Matthias Hasewend, BSc

Photoionization Spectroscopy on Single Cr Atoms in Superfluid Helium Nanodroplets

MASTER THESIS

For obtaining the academic degree
Diplom-Ingenieur

Master Programme of
Technical Physics

Graz University of Technology

Supervisor: Univ.-Prof. Mag. Dr.rer.nat Wolfgang E. Ernst

Co-Supervisor: Dipl.-Ing. Dr.techn. Markus Koch

Institute of Experimental Physics

Graz, August 2012

Danksagung

Univ.-Prof. Mag. Dr.rer.nat. Wolfgang E. Ernst hat diese Masterarbeit ermöglicht und betreut. Trotz seiner vielen Aufgaben als Institutsleiter und darüber hinaus nahm er sich die Zeit, auf Fragen und Wünsche einzugehen. Er gab manchen Denkanstoß zur Interpretation der Ergebnisse.

Markus Koch übernahm die Co-Betreuung. Seine Freude an der Physik wirkt ansteckend. Er war stets engagiert, experimentelle Erfahrung und theoretisches Wissen weiterzugeben. Während der Messungen stand er unterstützend zur Seite. Er hat diese Arbeit ausführlich korrekturgelesen.

Andreas Kautsch hat mit seiner Fähigkeit zur raschen Problemlösung sehr zum Gelingen dieser Masterarbeit beigetragen, sowohl im Experiment als auch in der Interpretation. Er hat im Labor Verbesserungsmöglichkeiten erkannt und umgesetzt und gab mir viele wertvolle Tipps.

Martin Ratschek ist mir besonders in der Einarbeitungsphase zur Seite gestanden. Gerne gab er sein Wissen über den Experimentellen Aufbau, die Interpretation und die Theorie weiter. Er hatte ebenfalls viele Tipps parat.

Johann Pototschnig ist sehr kompetent in theoretischer Physik. Gerade für die Auswertungen und den Theorieteil in dieser Masterarbeit lieferte er einige Denkanstöße.

Prof. Theo Neger und **Prof. Laurentius Windholz** sind nicht nur wegen ihrer langjährigen Erfahrung gute Ansprechpartner für Fragen physikalischer und technischer Natur.

Rupert Maierhofer, **Uwe Seidl**, **Werner Luttenberger**, **Josef Friedrich** und **Reinhard Dämon** betreuen die Werkstätten. Sie wissen, wie man schnell und zuverlässig fertigt.

Sandra Brunner, **Bettina Gsöls-Bedenik** und **Elisabeth Weiß** sind unentbehrlich, wenn es um organisatorische Dinge, Bestellungen, Abrechnungen, Termine und vieles mehr, oder einfach um Bürobedarf geht.

Günther Krois, **Florian Lackner** und **Moritz Theisen** vom Cluster Labor I waren sehr hilfsbereit, als es um das Kennenlernen des Farbstoff-Lasersystems ging. Während der Messungen stellten sie Vergleichsdaten bereit und erleichterten so das Herangehen.

Michaela Ellmaier, **Bettina Gamper**, **Christian Gösweiner**, **Patrik Kraus**, **Michaeal Mayrhofer**, **Johannes Poms**, **Toni Tamtögl**, **Phillip Thaler**, **Alexander Volk** und andere Personen machten die Arbeit am Institut sehr angenehm.

Gernot Gruber, **Christian Hartler**, **Iris Hehn**, **Raffael Hinteregger**, **Klaus Lang**, **Andreas Martitsch**, **Martin Nuss**, **Markus Polanz**, **Sebastian Rohm**, **Richard Romirer**, **Yao Shan**, **Gernot Sturm**, **Rebecca Sumann**, **Robert Winkler** und andere Studienkollegen waren immer für anregende Gespräche zu verschiedensten Themen zu haben. Oder wenn es darum ging, Spaß zu haben.

Ich danke den genannten Personen recht herzlich! Ebenso danke ich allen Freunden und Verwandten, die mich während meiner Studienzeit unterstützt haben. Ich danke allen Lehrerinnen und Lehrern, die mich zu Schulzeiten gefördert und mir Begeisterung vermittelt haben.

Franz und Maria Hasewend, meinen Eltern, gilt besonderer Dank. Sie haben meine Freude an den Naturwissenschaften geweckt. Während der Schulzeit haben sie mich mit nötigem Nachdruck zur Leistung animiert, mir aber dennoch Freiheit zur persönlichen Entwicklung gelassen. Während meiner Studienzeit konnte ich auf ihre volle Unterstützung bauen.

Der gleiche Dank gilt meinem Bruder **Thomas Hasewend**.

Kurzfassung

In dieser Masterarbeit geht es um die bislang ersten spektroskopischen Untersuchungen von Chromatomen auf superflüssigen Heliumnanotröpfchen. Das dafür eingesetzte Verfahren ist die massenselektive Photoionisierungsspektroskopie. Cr Atome sind besonders interessant, weil sie das höchste magnetische Moment aller Elemente besitzen. Es werden zuvor auch Rb-dotierte Tröpfchen untersucht, allerdings hatten diese Untersuchungen einzig den Zweck, geeignete Bedingungen für die Spektroskopie an Cr zu finden.

Wesentliche Komponente des Versuchsaufbaus ist ein Strahl aus Heliumtröpfchen. Er wird mit einer auf wenige Kelvin gekühlten Düse erzeugt und durchquert eine Vakuumapparatur. Die Tröpfchentemperatur beträgt etwa 0.4 K. Helium ist bei dieser Temperatur flüssig und besitzt eine superflüssige Phase. Die Tröpfchen nehmen Cr- oder Rb Atome auf. Sie stören die elektronische Struktur der Dopanden nicht allzu stark. Zudem sind sie bis in den UV Bereich transparent für Licht. Innerhalb der Apparatur wird an den dotierten Tröpfchen die Spektroskopie durchgeführt. Dazu wird der Tröpfchenstrahl mit einem durchstimmbaren gepulsten Laserstrahl gekreuzt. Der Laserstrahl stammt aus einem excimergepumpten Farbstofflaser und besitzt eine Pulsenergie im mJ-Bereich. Die Wellenlängen liegen im Bereich 330 bis 440 nm. Durch Absorption von Laserphotonen werden die Atome im Tröpfchen angeregt. Wegen der Wechselwirkung mit dem Helium sind tröpfcheninterne Zustände im Vergleich zu den freien Cr Zuständen energetisch verschoben und verbreitert.

Nach der Anregung kann es, wie in dieser Masterarbeit beschrieben, zur Ablösung der Cr Atome von den Tröpfchen kommen. Diese nunmehr freien und angeregten Atome werden durch Laserphotonen ionisiert. Es wird gezeigt, dass zwei verschiedene Photoionisierungsmechanismen auftreten. Der erste ist die direkte Ionisierung von angeregten Zuständen in das Ionisierungskontinuum. Im Kontrast dazu steht der Autoionisierungsmechanismus. Dabei gelang das Cr Atom zunächst in diskrete Anregungen oberhalb der Ionisierungsschwelle, die mit dem Ionisationskontinuum interferieren. Das nennt man Fano-Resonanz. Letztlich zerfallen diese Anregungen in Ionen und auslaufende Elektronen.

Die Ionen werden mit einem Quadrupolmassenspektrometer massenselektiert und mit einem Sekundärelektronenvervielfacher detektiert. Die Massenselektion schafft einen zusätzlichen Informationsgewinn.

Ziel dieser Masterarbeit ist die Erforschung des Verhaltens der Cr-Atome in der superfluiden Umgebung.

Abstract

This master thesis is about the very first spectroscopic investigations of chromium atoms in superfluid helium nanodroplets. The applied method is mass-selective photoionization spectroscopy. Cr atoms are of special interest because they have the highest magnetic moments of all the elements. Also Rb-doped droplets are investigated. Yet the purpose of these measurements is to find proper conditions for spectroscopy on Cr-doped droplets.

The main component of the setup is a helium droplet beam produced by a cooled nozzle in a vacuum chamber. The droplet temperature is about 0.4 K. At this temperature, helium is liquid and has a superfluid phase. The droplets pick up Cr or Rb atoms. Droplets are a relatively low-perturbing environment for the electronic structure of the dopants. Furthermore they are transparent for light up to the UV region. Within the apparatus, photoionization spectroscopy can be performed on the doped droplets. Therefore the droplet beam is crossed with a pulsed and tuneable laser beam. The laser beam origins from an excimer-pumped dye laser and has a pulse energy in the range of mJ. The wavelength ranges from 330 to 440 nm. By absorption of photons from the laser beam, atoms in the droplets are excited. Due to interaction with the surrounding helium, in-droplet states are shifted and broadened in energy compared to bare Cr states.

Subsequently, as shown in this master thesis, excited Cr atoms are ejected from the droplets. Excited bare atoms appear and are ionized by laser photons. Two different photoionization mechanisms are possible. The first mechanism is direct ionization from excited states into the ionization continuum. In contrast, ions are also produced by the autoionization mechanism. Cr atoms are excited into discrete levels above the first ionization threshold, which interfere with the ionization continuum. This is called Fano resonance. Such excitations finally decay into ions and evanescent electrons.

Ions are mass-selected by a quadrupole mass spectrometer and detected by a secondary electron multiplier. The mass-selection provides additional information.

The very aim of this master thesis is to explore the behaviour of Cr atoms within the superfluid surrounding.

Deutsche Fassung:
Beschluss der Curricula-Kommission für Bachelor-, Master- und Diplomstudien vom 10.11.2008
Genehmigung des Senates am 1.12.2008

EIDESSTATTLICHE ERKLÄRUNG

Ich erkläre an Eides statt, dass ich die vorliegende Arbeit selbstständig verfasst, andere als die angegebenen Quellen/Hilfsmittel nicht benutzt, und die den benutzten Quellen wörtlich und inhaltlich entnommene Stellen als solche kenntlich gemacht habe.

Graz, am ……. ……..
(Unterschrift)

Englische Fassung:

STATUTORY DECLARATION

I declare that I have authored this thesis independently, that I have not used other than the declared sources / resources, and that I have explicitly marked all material which has been quoted either literally or by content from the used sources.

……. ……..
date (signature)

Contents

1 Introduction **18**

2 Theoretical Background **20**
2.1 Superfluid He Nanodroplets 20
2.2 Cr and Rb 20
2.3 Multiple Electron Atoms 22
2.3.1 Hamiltonian 23
2.3.2 Multiple Electron States 24
2.3.3 Exchange Energy 25
2.3.4 Aufbau Principle 27
2.3.5 LS- and jj-Coupling 27
2.4 Multiple Electron Term Notations 28
2.5 Multiple Electron Dipole Transition Rules 29
2.6 PI Spectroscopy and PI Mechanisms 32
2.6.1 Direct PI - Born Approximation 33
2.6.2 Autoionization - Fano Resonances 34
2.7 Interaction between Dopant and He 36

3 Experimental Setup **38**
3.1 He Droplet Beam Apparatus 40
3.1.1 Source Chamber 41
3.1.2 Pickup Chamber 42
3.1.3 Optimizing Single Cr Pickup 45
3.1.4 Main Chamber 47
3.1.5 QMS Chamber 47
3.1.6 Optimizing Ion Yield 49
3.2 SR400 51
3.3 Transmission Window 51
3.4 Laser System 53
3.4.1 Dye Laser 53
3.4.2 Laser Dyes 54
3.4.3 Pump Laser 55
3.4.4 Attenuators 56
3.4.5 Minimizing ASE 56
3.5 ADC Card 61
3.6 Monochromator 62

3.7 Picoamperemeter and Analog Processor . . . 64
3.8 Wavemeter . . . 65
3.9 Laser Beam Profilometer . . . 66
3.9.1 A Method of recording Intensity Profiles . . . 67
3.9.2 Test Profiles . . . 68

4 Experimental Results 71
4.1 Bare Rb Atom PI Spectra using Stilbene 3 Laser Dye . . . 71
4.1.1 First PI Measurements . . . 72
4.1.2 Optimized Bare Rb Atom Spectrum . . . 74
4.1.3 Fitting the Spectra . . . 76
4.1.4 Conclusion . . . 79
4.2 Rb-doped Droplet Spectra using Stilbene 3 Laser Dye . . . 79
4.2.1 First Measurements . . . 79
4.2.2 Laser Energy Normalization . . . 81
4.2.3 Mass Spectrum . . . 83
4.2.4 Conclusion . . . 85
4.3 Cr-doped Droplet Spectra using DMQ Laser Dye . . . 86
4.3.1 First Attempts . . . 87
4.3.2 Laser Energy Normalization . . . 90
4.3.3 Bare Cr - Excitation and Ejection . . . 91
4.3.4 Autoionization . . . 92
4.3.5 Continuous Structure . . . 94
4.3.6 Population of Atomic States . . . 96
4.3.7 Mass Scans . . . 97
4.3.8 Conclusion . . . 100
4.4 Cr-doped Droplet Spectra using PTP Laser Dye . . . 100
4.5 Latest Results . . . 103

5 Conclusion and Outlook 106

6 Bibliography 108
6.1 Papers . . . 108
6.2 Theses . . . 109
6.3 Books . . . 111
6.4 Manuals . . . 111
6.5 Online-Sources . . . 112

7 Appendix 113

List of Figures

2.1 Ground State Electronic Configuration of Cr . . . 21
2.2 Temperature Dependence of the Vapour Pressure of Cr and Rb . . . 22
2.3 Direct PI Cross Section versus Photon Energy . . . 34
2.4 Fano Line Profile of Autoionizing States . . . 35

3.1 Experimental Setup . . . 39
3.2 He droplet Beam Apparatus Front View . . . 40
3.3 Droplet Size and Droplet Velocity . . . 41
3.4 Droplet Size . . . 42
3.5 Electron Bombardment Cr Source . . . 43
3.6 Pfeiffer QMG 220 QMS . . . 44
3.7 Cr Monomer Pickup Yield . . . 46
3.8 QMS Chamber Setup . . . 48
3.9 Sketch of the Ion Extraction Region . . . 49
3.10 QMS Voltage Optimization . . . 50
3.11 SR400 Front View . . . 51
3.12 QMS Chamber and Flange Window . . . 52
3.13 Fused Silica Transmission Curve . . . 52
3.14 Dye laser, Circulator and Cuvette . . . 53
3.15 Pump Laser . . . 55
3.16 Covered and uncovered Oscillator Grating Laser Spectral Profiles . . . 57
3.17 Dye Laser Spectral Profile for Stilbene 3 . . . 58
3.18 Spectral Distribution of DMQ Pulse Energy . . . 59
3.19 Dye Laser Spectral Profile for DMQ . . . 60
3.20 Self-developed Aperture . . . 61
3.21 Meilhaus ADC Card Connector Board . . . 61
3.22 Monochromator, wrapped PM, Control Unit and Power Supply . . . 63
3.23 Picoamperemeter and SR235 Analog Processor . . . 64
3.24 PM Signal before and after Picoamperemeter . . . 64
3.25 Pulse Wavemeter and Entrance Hat . . . 65
3.26 Beam Profilometer Equipment . . . 67
3.27 Real Color Images of attenuated Laser Beams recorded with the CCD . . . 68
3.28 Surface Plot of a Beam Profile showing massive Saturation . . . 69
3.29 Surface Plots of a noisy Profile and the same Profile after Smoothing . . . 69
3.30 Pseudocolor Plots of a noisy Profile and same Profile after Smoothing . . . 70

4.1 Bare Rb Atom Energy Level and Transition Scheme . . . 72

4.2 Bare Rb Atom PI Spectrum before Laser Optimization 73
4.3 Bare Rb Atom PI Spectrum after Laser Pulse Energy Optimization . . . 74
4.4 Bare Rb Atom PI Spectrum after Low ASE Optimization 75
4.5 Raw and FFT smoothed Laser Profile 75
4.6 Gauss Fit and Residuals of Bare Rb PI Spectrum 76
4.7 Gauss and Lorentz Fits of Residual Rb PI Spectrum 77
4.8 First Rb doped Droplet PI Spectrum 80
4.9 First Rb doped Droplet PI Spectrum - Dimers 81
4.10 First Rb doped Droplet PI Spectrum - Laser Energy Normalisation . . . 82
4.11 First Rb doped Droplet Mass Spectrum 84
4.12 First Rb doped Droplet Mass Spectrum - Dimers 85
4.13 Bare Cr Atom Energy Level and Transition Scheme 87
4.14 First Cr doped Droplet PI Spectrum and Laser Pulse Energy 88
4.15 Cr-doped Droplet PI Spectrum - Detailed View of the Peaks 89
4.16 Raw and FFT smoothed Laser Profile 89
4.17 First Laser Energy normalized Cr doped Droplet PI Spectrum 90
4.18 Cr - Excitation and Ionization Scheme 91
4.19 Prominent Excitation and Autoionization Scheme of Cr 93
4.20 Cr - Excitation and Ionization Scheme 95
4.21 First Laser Energy normalized Cr doped Droplet PI Spectrum 96
4.22 Cr - Transition Scheme 97
4.23 First Cr and Rb doped Droplet Mass Spectrum 98
4.24 First Cr doped Droplet Mass Spectrum at Peak Wavelength 99
4.25 Cr doped Droplet PI Spectrum and Laser Pulse Energy 101
4.26 Smoothed Cr doped Droplet PI Spectrum 102
4.27 Smoothed and Laser Energy normalized Cr doped Droplet PI Spectrum . 103
4.28 Cr doped Droplet PI Spectrum and Laser Pulse Energy 104
4.29 Cr doped Droplet PI Spectrum 104
4.30 Raw and FFT smoothed Laser Profile 105

7.1 Meilhaus ADC Card Connector Board 113
7.2 Front Panel of singleDIO.vi 114
7.3 Block Diagram of singleDIO.vi 115
7.4 Front Panel of singleAI.vi 117
7.5 Block Diagram of singleAI.vi 118
7.6 Front Panel of singleAO.vi 118
7.7 Block Diagram of singleAO.vi 119
7.8 Front Panel of singleCTR.vi 120
7.9 Block Diagram of singleCTR.vi 120

List of Tables

3.1 Ion Extraction Region Voltages 50
3.2 Comparing Data of different Laser Dyes 54

4.1 Fit Parameters 77
4.2 Number of allowed m_J Transitions between J Sublevels 93

Abbreviations

ASE ..... Amplified Spontaneous Emission
ADC ..... Analog-Digital Converter
CCD ..... Charge-Coupled Device
CLI ..... Cluster Laboratory I at the Institute of Experimental Physics
CLII ..... Cluster Laboratory II at the Institute of Experimental Physics
Cr ..... Chromium
ESR ..... Electron Spin Resonance
FFT ..... Fast Fourier Transform
FWHM ..... Full Width at Half Maximum
GPIB ..... General Purpose Interface Bus, also called IEEE-488
LED ..... Light Emitting Diode (state indicator in LabView)
LIF ..... Laser-induced Fluorescence
PI ..... Photoionization
PM ..... Photomultiplier
Rb ..... Rubidium
SEM ..... Secondary Electron Multiplier
SEQ ..... Schroedinger Equation
TOF ..... Time-of-flight Mass Spectrometer
TTL ..... Transistor-transistor Logic
UV ..... Ultraviolet Light
QMS ..... Quadrupole Mass Spectrometer

1 Introduction

Superfluid helium nanodroplets provide an outstanding method of preparing single- or multiple-atomic systems. Within the droplets, dopants can interact and aggregate. Different sorts of dopants can be mixed. The mean dopant number per droplet can be controlled. Thus it can be selected, which species are favoured in aggregation. Tailored clusters and molecules can be produced. The nanodroplets are a quantum lab to study the physical basics of chemistry.

Spectroscopic methods are the key to the properties of atoms, molecules and clusters. This master thesis is focussing on one certain method, namely photoionization laser spectroscopy. The measured signal is a wavelength-depending ion yield. In combination with a mass spectrometer, this method provides a high content of information due to the mass selection of the ions.

The CLII droplet apparatus was built from a molecular beam apparatus by Markus Koch in course of his doctoral thesis to perform electron spin resonance experiments. Martin Ratschek designed a high-temperature Cr-source. This source made it possible to dope the droplets with Cr. The aim was ESR on Cr-doped droplets, which is interesting due to the high magnetic moment of Cr atoms.

Yet electron spin resonance was preceded by laser-induced fluorescence and photoionization experiments. Laser-induced fluorescence was performed by Andreas Kautsch and Martin Ratschek, photoionization by Matthias Hasewend and Andreas Kautsch in course of their master and doctoral thesis, respectively.

Before that, photoionization experiments had never been performed on the CLII apparatus. In the CLI, photoionization was already performed on Rb-doped droplets and other species. Thus it was helpful to optimize the procedure of photoionization on Rb-doped droplets in order to reproduce the results of CLI. Therewith a good basic concept for photoionization on Cr-doped droplets was found.

For photoionization spectroscopy, at least a two-step excitation- and ionization process is advantageous. The most simple and thus favoured photoionization scheme is two-photon-one-colour. In the beginning, it was not obvious which laser system to use. In principal, two-step processes require an increased photon density. Thus the excimer-pumped pulsed dye laser of CLI was considered to be suitable. During a pulse, its photon density is relatively high. Furthermore it is easy to tune. Disadvantages of this laser system are the time-consuming adjusting and the dye exhaustion.

By means of the two-photon-one-colour photoionization scheme, atomic states above half the ionization energy can be investigated. Using energy levels from literature [43], [9] and [12], it was easy to figure out an interesting laser energy range. Therefore different laser dyes had to be chosen. The dyes are listed in subsection 3.4.2.

Further preparation concerned reconstructions of the apparatus and assembling an optical path to guide the laser from CLI to CLII. Furthermore, LabView and MATLAB programs had to be designed in order to control the components and to process measurement data.

Chapter 2 provides the basics of multiple electron atoms, as they had been investigated in course of this thesis. Furthermore it presents optical excitation and photoionization mechanisms of such systems. Also the role the surrounding helium is playing for the dopants is shown.

Chapter 3 is describing the apparatus, instruments and utilities necessary for performing the measurements. It shows the properties of the components and how to configure them in order to achieve good results.

Chapter 4 is the most extensive chapter. It outlines the experimental procedure and results. This chapter describes the measurements on single Rb atoms as well as on Rb- and Cr-doped droplets. Each section is based on the scheme expectation $\rightarrow$ approach $\rightarrow$ results $\rightarrow$ conclusion. The last section shows the latest photoionization results that are also published in [5].

2 Theoretical Background

PI spectroscopy on Cr and also Rb atoms in superfluid He nanodroplets is the very topic of this master thesis. This chapter outlines the theoretical background in order to understand why Cr is of special interest. It also presents the properties of the nanodroplets. The most important topics are dealing with multiple electron atoms in order to interpret the experimental results of chapter 4. Therefore it is also important to understand PI spectroscopy and how ionization works. Finally a model describing the interaction between the metal atoms and the He is presented.

2.1 Superfluid He Nanodroplets

Doping superfluid He nanodroplets with atoms is an outstanding method of preparation. Advantages are described in [3]. This chapter of the book also includes the significance of the droplets as a cold bath, different sorts of spectra and their applications and the limits of in-droplet spectroscopy. Further information is found in master theses of Alexander Volk [30], Martin Ratschek [28], Florian Lackner [22] and the doctoral thesis of Markus Koch [20]. These sources include production and properties of the droplets, their size and velocity, the doping and spectroscopy on droplets.

Droplet production is outlined in subsection 3.1.1. The four-chamber vacuum system for production, doping and investigation of the droplets including relevant parameters is shown. [15] is another source of information.

2.2 Cr and Rb

Rb is an alkaline metal. It has one single electron outside a closed Kr shell. Electronic properties are similar to hydrogen. Details concerning Rb are not discussed here. Master thesis [30] and doctoral thesis [20] give information about the abundance, the physical and chemical properties, the isotopic composition, the vapour pressure and transitions of Rb. Subsection 3.1.2 describes the vaporization of Rb including specific parameters.

Here it is more interesting to show what makes Cr relevant for investigation. Bulk properties are well known. Due to a stable oxide layer, Cr is used for passivations, as known from car tuning, and also for alloys and catalytic converters. The natural isotopic composition is 4.3 % ^{50}Cr, 83.8 % ^{52}Cr, 9.5 % ^{53}Cr and 2.4 % ^{54}Cr.

Concerning this work, it is rather the atomic properties that make Cr special. Bulk Cr is antiferromagnetic, but small clusters are superparamagnetic, as shown in [2]. Single Cr atoms have a high spin and thus the highest magnetic moment of all elements. The ground state electronic configuration is shown in fig. 2.1. It consists of an Argon shell and six outer electrons of parallel spin due to the Pauli Principle mentioned in subsection 2.3.2. These valence electrons align their spins. The reason for the spin alignment is discussed in subsection 2.3.3. 4p and 5s orbitals are populated during excitation and PI experiments, as shown in fig. 4.20 in subsection 4.3.5.

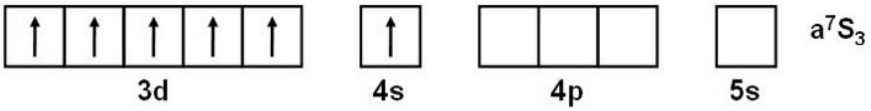

Figure 2.1: Ground State Electronic Configuration of Cr

The high magnetic moment provided by these six electrons makes Cr an interesting element. In conventional microelectronics, the charge of the electrons is coding the information. A new branch called Spintronics is focussing on methods to use the electron spin instead. Spintronics is based on physical effects dealing with spin magnetic moments. For example the electric resistance of ferromagnetic thin layers can be highly dependent on the direction of magnetization. That effect is called giant magneto resistance (GMR). It is imagineable that Cr clusters can contribute to this new branch of materials development.
Spectroscopy is the key method to investigate electronic structure, especially for the high-spin elements. From the electronic structure, future applications in magneto-electronic devices could be derived.

This master thesis includes a description of the vaporization of Cr and specific parameters, found in subsection 3.1.2. An excitation scheme is found in fig. 4.1 in section 4.1. Cr levels are listed in [13]. Further information about Cr is found in [11]. Master thesis [26] is accounting to physical properties and transitions of Cr.

The process of doping nanodroplets with Cr, Rb or other dopants is called pickup. Concerning pickup, the difference between Rb and Cr is that Rb is much more volatile, as fig. 2.2 shows.

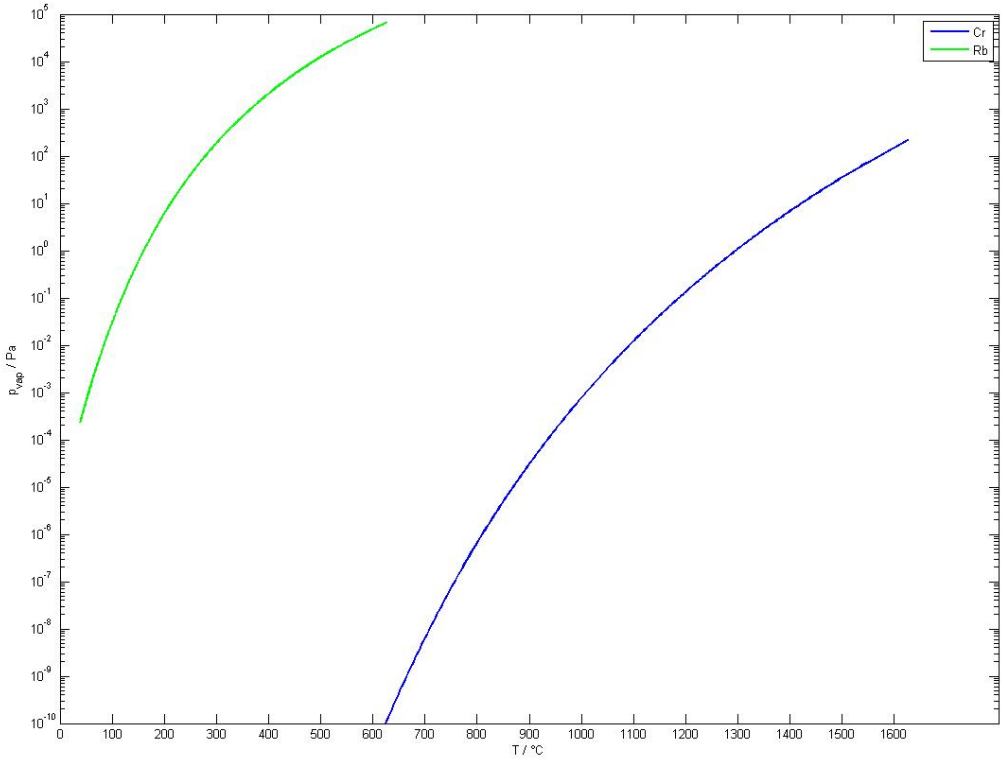

Figure 2.2: Temperature Dependence of the Vapour Pressure of Cr and Rb

Note that the melting temperatures of Rb and Cr are 39 and 1907 °C. The temperature-dependent vapour pressures of Rb and Cr had been computed using empirical formulas outlined in [37]. During experiments in course of this master thesis, Rb heating temperatures ranged from 70 to 100 °C. Obviously this corresponds to vapour pressures of 0.01 to 0.1 Pa. A Cr heating power of 200 W is corresponding to local temperatures of 1650 °C, as shown in [28]. Thus the maximum vapour pressure of Cr reached in our setup is about 100 Pa. See subsection 3.1.2 for further information.

2.3 Multiple Electron Atoms

Atoms consist of an electron shell and a core. The core can be fixed and considered as the source of an ideal coulomb potential for the electrons (Born-Oppenheimer approximation). Thus one can treat the atom as a multiple-electron quantum mechanical system. A Schroedinger equation can be formulated. In the Bohr semi-classical atomic model, electrons are charged particles moving around the core. Thus they have a quantized magnetic moment. Electrons also have a spin and thus another magnetic moment. Both magnetic moments interact. This is called spin-orbit-interaction.

2.3.1 Hamiltonian

For the SEQ, the whole Hamiltonian reads as

$$\mathrm{H} = \sum_{i=1}^{N} \left[\frac{1}{2m} \left(\mathbf{p}_i - e\mathbf{A}_i \right)^2 - e\mathrm{V}_i - \frac{2\,\mathrm{g_S}\,\mu_\mathrm{B}}{\hbar}\,\mathbf{S}_i \cdot \mathbf{B}_i \right]. \tag{2.1}$$

It is the sum of N single electron Hamiltonians in an external electromagnetic field. This field is produced by the charge of the core and the other electrons and the spin- and orbital magnetic momenta of the other electrons. Beside common momentum- and position-operators, the Hamiltonian includes a magnetic vector potential operator $\mathbf{A}_i$, a spin operator $\mathbf{S}_i$ and a magnetic field operator $\mathbf{B}_i$. $\mu_\mathrm{B} = \frac{e\hbar}{2m}$ is Bohrs magneton. The vector potential $\mathbf{A}_i$ is

$$\mathbf{A}_i = \frac{\mu_0\,\mu_\mathrm{B}}{4\pi\hbar} \sum_{j=1,\,j\neq i}^{N} \left[\frac{1}{\left|\mathbf{r}_i - \mathbf{r}_j\right|^3} \left[\left(\mathbf{r}_i - \mathbf{r}_j\right) \times \left(\mathrm{g_S}\mathbf{S}_j + \mathrm{g_L}\mathbf{L}_j\right) \right] \right]. \tag{2.2}$$

It includes all the magnetic vector potentials generated by the spin- and orbital magnetic momenta of the other electrons. It is formulated in Lorenz gauge. The way it is included in the Hamiltonian (2.1), the Lorentz force on the electron i caused by these magnetic momenta is taken into account. $(\mathbf{r}_i - \mathbf{r}_j)$ is the difference vector between the positions of electrons i and j. $\mathbf{L}_j$ is the angular momentum of electron j. $\mathrm{g_S}$ and $\mathrm{g_L}$ are the Landé factors for the spin- and orbital magnetic moments caused by angular momentum. $\mathrm{g_S}$ is approximately 2, while $\mathrm{g_L}$ is exactly 1.

The scalar potential produced by the electron charges and the core is

$$\mathrm{V}_i = \frac{1}{4\pi\epsilon_0} \left[\frac{Ze^2}{\left|\mathbf{r}_i\right|} - \sum_{j=1,\,j\neq i}^{N} \frac{e^2}{\left|\mathbf{r}_i - \mathbf{r}_j\right|} \right]. \tag{2.3}$$

External electric fields, like laser fields for exciting the atom, can be regarded by introducing additional scalar potentials, as shown below in section 2.5.

Interaction between the angular magnetic moment of electron i and the magnetic field created by the other electrons was already considered by introducing the vector potential. The spin magnetic moment of electron i couples to a **B**-field which reads as

$$\mathbf{B}_i = \nabla \times \mathbf{A}_i - \frac{1}{mc^2} \left[\mathbf{p}_i \times \nabla \mathrm{V}_i \right]. \tag{2.4}$$

By including the derivative of the vector potential in the **B**-field, interaction between the spin magnetic moment of electron i and the magnetic field is also taken into account. The second term of $\mathbf{B}_i$ comes from the spin-orbit interaction. The orbital angular momentum of an electron is caused by the Coulomb potential of all the other electrons and the core. The total electric field can accelerate the electron perpendicular to its velocity. This gives the electron an additional angular momentum and thus a magnetic moment,

which can interact with the spin magnetic moment. This is called spin-orbit interaction.

The Hamiltonian (2.1) includes Coulomb interaction between electrons and core, electron-electron Coulomb interaction and interaction between the electrons orbital and spin magnetic moments. In principal, solutions of the SEQ give a good approximation of the electronic structure of the atom.[1]

Interactions presented in this subsection enable multiple electron transitions of Cr and other atoms.

Unfortunately, the problem is formulated in 3N spatial dimensions times a factor 2N respecting the spin of the N electrons. The high dimensionality and the complicated electron-electron-interaction make it impossible to find exact solutions even for only a two electron problem like the He atom.

2.3.2 Multiple Electron States

At least an ansatz for the multiple electron wavefunction can be found. A basis set can be constructed as products of wavefunctions out of a single electron basis set, as shown in formula (2.5) for a two-electron system. Modified hydrogen wavefunctions can for example form the single electron basis set. This basis set automatically respects the spherical symmetry and the Coulomb-interaction with the core. $\mathbf{r}$ is the vector of the three spatial coordinates of the electron, s is the spin coordinate. Ψ is a total electron wavefunction consisting of a spin- and an orbital part.

$$\Psi_{\text{tot}}(\mathbf{r}_1, \mathrm{s}_1, \mathbf{r}_2, \mathrm{s}_2) = \Psi_1(\mathbf{r}_1, \mathrm{s}_1)\, \Psi_2(\mathbf{r}_2, \mathrm{s}_2) \tag{2.5}$$

This notation means that one electron is in the state described by Ψ_1, while the state of the other electron is described by Ψ_2.

Electrons are indistinguishable. Thus the electron density must not change if two electrons change their state. Furthermore, theory demands that multi-particle fermionic wavefunctions are antisymmetric under particle exchange. Formula (2.6) shows what this is supposed to mean in the case of a two-electron system.

$$\Psi_{\text{tot}}(\mathbf{r}_1, \mathrm{s}_1, \mathbf{r}_2, \mathrm{s}_2) \stackrel{!}{=} -\Psi(\mathbf{r}_2, \mathrm{s}_2, \mathbf{r}_1, \mathrm{s}_1) \tag{2.6}$$

This restriction can only be fulfilled, if the wavefunction is a sum of several product states represented by a so-called Slater-determinant. For a two-electron system, the Slater determinant reads as

[1] Beside these interactions included in the Hamiltonian (2.1), other effects can have an impact on the spectrum. The spin magnetic moment of the core can interact with the spin- and orbit-magnetic moment of the electrons causing some extra level splitting. The core magnetic moment is low compared to the electron moments. Thus the splitting is relatively small. It is called hyperfine structure. Furthermore, the Hamiltonian (2.1) does not include relativistic effects and electromagnetic field quantisation. Although there exist ways to regard them, as shown in Diracs theory and Quantum Electrodynamics (QED).

$$\Psi_{\text{tot}}(\mathbf{r}_1, \mathrm{s}_1, \mathbf{r}_2, \mathrm{s}_2) = \frac{1}{\sqrt{2}} \left[\Psi_1(\mathbf{r}_1, \mathrm{s}_1)\, \Psi_2(\mathbf{r}_2, \mathrm{s}_2) - \Psi_1(\mathbf{r}_2, \mathrm{s}_2)\, \Psi_2(\mathbf{r}_1, \mathrm{s}_1)\right] = \tag{2.7}$$

$$\frac{1}{\sqrt{2}} \begin{vmatrix} \Psi_1(\mathbf{r}_1, \mathrm{s}_1) & \Psi_2(\mathbf{r}_1, \mathrm{s}_1) \\ \Psi_1(\mathbf{r}_2, \mathrm{s}_2) & \Psi_2(\mathbf{r}_2, \mathrm{s}_2) \end{vmatrix}.$$

It can easily be generalized for arbitrary numbers of electrons, as shown in formula (2.8).

$$\Psi_{\text{tot}}(\mathbf{r}_1, \mathrm{s}_1, \mathbf{r}_2, \mathrm{s}_2, \ldots, \mathbf{r}_N, \mathrm{s}_N) = \frac{1}{\sqrt{N!}} \begin{vmatrix} \Psi_1(\mathbf{r}_1, \mathrm{s}_1) & \Psi_2(\mathbf{r}_1, \mathrm{s}_1) & \cdots & \Psi_N(\mathbf{r}_1, \mathrm{s}_1) \\ \Psi_1(\mathbf{r}_2, \mathrm{s}_2) & \Psi_2(\mathbf{r}_2, \mathrm{s}_2) & \cdots & \Psi_N(\mathbf{r}_2, \mathrm{s}_2) \\ \vdots & \vdots & \ddots & \vdots \\ \Psi_1(\mathbf{r}_N, \mathrm{s}_N) & \Psi_2(\mathbf{r}_N, \mathrm{s}_N) & \cdots & \Psi_N(\mathbf{r}_N, \mathrm{s}_N) \end{vmatrix} \tag{2.8}$$

Evaluating this determinant gives a sum of products of N single electron wavefunctions. The order, which electron occupies which state, is permuted. The whole expression changes its sign, if two electrons are exchanged.[2]

Using a suitable single electron basis set, eigenstates of the Hamiltonian (2.1) can be represented by a single slater determinant.[3]

Such states can describe the electronic structure of atoms and molecules.

2.3.3 Exchange Energy

Correspondences of the following derivation can be found in various books about many-body quantum mechanics, for example [36].

Claiming for multiple electron wavefunctions to be represented by Slater determinants brings some consequences for the electronic properties. In the following, consequences are demonstrated by means of a two-electron system. Results can be generalized to arbitrary numbers of electrons. A two-electron spatial wavefunction reads as

$$|\psi(\mathbf{r}_1, \mathbf{r}_2)\rangle = \frac{1}{\sqrt{2}} \left[\psi_1(\mathbf{r}_1)\, \psi_2(\mathbf{r}_2) \pm \psi_1(\mathbf{r}_2)\, \psi_2(\mathbf{r}_1)\right] =: |12\rangle \pm |21\rangle. \tag{2.9}$$

Dirac notation was introduced to make the following easier to read. (2.9) is only referring to the orbital parts of the electron wavefunctions. This is indicated by using $\psi(\mathbf{r})$ instead of $\Psi(\mathbf{r}, \mathrm{s})$. The `-´ in formula (2.7) was replaced with a `±´ because the

[2] If a certain single electron state is included two or more times in this matrix, the determinant becomes 0. Thus it is forbidden for electrons to pairwise have the same orbital and spin. That is the explanation of the Pauli Principle.

[3] Other basis sets could make the eigenstates become a sum of Slater determinants. In this case it is not be possible to decompose it into single electron states. The electrons are then entangled in terms of this basis set.

orbital product wavefunction may be both symmetric or antisymmetric under particle exchange, as long as the spin product wavefunction is assuring the total product wavefunction to be antisymmetric.

The two-electron Coulomb operator is

$$V_{\mathrm{c}} = \frac{1}{4\pi\epsilon_0} \frac{e^2}{|\mathbf{r}_1 - \mathbf{r}_2|}. \tag{2.10}$$

Note that it has a similar form as in (2.3). With this operator, the expectation value of the Coulomb interaction becomes

$$\langle\psi|V_{\mathrm{c}}|\psi\rangle = (\langle 12| \pm \langle 21|)\ V_{\mathrm{c}}\ (|12\rangle \pm |21\rangle) =$$

$$\langle 12|V_{\mathrm{c}}|12\rangle \pm \langle 12|V_{\mathrm{c}}|21\rangle \pm \langle 21|V_{\mathrm{c}}|12\rangle \pm \langle 21|V_{\mathrm{c}}|21\rangle =$$

$$2\left[\int\int \frac{|\psi_1(\mathbf{r}_1)|^2\ |\psi_2(\mathbf{r}_2)|^2}{|\mathbf{r}_1 - \mathbf{r}_2|} \pm \frac{\psi_1^*(\mathbf{r}_1)\,\psi_2^*(\mathbf{r}_2)\,\psi_1(\mathbf{r}_2)\,\psi_2(\mathbf{r}_1)}{|\mathbf{r}_1 - \mathbf{r}_2|}\,\mathrm{d}\mathbf{r}_1 \cdot \mathrm{d}\mathbf{r}_2\right]$$

$$=: C \pm S. \tag{2.11}$$

That result includes classical coulomb energy and an extra term called exchange energy. Exchange energy is a completely non-classical effect. It is caused by claiming indistinguishable electrons and antisymmetric multi-fermionic wavefunctions, as outlined above in subsection 2.3.2.

The result of (2.11) shows that the total energy is minimal, if the `$\pm$´ becomes a `-´. In this case, the total orbital wavefunction (2.9) is antisymmetric. Antisymmetric total orbital wavefunctions are thus energetically favoured.

Per construction of the multiple electron wavefunction as a Slater determinant, as outlined in formula (2.8), orbital asymmetry requires spin symmetry. This means alignment of the non-paired electron spins in the multiple electron ground state. Coulomb repulsion within the electron shell forces the electrons to align their spins. Exchange interaction can thus give an explanation for Hund´s rule described in [32].

The ground state spin alignment shown in fig. 2.1 is the reason for the large magnetic moment of single Cr.

Exchange energy is also a key to understand other phenomena, like ferromagnetism or certain chemical effects. Further information is found in [36].

2.3.4 Aufbau Principle

Exchange interaction explains Hund´s rule. On the other hand Hund´s rule describes the order of how to populate degenerated atomic states with electrons. The electron shell of the atom is filled in energetically ascending order. Combining these two rules gives the so-called Aufbau principle, as outlined in [32]. The Aufbau principle can explain the order of the periodic table of elements.

2.3.5 LS- and jj-Coupling

In subsection 2.3.1, it was said that the electrons of an atom can couple their spin and angular magnetic moment via magnetic interaction. The result is a total magnetic moments corresponding to a total angular momentum quantum number J. That can act in two different ways. Each electron has orbital- and spin-magnetic moment corresponding to angular momenta. The orbital angular momenta can form a total orbital angular momentum (2.12)), while the spin angular momenta form a total spin angular momentum (2.13).

$$\mathbf{L}_{\text{tot}} = \sum_{i=1}^{N} \mathbf{L}_i \tag{2.12}$$

$$\mathbf{S}_{\text{tot}} = \sum_{i=1}^{N} \mathbf{S}_i \tag{2.13}$$

These two angular momenta finally interact to form a total angular momentum (2.14).

$$\mathbf{J}_{\text{tot}} = \mathbf{L}_{\text{tot}} + \mathbf{S}_{\text{tot}} \tag{2.14}$$

This coupling scheme is called LS- or Russel-Sounders-Coupling. It can describe the behaviour of low atomic number electron shells in low external magnetic fields very well. $\mathbf{J}_{\text{tot}}$, $\mathbf{L}_{\text{tot}}$ and $\mathbf{S}_{\text{tot}}$ have quantum numbers J, L and S related by J = L + S.

For high atomic numbers, another model is more accurate, e.g. the jj-coupling scheme. Therein, the orbital- and spin-angular momenta of each electron couple to form total electron angular momenta (2.15).

$$\mathbf{J}_i = \mathbf{L}_i + \mathbf{S}_i \tag{2.15}$$

They have quantum numbers j_i. Subsequently, these electronic momenta couple to form the total angular momentum (2.16).

$$\mathbf{J}_{\text{tot}} = \sum_{i=1}^{N} \mathbf{J}_i \tag{2.16}$$

It has also a quantum number J.

Actual behaviours of atomic shells are mostly mixtures of LS- and jj-scheme. Cr is located somewhere between the regions better described by LS- and jj-coupling.

However, it is supposed that the LS-scheme is a sufficiently good approximation for this element.

As shown below in section 2.4, different J-values enumerate the sublevels of one single LS or jj configuration. The z^5P atomic level of Cr was populated during PI spectroscopy, as described in subsection 4.3.3. This level has sublevels of J = 3, 2 and 1. Corresponding energies are listed in [13]. J-sublevels are non-degenerated.

Due to precession of the total angular momentum, the J-sublevels of a configuration have 2J+1 sub-sublevels enumerated by a magnetic quantum number m_J ranging from J to +J. Without any magnetic field, these sub-sublevels are degenerated. Thus there can be two or more initial and final states at same level energy. One has to consider this degeneracy while estimating transition rates.

m_J-degeneracy has an impact on transition peak heights, as shown in (Tab. 4.2) in subsection 4.3.4.

This degeneracy can be broken by a magnetic field due to the Zeeman-effect. With increasing field, level energy differences are stretched. At strong magnetic fields, the sublevel structure changes due to a breakdown of the LS- and jj-coupling scheme. This is called Paschen-Back-Effect. Further information about Zeeman- and Paschen-Back-Effect is found in [31].

For experiments concerning this master thesis, no magnetic field was applied.

2.4 Multiple Electron Term Notations

Spectroscopy and computational quantum mechanics deliver information about atomic levels. Even simple atoms have a huge diversity of levels due to the different types of interaction considered in the Hamiltonian formula (2.1). Furthermore, spectra are complicated by the possibility of multiple electron excitations enabled by these interactions. Such processes can change the state of more than one electron.

To overlook this diversity, a term notation needs to be introduced. For hydrogen, it is common to give the quantum numbers of the state the single electron occupies. Using this convention, the ground state electron configuration of hydrogen is

$$\mathrm{GS_H} = 1\mathrm{s}^2. \tag{2.17}$$

This notation is described in [31]. The order of filling the single electron orbitals is regarding to the Aufbau principle described in subsection 2.3.3. The ground state electron configuration of Cr reads as

$$GS_{Cr} = 1s^2\,2s^2\,2p^6\,3s^2\,3p^6\,3d^5\,(^6S)\,4s^1 = [Ar]\,3d^5\,(^6S)\,4s^1, \tag{2.18}$$

with [Ar] representing the ground state electronic configuration of the next lower atomic number closed-shell noble gas Argon. (^{6}S) is indicating the L and S quantum number of the 3d electrons.

Yet this notation is too complicated. It should be replaced by a simpler one. For characterization of spectroscopic levels of atoms described by LS-coupling, it is enough to give the total L, S and J quantum numbers of the electron shell. These numbers were described in subsection 2.3.5. Different J-values enumerate the sublevels of a single L and S configuration. From the spin quantum number S, the total multiplicity of the shell is calculated by r = 2S + 1. Thus the ground state of Cr can be written as

$$|GS_{Cr}\rangle = {}^7S_3. \tag{2.19}$$

Ground state Cr is an example to explain this notation. For this state, J, L and S are 3, 1 and 3. The multiplicity r = 2S + 1 = 7 is marked in this notation by the supersript 7. The letter S is representing L = 0. The convention known from hydrogen states that S,P,D,F,... indicate L to be 0,1,2,3,... holds. The subscript 3 is representing J.

Unfortunately, this notation is not unique. There are always several states having the same S, L and J. The clue is to enumerate terms using additional letters. For even parity states, the enumeration starts at `a´ and continues alphabetically. For odd parity, it starts at `z´ and continues counter-alphabetically. The Cr ground state turns into

$$|GS_{Cr}\rangle = a^7S_3. \tag{2.20}$$

From this shortened notation, it is always possible to conclude the complete electronic configuration of a state. The multiple electron atomic transition rules described in the next section 2.5 refer to this notation. LS-coupling is also a good approximation for lots of other elements. Therefore, level diagrams of most of the elements use the described notation.

In this thesis, states of Cr are named regarding to this notation.

2.5 Multiple Electron Dipole Transition Rules

A pretty simple rule to calculate transition rates between two quantum states can be derived from elementary quantum mechanics by using a transition operator. Derivation was done by E. Fermi. Thus it is called Fermi´s Golden Rule. It reads as

$$\Gamma_{i\to f} = \frac{2\pi}{\hbar}\,|\langle\Psi_f|H|\Psi_i\rangle|^2\,\rho, \tag{2.21}$$

wherein $\Gamma_{i\to f}$ is the transition rate from initial to final state, $\hbar$ is Plancks constant, $\langle\Psi_f|$ the final state, H the transition Hamiltonian, $|\Psi_i\rangle$ the initial state and ρ the density

of final states at respective energy.

Initial and final states are multiple electron wavefunctions of the electron shell of the atom represented by Slater determinants described in subsection 2.3.2. The question is now which transition Hamiltonian has to be plugged into formula (2.21) in order to analyze, which electronic transitions are allowed, while exciting the atom for example with a laser.

The electric field of the exciting laser is described by an external scalar potential V_{ext}. As shown above in formula (2.1), this potential can contribute to the Hamiltonian and cause transitions between eigenstates of the undisturbed atom. It can thus be declared as the electric transition Hamiltonian and reads as

$$\mathrm{H}_{\mathrm{trans}} = e\mathrm{V}_{ext}(\mathbf{r}). \tag{2.22}$$

The exciting scalar potential is situated in the coordinate system of the atom. One can expand the scalar potential $\mathrm{V}_{ext}(\mathbf{r})$ into a Taylor series around the origin with respect to $\mathbf{r}$. The result up to second order is

$$\mathrm{H}_{\mathrm{trans}} = e\left[\mathrm{V}_{ext}(0) + \sum_{k=1}^{3} r_k \frac{\partial \mathrm{V}_{ext}}{\partial r_k}(0) + \frac{1}{2}\sum_{k,l=1}^{3} r_k r_l \frac{\partial^2 \mathrm{V}_{ext}}{\partial r_k \partial r_l}(0) + \ldots\right]. \tag{2.23}$$

This series can be plugged into the inner product of Fermi´s Golden rule. The result is

$$\begin{aligned}\langle\Psi_f|\mathrm{H}_{\mathrm{trans}}|\Psi_i\rangle &= 0 - \sum_{k=1}^{3} d_k E_k(0) - \frac{1}{6}\sum_{k,l=1}^{3} Q_{kl}\frac{\partial E_k}{\partial x_l}(0) + \ldots \\ &= \mathbf{d}\cdot\mathbf{E}(0) + \ldots = \langle\Psi_i|\mathbf{r}|\Psi_f\rangle\cdot\mathbf{E}(0) + \ldots.\end{aligned} \tag{2.24}$$

First-order derivatives of the scalar potential are identified as the components of the electric field of the laser, second-order derivatives by the first-order derivatives of the field. The first term in this expansion becomes zero due to the orthogonality of initial and final states. Products $\langle\Psi_f|x_k|\Psi_i\rangle$ are the components of a first-order tensor named electric dipole transition operator d_k . Products $\langle\Psi_f|x_k x_l|\Psi_i\rangle$ are components of a second-order tensor named electric quadrupole transition operator Q_{kl}. The expansion continues to higher-order multipoles.

The most important part of this expansion is the electric dipole operator d_k. Compared to electric transition operators of higher order, this part can provide a remarkable transition yield even at moderate light intensities. That is because the higher the multipole order is, the lower becomes the transition probability. Thus this operator is mainly dictating, which transitions are allowed in the optical photon energy regime and at moderate intensities.

For experiments in course of this thesis, bare atomic transitions are described by the dipole operator.

The dipole operator can now be used to derive transition rules. Its matrix elements in a basis of initial and final multiple-electron eigenstates represent a vector. (2.23) shows that it reads as

$$\mathbf{d}_{if} = e \, \langle \Psi_i | \mathbf{r} | \Psi_f \rangle. \tag{2.25}$$

Multiple electron dipole transition rules can be derived out of this matrix. However, the derivation is complicated. It is outlined on pages 292 ff. in [33] and pages 224 ff. of [34] and in formula 24 in the appendix of [34]. The transition rate between initial and final states is named S. Here it is called $\mathrm{S_{trans}}$ [4]. Atoms like Cr are described by the LS-coupling scheme introduced in subsection 2.3.5. As shown in section 2.4, for such atoms, states are labelled by a symbol `x´ and multiple-electron quantum numbers S, L, J, and $\mathrm{m_J}$. `x´ refers to the alphabetic or counter-alphabetic enumeration of states having even or odd parity. It is necessary to distinguish between states having the same set of quantum numbers. Using this notation, the transition rate is

$$\mathrm{S_{trans}} \propto \sum_{\mathrm{m_J}\,i,\,\mathrm{m_J}\,f,\,k} \left| \langle \mathrm{x}_i \, \mathrm{S}_i \, \mathrm{L}_i \, \mathrm{J}_i \, \mathrm{m_J}\,_i \,|\, \mathrm{d}_k \, \mathrm{E}_k \,|\, \mathrm{x}_f \, \mathrm{S}_f \, \mathrm{L}_f \, \mathrm{J}_f \, \mathrm{m_J}\,_f \rangle \right|^2 . \tag{2.26}$$

The sum respects the three components of $\mathbf{d}$ labelled by k and the $\mathrm{m_J}$-degeneracy of initial and final states discussed above in subsection 2.3.5. On pages 226 ff. of [34] it is shown how this sum can be converted into

$$\mathrm{S_{trans}} \propto (2\mathrm{J}_i + 1)\,(2\mathrm{J}_f + 1) \begin{Bmatrix} \mathrm{L}_i & \mathrm{L}_f & S \\ \mathrm{J}_f & \mathrm{J}_i & 1 \end{Bmatrix}^2 . \tag{2.27}$$

.

Factors (2 $\mathrm{J_a}$ + 1) and (2 $\mathrm{J_b}$ + 1) respect the $\mathrm{m_J}$-degeneracy and the requirement Δ $\mathrm{m_J} = 0, \pm 1$. For transitions of Cr, values of the product of these factors are tabulated in (Tab. 4.2) in subsection 4.3.4.

The curly brackets in (2.27) represent the Wigner-6J-Symbol. This symbol underlies a certain mathematical requirement, namely the triangular relation $\delta(\mathrm{Ja,\ Jb,\ 1}) \stackrel{!}{=} 1$. This can only be fulfilled if $|\mathrm{J_a} - \mathrm{J_b}| = 0$ or 1. Thus a transition rule for atoms described by LS-coupling is derived, namely $\Delta \mathrm{J} = 0, \pm 1$.

Another transition rule comes from the intrinsic nature of dipole transitions, namely the change of parity. This rule is always restrictive. Combined with the rule for spin transitions, the multiple electron transition rules are

$$\mathbf{\Delta s = 0},\ \mathbf{\Delta Parity = \pm 1},\ \mathbf{\Delta J = 0, \pm 1}. \tag{2.28}$$

[4] Also the original state notation in [34] was replaced with the notation introduced in section 2.4.

These rules played a central role during analysis of the PI spectra outlined in chapter 4.

They are a generalization of the hydrogen transition rules in [31]. $\Delta S = 0$ is no more strict. It becomes less compulsive with increasing atomic number. The reason is the change from LS- to jj-coupling, as described above. This means that transitions between different multiplets, co-called intercombinations, are no more forbidden, although $\Delta S = 0$ transitions are favoured.

In all cases, the change of parity is restrictive.

The rule $\Delta m_J = 0, \pm 1$ was not listed in (2.28) due to the degeneracy of m_J levels in actual experiments. Effects of this degeneracy are described above in subsection 2.3.5. Δm-rules have to do with the alignment of the polarization of the exciting light relatively to the atomic quantization axis. $\Delta m = 0$ holds if the light is polarized parallel to the quantization axis. It is then called π-polarized. If it is polarized perpendicular to the quantization axis, $\Delta m = \pm 1$ and the light is called $\sigma\pm$-polarized.

2.6 PI Spectroscopy and PI Mechanisms

The purpose of PI spectroscopy is to investigate atomic or molecular electronic levels. The basic idea is that after one- or multi-step electric excitation of the species by a laser, the same or some other laser is used to photoionize from an excited level.

It is advantageous to use a tuneable laser for excitation and ionization. While scanning the laser wavelength, direct PI is possible at continuous laser energies above the ionization threshold, as shown in subsection 2.6.1. Thus the wavelengths at which ions can appear are depending on electron level energies. They can only appear, if the laser energy fits to some electronic transition. Plotting the ion yield versus the laser wavelength gives information about the excitation spectrum of the particle. Thus information about the properties of the atom or molecule is obtained. That is the idea of PI spectroscopy.

A chapter of [22] deals with the theory of one- and two-photon excitation and the PI of alkali metals.

The way the most relevant PI experiments had been performed in course of this thesis requires three components.

- Interesting species need to be prepared in a manner to eliminate influences disturbing the atomic properties. Due to their low temperature and weak interaction, superfluid He nanodroplets provide a low-disturbing environment. Furthermore, droplets are transparent for exciting and ionizing laser light. One disadvantage is that the interaction with the He has a significant impact on the electronic structure

of the dopant, as shown below in section 2.7. In subsection 3.1.2, it is described, how the droplets are produced and doped with metal atoms. Look at sections 2.1 and 2.7 to find out more about the droplets.

- One or several tuneable lasers are performing excitation and subsequent PI. Concerning this work, a tuneable pulsed dye laser was used. It is described in section 3.4. The laser needs to have a narrow spectral profile and a sufficiently high energy.
- Thirdly, a device to detect and ideally mass-select the ions is needed, for example a QMS combined with a SEM. These two devices are outlined in subsection 3.1.5.

PI consists of photo-excitation and ionization steps. The theory of excitation is outlined above in section 2.5.

The following two subsections 2.6.1 and 2.6.2 include information about the theory of two different PI mechanisms possible for many atoms, especially for Cr and thus related with this master thesis.

Corresponding sections are 4.3.5 and 4.3.4 in chapter 4.

2.6.1 Direct PI - Born Approximation

Direct PI is modelled as an electric transition between a bound and a free electron wavefunction. Free electron wavefunctions can be approximated by plane waves $|\mathbf{k}\rangle$ characterized by the wave vector $\mathbf{k}$. This is called Born approximation. $|\mathbf{k}\rangle$ are the final states, original states are bound multiple-electron wavefunctions $|\Psi\rangle$. One can analyze the corresponding dipole transition matrix according to formula (2.25) and comes up to

$$\mathrm{S}_{\mathrm{trans}} \propto \langle \Psi | \mathbf{r} | \mathrm{k} \rangle.$$

From this product, the PI cross-section can be derived, as shown on page 180 in [34]. The result is

$$\mathrm{S}_{\mathrm{trans}} \propto Z^5 \left(\hbar\omega\right)^{-\frac{7}{2}}, \tag{2.29}$$

with Z the atomic number and $\hbar\omega$ the photon energy. It is the cross-section for optical excitation from a discrete atomic level into the continuum of ionized states. The photon energy needs to be high enough to reach the lower edge of the continuum. If it is too low, the cross-section is zero. At the threshold, the cross-section makes a jump. This is called absorption edge. The continuum can be reached from different atomic levels. Thus the total direct PI cross-section is an overlay of several absorption edges and looks like in fig. 2.3. Note that this figure is schematically and does not belong to an actual element. The scale is linear.

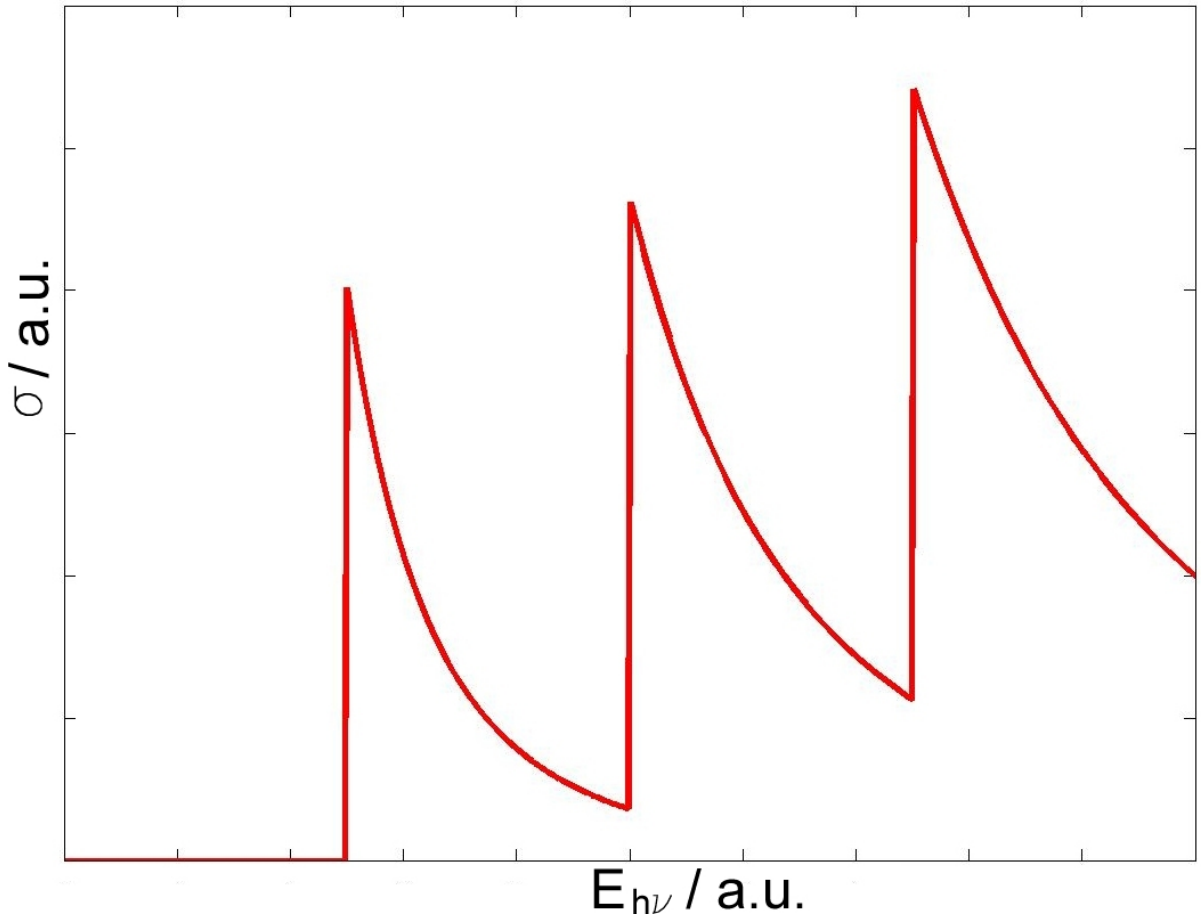

Figure 2.3: Direct PI Cross Section versus Photon Energy

This model is valid for single atoms. Cr PI spectra fig. 4.14 and fig. 4.17 in section 4.3 show a more complicated pattern. The reason for that is discussed in subsection 4.3.5.

Further information about direct PI is found on pages 415 ff. of [34] and pages 160 ff. of [35].

2.6.2 Autoionization - Fano Resonances

Above the ionization threshold, there are discrete levels embedded in the ionization continuum. Energies of these states are discrete; all the electrons are still bond to the atom. Yet the excitation energy is sufficiently high to make the atom become an ion. Electronic correlation effects described in section 2.3 enable the exchange of energy between electrons after excitation. Thus excitations above the ionization threshold may decay into the ionized state. The residual ion is in its ground state, while the evanescent electron takes away the additional energy. This mechanism is called autoionization.

Autoionization is described as an interaction between discrete energy bound states and

unbound continuum states. These had been explained by Ugo Fano and outlined in [4]. The interference between discrete and continuous levels is described, and also the reason why the line profile of the autoionizing states is asymmetric in energy. It is called Fano profile and shown in fig. 2.4 for different parameters. Also the Fano profile can be derived analytically. The asymmetry comes from the interference, which is possible since the discrete levels are embedded in the continuum. The broadness of the Fano profile reflects the lifetime of the autoionizing states.

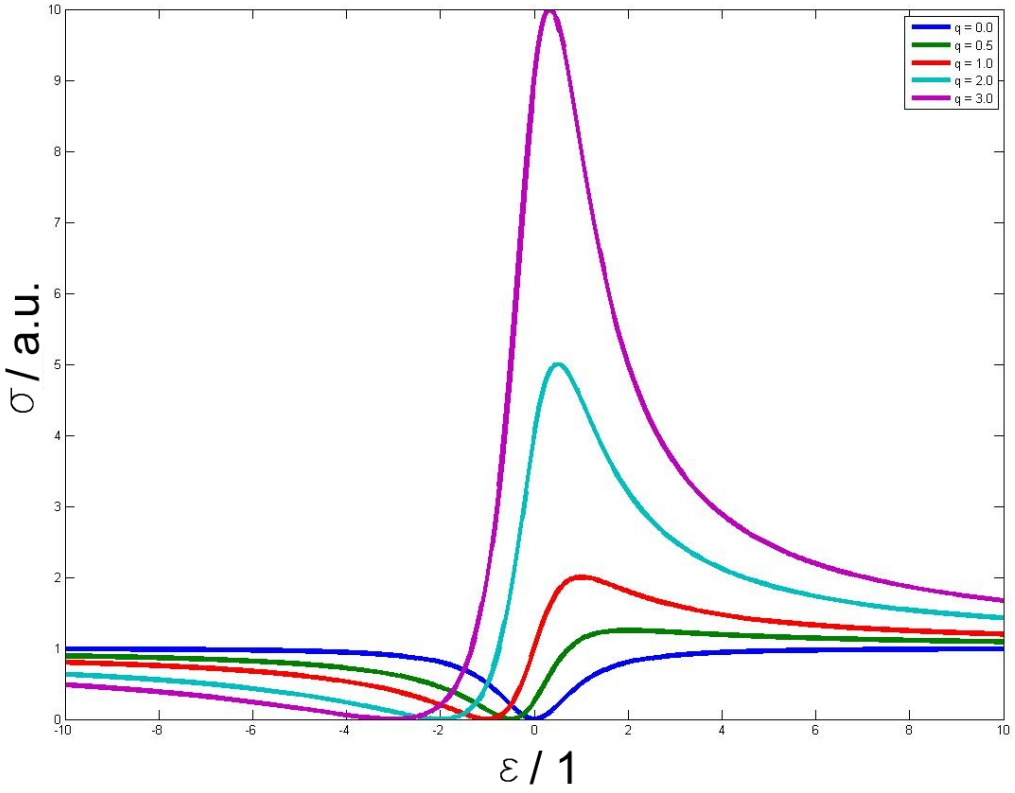

Figure 2.4: Fano Line Profile of Autoionizing States

The Fano profile is defined as

$$\sigma = \frac{(q+\epsilon)^2}{1+\epsilon^2}, \tag{2.30}$$

whereby q is the Fano parameter and ϵ the reduced excitation energy defined by

$$\epsilon = \frac{\mathrm{E} - \mathrm{E}_0}{\Gamma/2}.$$

E is the excitation energy, E_0 is the center energy of the profile and Γ is the line width.

Latest experimental PI results resolved Fano-Resonances of Cr. These results and further information are outlined in [5]. Autoionization and Fano-Resonances are also described on pages 272 and 275 of [34] and pages 220 ff. of [32].

2.7 Interaction between Dopant and He

Spectroscopy on dopants in superfluid He droplets is a key to investigate atomic or molecular electronic structure. Yet the helium surrounding can have an influence on this structure. In [8] a model of how to describe the influence is presented. It is called bubble model. Interaction between dopants and He is a many-body problem and thus very difficult to treat. Fortunately, two simplifications can make this problem much easier to handle.

- He wavefunctions strongly overlap. Thus the He can be approximated as a continuous fluid.
- Pauli Repulsion between the fluid and the dopants makes the He form small spherical cavities around the dopants, so-called bubbles.

That is the reason, why this pseudo-hydrodynamic model is called bubble-model. The total extra energy of the dopant in the bubble reads as

$$\mathrm{E_{tot}} = \mathrm{E_{He\text{-}Dopant}} + \mathrm{E_{Pressure}} + \mathrm{E_{Surface}} + \mathrm{E_{Zero\text{-}Point}}.$$

$\mathrm{E_{He\text{-}Dopant}}$ is the interaction energy between the dopant and the surrounding He. $\mathrm{E_{Pressure}}$ and $\mathrm{E_{Surface}}$ are the pressure-volume energy and surface tension energy. $\mathrm{E_{Zero\text{-}Point}}$ is an increase of zero-point energy due to the location of He atoms at the bubble interface.

Interaction with the He makes the electronic states of the dopant broadened in energy. The electron wavefunctions can couple to radial bubble oscillations. Information about the broadening of Cr levels resolved in course of this master thesis is found in subsection 4.3.5.

The bubble model can also explain another effect. If the electron shell undergoes a transition, its electron density gets redistributed. Following an excitation, electrons are more likely located at positions next to the bubble surface, where they underlie a strong Pauli repulsion. The bubble expands causing increase of the pressure-volume and surface tension energy. Thus extra excitation energy is required for the dopants. Transitions can thus be blueshifted. Latest results highlight a blueshift of $400\,\mathrm{cm^{-1}}$ for excitations from the in-droplet Cr ground state to y^7P. That is relatively low compared to 1600 to $2000\,\mathrm{cm^{-1}}$ for Cr in Kr and Ar matrices, as published in [9].

There are two possibilities of how the dopants can get doped to by the droplets. They can be bond to the droplet surface or located inside the droplets. Broadening and blueshift is higher, if the dopant dips into. The amount of broadening outlined in subsection

4.3.5 is pointing out that Cr dips into.

Quantum chemistry methods like Hartee-Fock, Density Functional Theory and others can give a rise to better understand the He-dopant-interaction. For these methods, another simplification is taken into account. If the dopant stays on the surface, the doped droplet is considered as a pseudo-diatomic molecule consisting of the dopant and one He atom. A diatomic interaction potential can be computed. The shape of this potential curve is a rich source of information. Further information about computational approaches is found in theses [18], [27] and [28].

There is one final effect the He has on the dopant left to mention. Interactions like collisions with surrounding He atoms can enable the violation of the bare atomic transition rules listed in section 2.5.

That might be the case with the ejection from in-droplet y^7P to atomic z^5P without change of parity, as described in subsection 4.3.3.

3 Experimental Setup

Most of the components of the setup had been used and described during former projects. Concerning these devices, this chapter includes only brief information. Sources of more detailed descriptions are mentioned in the following.

The He droplet beam apparatus of CLII was used for the production of Rb- and Cr-doped superfluid He nanodroplets. A detailed description of the He beam apparatus is included in [6], the doctoral thesis of Markus Koch [20] and the master thesis of Johannes Lanzersdorfer [23]. This system was originally developed to investigate alkali metals. It was equipped with a Rb pickup source and later expanded by an electron bombardment Cr source. The latter is described in the master thesis of Martin Ratschek [28]. After finishing the apparatus, the very first experiments had been ESR on alkali metals. Information about this topic including results is found in [6], the doctoral thesis of Markus Koch [20] and master theses of Alexander Volk [29] and Johannes Poms [26].

The ionizing laser beam is created by an excimer-pumped pulsed dye laser system from CLI. The master thesis [21] by Guenther Krois includes information about it. Assistance in development of a laser beam profilometer was also part of this master thesis. The profilometer was finished by Christian Goessweiner. Descriptions are found in his bachelor thesis [17]. The profilometer was used to determine the laser pulse energy density. Further details concerning production and investigation of dopants in He nanodroplets are found in theses of Johann Nagl [24], Gerald Auboeck [16], Alexandra Pifrader [25], Florian Lackner [22] and Moritz Theisen [29].

The complete setup is sketched in fig. 3.1. It shows the arrangement of the devices and pump- and dye laser optical path.

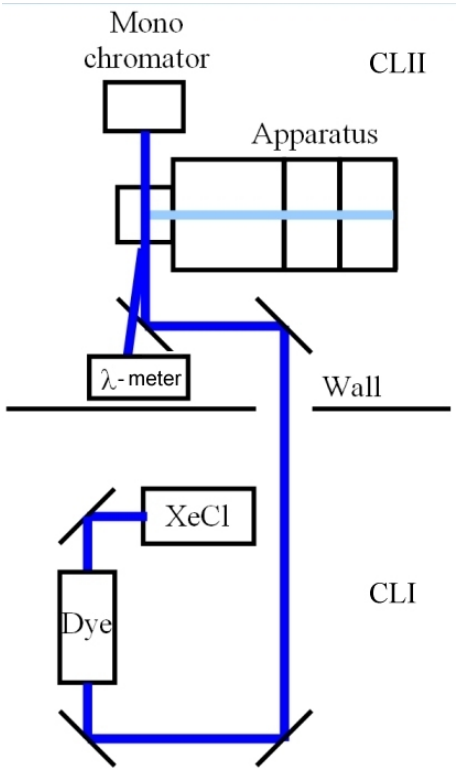

Figure 3.1: Experimental Setup

The following devices are included in the setup:

1. He-Droplet Apparatus
2. Rb Pickup Source
3. Cr Pickup Source
4. Pfeiffer QMG 220 QMS
5. Balzers QMG 422 Main QMS and Equipment
6. Stanford Research Systems SR 400 Two Channel Gated Photon Counter
7. Lambda Physik FL3002 Dye Laser
8. Radiant Dyes RD-EXC-200 Excimer Pump Laser
9. ARC SpectraPro-275 Monochromator
10. Hamamatsu R372 PM
11. Keithley 485 Auto-Ranging Picoamperemeter
12. Stanford Research Systems SR 235 Analog Processor

13. Meilhaus ME-4660 ADC Card
14. Coherent WaveMaster Wavelength Meter (λ-meter)
15. Laser Profilometer
16. CLII PC

The following sections 3.1 to 3.9 include information about every single device. All of them had been applied several times during the experiments described in the following chapter 4.

3.1 He Droplet Beam Apparatus

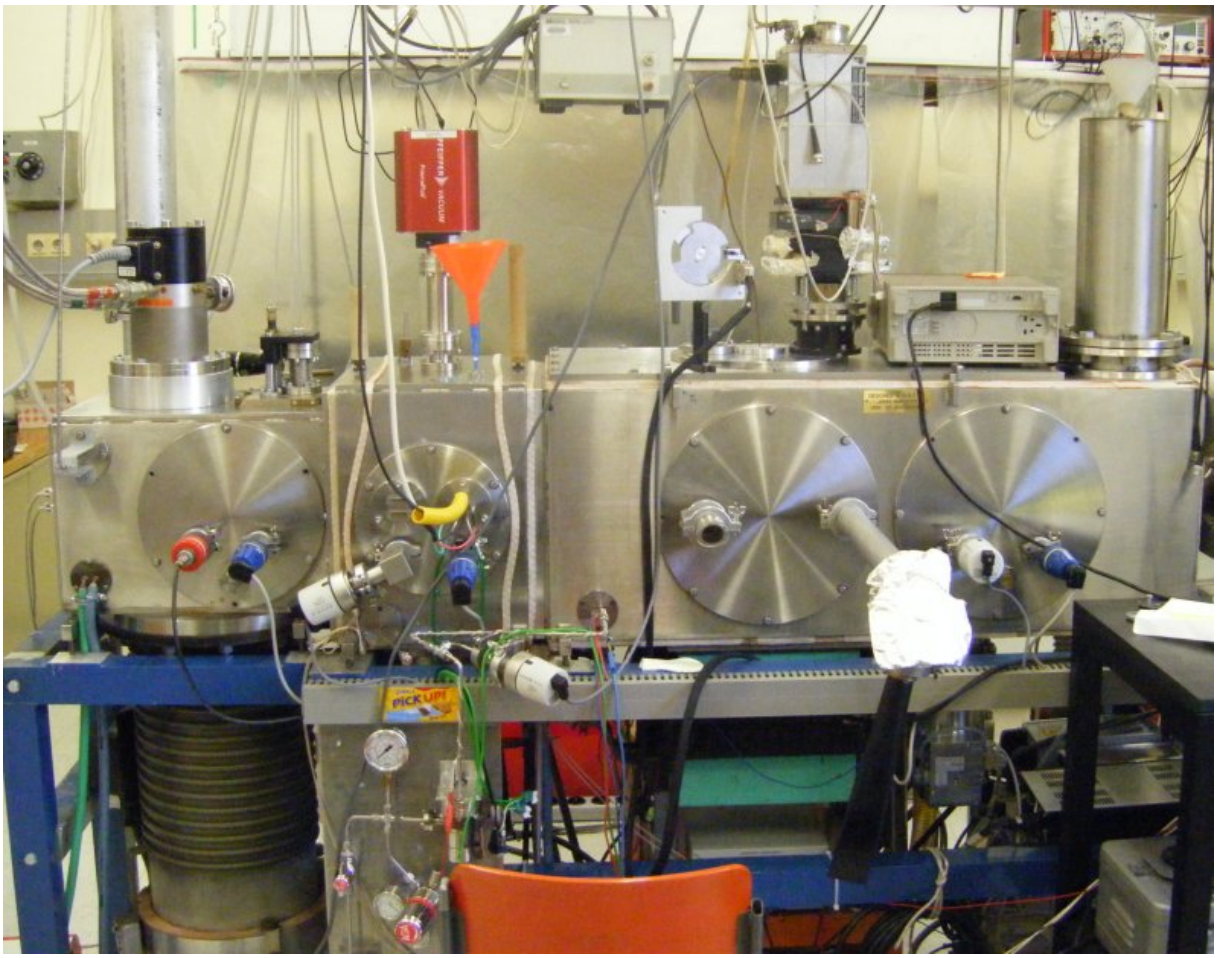

Figure 3.2: He droplet Beam Apparatus Front View

Fig. 3.2 shows the apparatus. It has a fourfold chamber design. Every chamber has its own vacuum system consisting of a prevacuum- and a high vacuum pump. Prevac-

uum pumps are roots, rotary-vane or membrane types, high vacuum pumps are turbomolecular or diffusion type. The operating pressures of the chamber range from 10^{-8} to 10^{-5} mbar, which means high vacuum.

See section 2.2 for further information about Cr and Rb.

3.1.1 Source Chamber

The source chamber is equipped with a cold head. This thermodynamic device uses a two-stage Gifford-McMahon process to cool an isolated nozzle down to a temperature of 10 to 30 K. The nozzle temperature is controlled by electric heating. 99.9999% pure He gets precooled to this temperature. The nozzle has a diameter of 5 μm. He gas goes through a supersonic jet expansion which further cools and leads to condensation into nanometre-sized droplets. High energy atoms can escape from the droplets. Again the He is cooled by this evaporative mechanism. A temperature of 0.38 K can thus be reached. At this temperature, liquid He is superfluid.

A slightly divergent beam of droplets is created by a 200 μm skimmer. It expands to a diameter of around 10 mm at 2 m distance from the nozzle. The droplet size is logarithmically normal-distributed. The expectation value depends on the nozzle temperature and the He pressure, as the left part of fig. 3.3 shows. This subfigure was taken from [20] and is based on the results of several experimenters. At 50 bar He pressure, droplet sizes are suitable for actual experiments at 12 to 23 K. Also the mean droplet velocity depends on He pressure and nozzle temperature, as the right part of fig. 3.3 shows. That subfigure and also fig. 3.4 origin from [23].

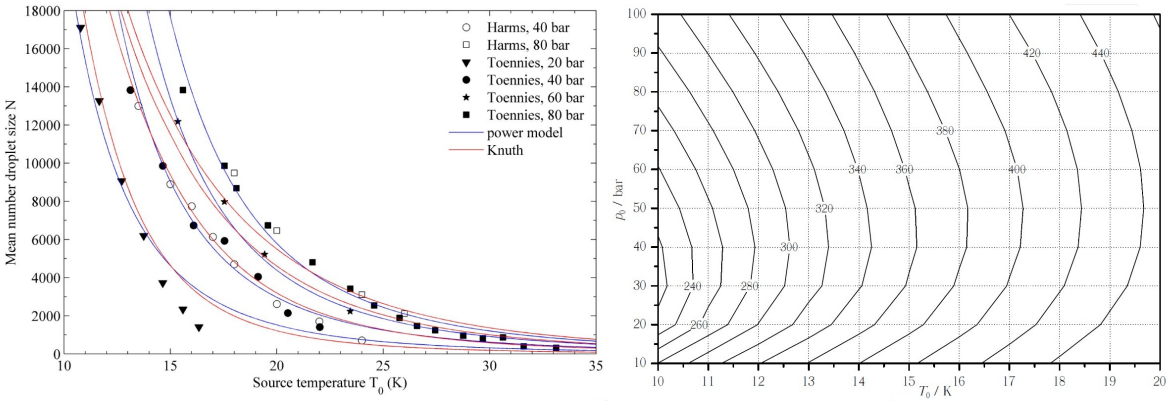

Figure 3.3: Droplet Size and Droplet Velocity

Figures taken from [20] and [23].

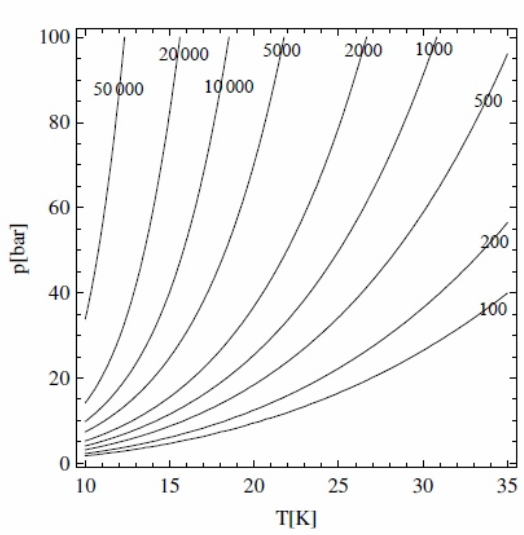

Figure 3.4: Droplet Size

Figure taken from [3] and [23].

3.1.2 Pickup Chamber

The pickup chamber is equipped with pickup sources aligned to the droplet beam. Two different sources had been used. The first one is a cell filled with the alkaline metal Rb. This cell is resistively heated to increase the vapour pressure of the metal. It is heated up to 70 to 100 °C. The temperature is controlled. An effusive atomic Rb beam is formed. As the He droplets fly through the vaporized metal, they can pick up atoms.

Also a Cr source is included in this chamber. The difference between Rb and Cr is that Rb is much more volatile. Cr is vaporized by electron bombardment heating. Electrons are emitted by a heated filament and get accelerated against a Cr crucible by a high voltage up to 1000 V. By collision with the crucible, the electron energy is thermalized. A local temperature of 1650 °C can be reached, as shown in [28]. Thus the metal emits atoms which pass through a slit aperture. Thus an atomic beam is formed. It crosses the droplet beam perpendicular. Unlike Rb, no effusive beam is formed. The heating power is also controlled. It can be set continuously between 0 and 200 W. Fig. 3.5 is showing the Cr source.

The temperature of the Rb source and the heating power of the Cr source are controlling the vapour pressures. Respective values are outlined in section 2.2.

After pickup, metal atoms are trapped in an ultracold container, namely the helium droplet. Further evaporative cooling happens. Metal atoms can interact and form clusters. The He droplet is a low perturbing environment. The picked up species are

relaxed into the ground state. Single atoms and clusters are now ready for investigation. Measurements are performed within the third and fourth chamber, the main- and the QMS-chamber.

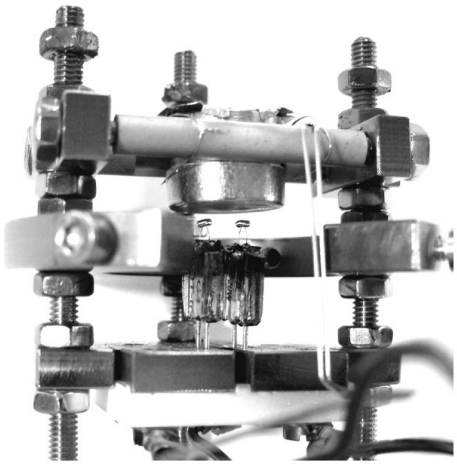

Figure 3.5: Electron Bombardment Cr Source

Picture taken from [11].

Furthermore, a Pfeiffer QMG 220 QMS, as displayed in Fig. 3.6, was purchased for analysis of the residual gas within the pickup chamber. This unit consists of electron bombardment ionization device, the rod system, Faraday cup, secondary electron multiplier and an electronic evaluation device.

Figure 3.6: Pfeiffer QMG 220 QMS

The QMG 220 QMS has a closed cylindrical stainless steel housing. The ion source on top of the rod is the only inlet. Approximately at one third of the rod length, starting from the ion source, there is a CF-type vacuum flange for mounting the whole unit. The QMS was mounted on the pickup chamber such that the ion source is approximately on the level of the chamber wall, as shown in fig. 3.2. This ensured protection and high sensitivity of the system.

Before in-droplet spectroscopy, it was essential to achieve a good vacuum performance. Beside metal dopants, particles from the residual gas may also be caught by the droplets. They can interact with the dopants. Transitions might be quenched and spectra might be distorted. Especially water vapour is suspected to be harmful since water molecules can absorb major parts of the thermal radiation at room temperature. As water is picked up by the droplets, it might act as a tiny antenna for thermal radiation to bring heat into the droplets and destroy them by vaporization. Efforts had been taken to increase the vacuum performance by means of two cold traps filled with liquid nitrogen during all the measurements. Especially the amount of water vapour can thus be reduced.

The QMS selects ionized species by means of their mass. Since Rb and Cr isotopes are medium-heavy atoms, there might exist for example some hydrocarbons having the same masses. If the vacuum chambers contain such hydrocarbons or other species and if they can also be ionized by the laser, the PI signal might thus be biased. Fortunately there exists a method to make such influences non-compulsive. While recording a spectrum, the droplet beam is chopped and the difference between open and closed QMS counts is recorded.

3.1.3 Optimizing Single Cr Pickup

Sections 4.3 and 4.4 describe the approach of PI on Cr-doped droplets. It was decided to focus on single Cr-doped droplets. In the following, it is described how to favor single Cr pickup.

The mean droplet size depends on the He nozzle temperature, as outlined in fig. 3.3 in subsection 3.1.1. Low nozzle temperature means large droplet size, and vice-versa. The He mass flow is nearly independent from the nozzle temperature. Thus either a large number of small or a small number of large droplets can be produced. The larger the droplets are, the more likely they pick up large numbers of Cr atoms. Very small droplets may disappear after pickup due to evaporative cooling. Thus it is necessary to look for optimized He nozzle settings before the measurement.

Also the Cr heating power is playing a role for pickup. The density of metal atoms to be picked up by the droplets depends on the heating power. Thus the corresponding setting also has to be optimized. Due to deposition of vaporized Cr within the source, the pickup conditions underlie severe variations over time.

It was thus necessary to optimize the Cr pickup conditions at the beginning of every experiment. This was done by observing the QMS signal of the desired species, mostly Cr monomers, while changing the Cr source heating power. Fig. 3.7 shows the Cr monomer signal versus heating power. The aim was to find the heating power with maximum QMS signal. Due to hysteresis effects, it is recommended to watch the signal while increasing and decreasing the heating power. The QMS electron bombardment device was used for ionization.

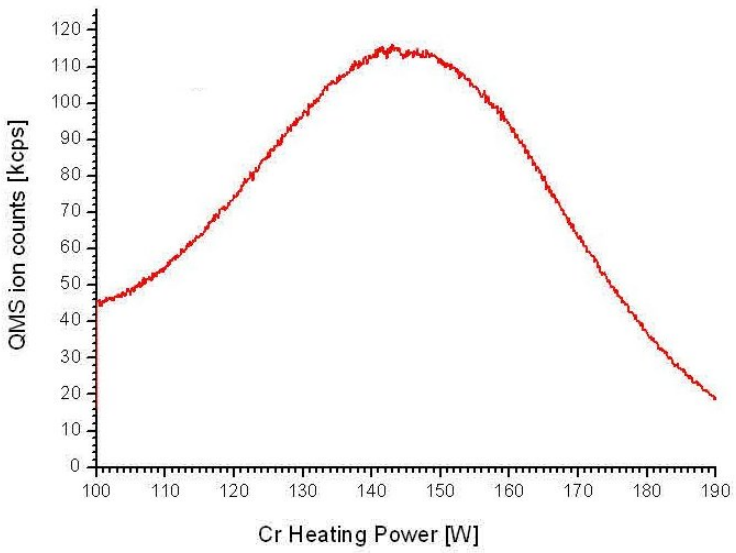

Figure 3.7: Cr Monomer Pickup Yield

Laser dye: Stilbene DMQ, 1.5 mJ max., QMS: 2.5 kV SEM voltage, 52 u, 200 ms counting time, Cr source controller speed: 1.5 %, Rb source: off, ion yield optimized ion extraction region voltages, cold head on: 15 K, 50 bar, date: 23.11.2011, files: QMS1350.txt.

Fig. 3.7 can be compared to a similar pickup curve on page 46 of [11]. It was also recorded at $T_0 = 15\,K$, $p_0 = 50\,bar$ and thus a mean droplet size of 10000 to 12000 He atoms, 2.5 kV SEV voltage and 0.5 mA electron bombardment current. This curve has its maximum of only 35000 cps at 170 W. Higher count rates in fig. 3.7 are due to ion yield optimization by means of ion extraction region voltages shown in (Tab. 3.1).

There are three reasons to explain the shift of the pickup maximum to higher heating power. The monomer pickup maximum corresponds to a density of vaporized Cr the droplet beam has to pass through. On one hand, this density depends on the distance between droplet beam and the slit the vaporized Cr exits from the bombardment source. The temperature of the Cr emitting surface and thus the Cr density is not directly related to the heating power. If the thermal contact between the hot surface and the surroundings is good, the temperature might be relatively low even though the heating power is high. Due to that, the maximum pickup heating power may vary. Thus a pickup curve has to be recorded at the beginning of every measurement day.

3.1.4 Main Chamber

This chamber includes facilities to perform electron spin resonance and laser induced fluorescence experiments. They had not been used during PI spectroscopy. Further information about the facilities of this chamber is found in theses [20], [23], [26], [28] and [30].

3.1.5 QMS Chamber

For PI spectroscopy, the only relevant measuring device within the apparatus is the Balzers QMG 422 QMS located in the fourth chamber. It is useful for analysis of even very low amounts of gaseous species, which are normally ionized by electron bombardment. The electron current ranges from 0 to 1 mA. The species are collected by ion optics in the extraction region and guided to the rod system, where they are mass selected. The single mass, for which the rod system is transparent, depends on the frequency. Filtered ions are detected by a secondary electron multiplier. That SEM is supplied by a DC high voltage up to 2500 V. The parameters of the ion extraction region can be modified. Further information about that can be found in subsection 3.1.3. The left side of fig. 3.8 is an external view of the QMS.

While doing PI, electron bombardment ionization is switched off.

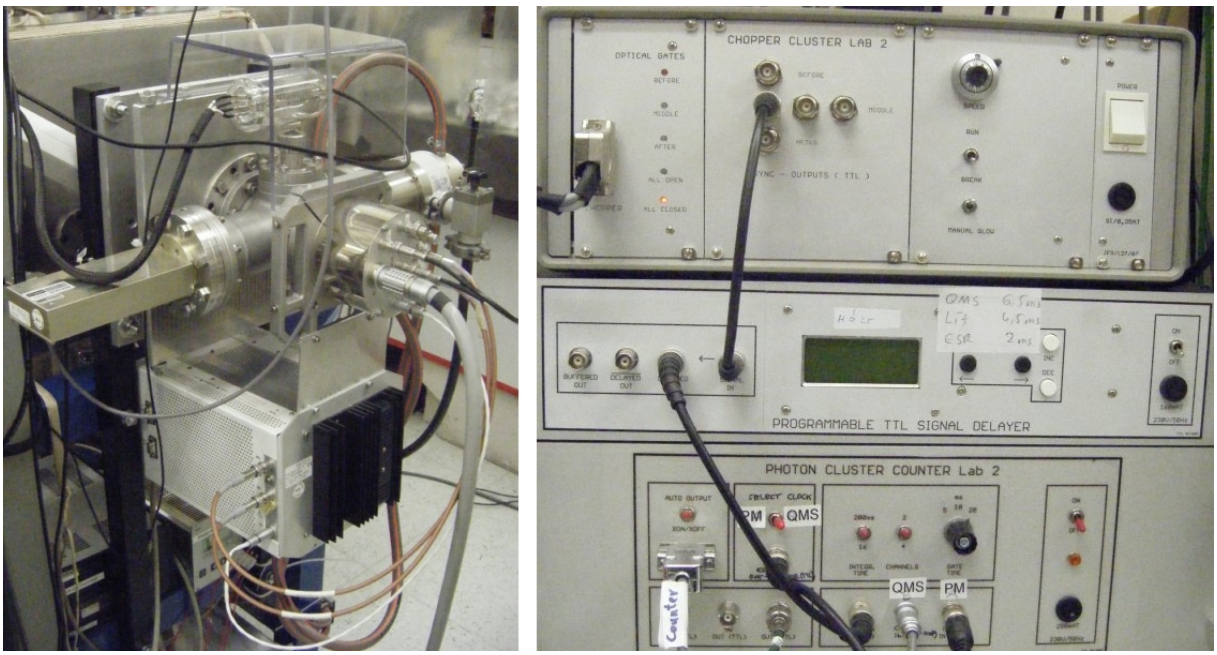

Figure 3.8: QMS Chamber Setup

Left: On top the ionization manometer, from left to right SEM, rod system supply and turbo pump, below the QMS controller, Right: chopper controller, signal delayer and counter.

The SEM creates electric pulses of different height and time lag. The pulses pass a discriminator and are electronically counted. As outlined in subsection 3.1.2, a chopper is needed to distinguish between background and signal yield by the droplets. The chopper has optical switches to determine its state. The states are used as a clock for the counting windows. The chopper is located immediately behind the skimmer, approximately 2 m before the QMS. There is thus a delay between chopper signal and the related interrupt of the droplet beam at the QMS. That delay depends on the beam velocity.

For synchronization, the chopper signal is delayed by a programmable TTL signal delayer. The right side of fig. 3.8 shows chopper controller, signal delayer and counter. This combination had been used during mass scan recordings. The counter is connected to the CLII PC via RS232 and linked into LabView. The counting time can be set to 200 ms or 1 s. The pulsed signal from the QMS SEM is converted to TTL level. For PI spectroscopy, this counter was substituted by a SR400 two channel gated photon counter. That device was connected to the TTL level output gate.

3.1.6 Optimizing Ion Yield

For the QMS, there is a method of increasing the ion yield accepting a lower mass resolution. This method was applied during PI measurements described in chapter 4. To catch ions produced either by PI or electron bombardment, the QMS extraction region is equipped with an electric ion optics system, as shown in fig. 3.9. Seven different voltages can be changed independently to modify the behaviour of the extraction region. Fig. 3.9 is a schematic illustration of the extraction region.

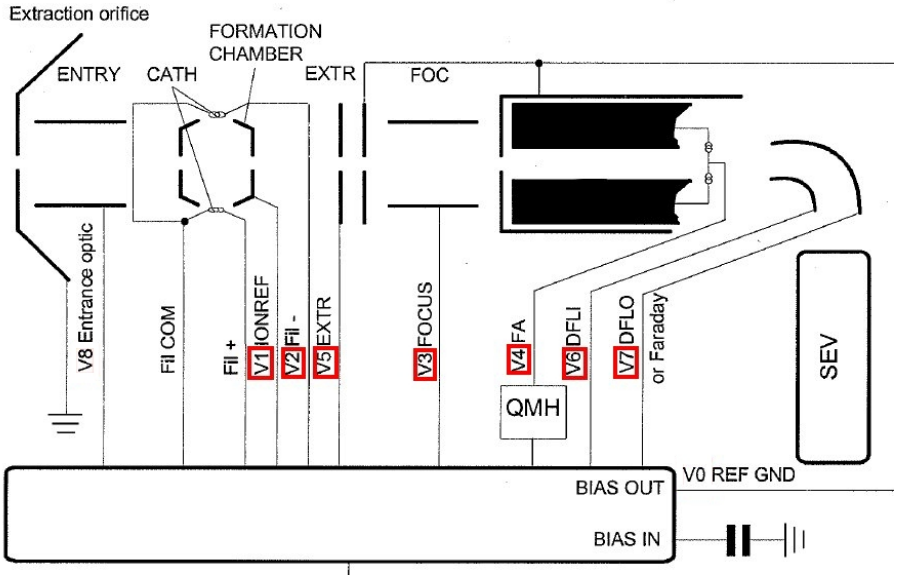

Figure 3.9: Sketch of the Ion Extraction Region

Picture taken from [38].

This illustration is from the QMS manual [38]. Originally these voltages had been set in a way to compromise detected ion yield and mass resolution during mass scans. But for PI spectroscopy, it is less important to have a good mass resolution. Thus the ion extraction region voltages had been changed to achieve high ion yield rather than good resolution. They depend on the mass of the ion species. Table (Tab. 3.1) shows default and optimized values for Rb and Cr. These new voltages had been used for recording the Rb and Cr PI spectra plotted in chapter 4.

Fig. 3.10 shows the effect of voltage optimization. It includes a series of Rb doped droplet mass spectra under different ion extraction region voltages and resolution values. It also shows the impact of changing some QMS parameter called `resolution´. This parameter has something to do with the selectivity of the quadrupole rod system, whereby a high value means a low selectivity. It shows that voltage optimization can indeed increase the ion signal. Increasing the `resolution´, value also leads to a higher signal, but the peaks at certain masses become asymmetric. Their maximum is

Table 3.1: Ion Extraction Region Voltages

No.	U_{def} [V]	$U_{\mathrm{opt,Rb}}$ [V]	$U_{\mathrm{opt,Cr}}$ [V]
V01	100	60	53
V02	70	60	60
V03	15,75	11	11
V04	9	4,25	6,25
V05	300	360	350
V06	300	330	330
V07	110	120	120

shifted below every integer mass value. When combining voltage optimization and high `resolution´, the ion yield is even higher. This figure includes results from Rb doped droplet PI spectroscopy.

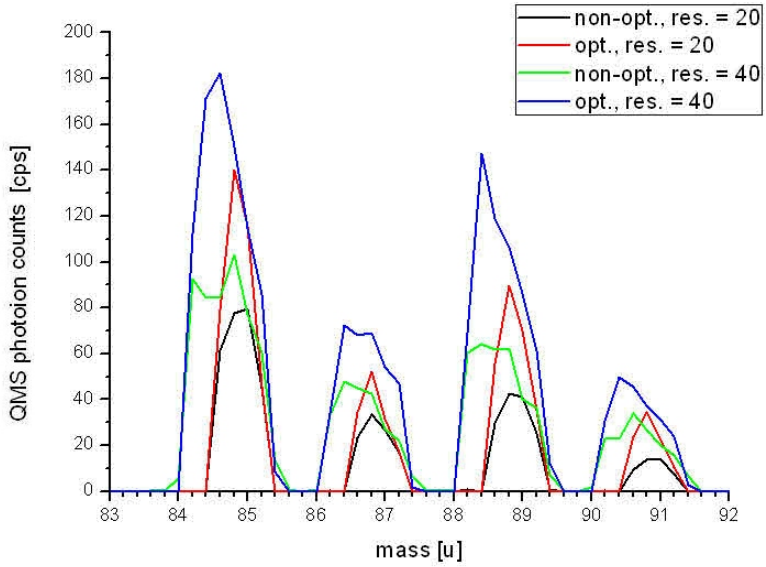

Figure 3.10: QMS Voltage Optimization

Laser dye: Stilbene 3, 1.0 mJ max., 417.4 nm, XeCl laser: 10 Hz, 50 mJ, QMS: 2.5 kV SEM voltage, $\Delta = 0.2$ u, Photon Cluster Counter: 1 s counting time, Rb source: 90 °C, ion yield optimized ion extraction region voltages, cold head on: 17 K, 50 bar. date: 18.11.2011, files: QMS1341.txt, QMS1342.txt., QMS1343.txt., QMS1344.txt.

3.2 SR400

Fig. 3.11 shows the SR400 counter. Unlike the one mentioned before, this counter can be used for gated counting. Thereby a gate is some time interval of counting activity. It is initialized by trigger pulses. The counting stops a specified time after triggering. Counts can also be accumulated over a certain counting time.

These features are very advantageous when dealing with pulsed production of countable species. For example, if one single laser pulse produces ions, they can be counted directly after the pulse. The rest of the time to next pulse, the SEM will give dark counts that should not be detected. After the gate expired, no more pulses are counted. Gated counting avoids signal distortion by means of dark counts.

Also the SR400 has a GBIP connection, which is much faster than RS232. Thus a fast read-out necessary for achieving a good spectral resolution while scanning the laser is provided. Also the counting time can be customized.

The SR400 was supplied by the SEM pulse signal converted to TTL levels from the respective output gate of the other counter mentioned above.

Figure 3.11: SR400 Front View

This device is also linked to LabView.

3.3 Transmission Window

A few reconstructions had been necessary to make the apparatus suitable for PI measurements. For maximum ion yield, it is essential to perform ionization and analysis at the same position. Thus the ionizing laser needs to be guided through the extraction region of the QMS, where it intersects with the He_N beam. The produced ions are exposed to an electric field and thus drawn into the QMS. The left part of fig. 3.12 shows a sketch of the setup, while the right part shows the laser window and the extraction region.

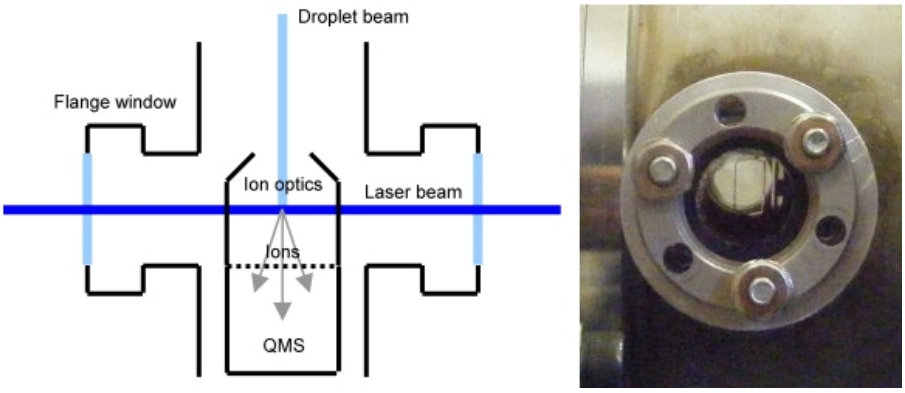

Figure 3.12: QMS Chamber and Flange Window

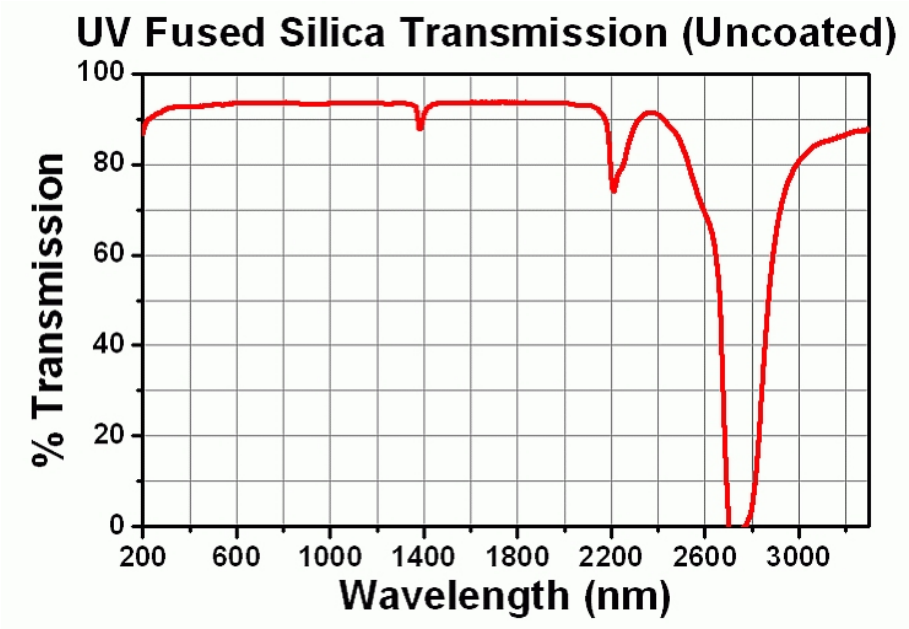

Figure 3.13: Fused Silica Transmission Curve

Picture taken from [44].

The windows are made of fused silica, which is transparent at least from 200 to 2000 nm, as fig. 3.13 shows. The position of the QMS had to be adjusted so that the center of the extraction region aligns with the centers of the windows. The only problem with these windows is that they can act as a Fabry-Perot interferometer for the laser beam. Thus the transmitted intensity oscillates periodically while scanning the laser. Later they had been substituted by wedged windows.

3.4 Laser System

3.4.1 Dye Laser

The ionizing laser beam comes from a Lambda Physik FL3002 excimer-pumped pulsed dye laser. The laser has two dye cuvettes exposed to pump laser light. They are called pre- and main-amplifier. Dye solution is circulating through the cuvettes. The preamplifier cuvette is included in an optical resonator. The resonator has a wavelength-selective grating. The angle of this grating can be changed by a stepper motor drive. Thus the resonance wavelength can be changed. Resonance light is coupled out of the resonator and amplified by transmission through pre-amplifier and main-amplifier. The upper pictures of fig. 3.14 are showing the dye laser with inserted pre- and mainamplifier cuvettes. The lower ones are viewing a dye circulator, dye cuvette and the side view of the cuvette showing the gap for laser transmission.

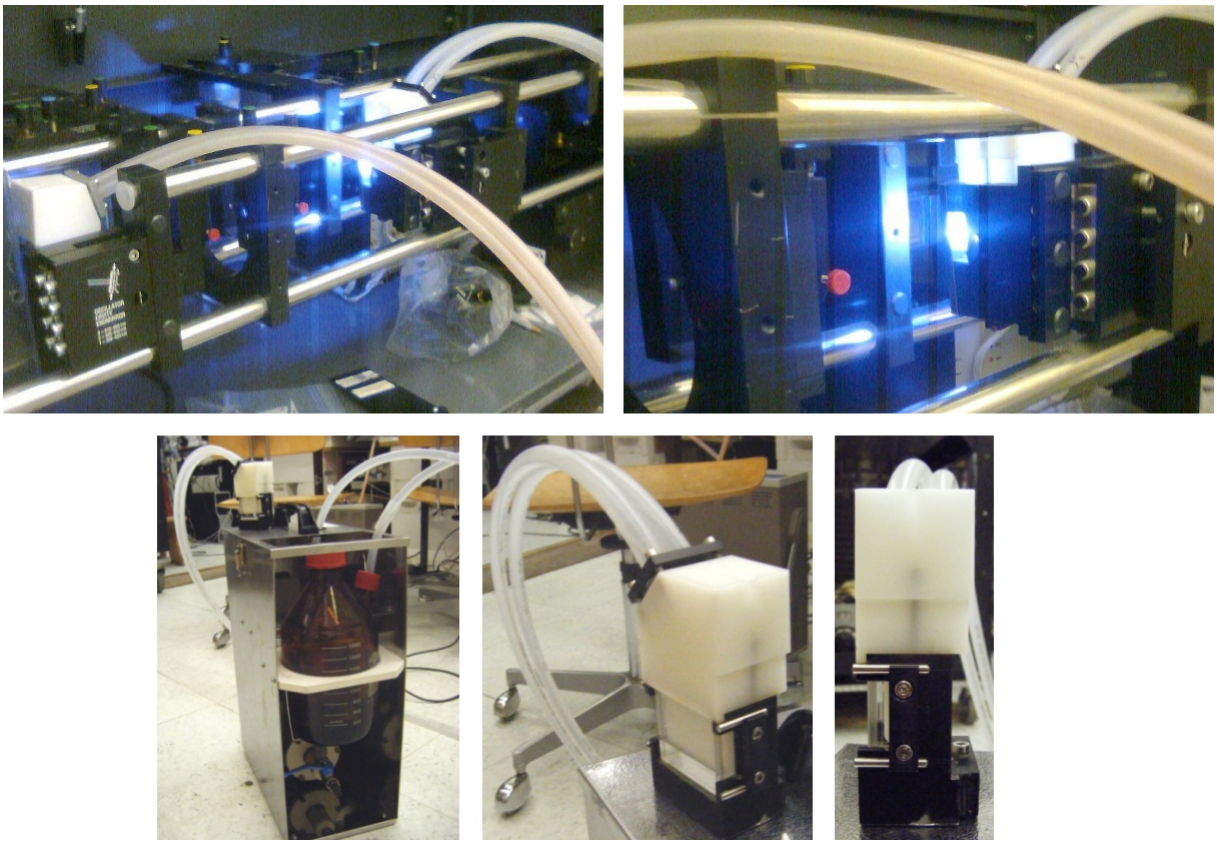

Figure 3.14: Dye laser, Circulator and Cuvette

The tuneability in combination with the possibility of changing the dye solution makes this laser very versatile. It can operate at wavelengths ranging from 300 to 1200 nm. Unfortunately changing the dye means hard work. The circulators need to be flushed. Also the laser needs to be readjusted. Some dyes have a low photochemical stability. In

this case the solution has to be refreshed after one single measurement day.

As fig. 3.1 shows, the exciting beam was transmitted from one lab to another along a total distance of about 12 m. Since it is slightly divergent, a focussing lens is necessary to keep the beam diameter within a few millimetres.

As described in subsection 3.4.5, adjusting the laser was pretty complicated. The task was to reduce amplified spontaneous emission. Adjustment was complicated by the fact that the laser was designed to work the best in the green region of the visible spectrum. Thus the operation in the blue and near ultraviolet region was handicapped.

3.4.2 Laser Dyes

Table (Tab. 3.2) is listing the laser dyes that had been used during experiments concerning this work. It compares tuning range, maximum power and corresponding wavelength, solvents and concentrations, price and photochemical stability as verified in the experiment. The data is from [41] and from an actual Radiant Dyes list.

Table 3.2: Comparing Data of different Laser Dyes

Data taken from [41].

Laser Dye	Tuning Range [nm]	WL of max. Power [nm]	max. Power [mJ]
Stilbene 3	415-432 (blue)	424	1.0
DMQ	350-370 (UV)	364	1.5
PTP	336-347 (UV)	342	0.6
RDC360Neu	338-365 (UV)	355	5

Solvent	Concentration [g/l]	Price 2012 [EUR/g]	Photochem. Stability [Wh]
MeOH	0.65	23	14
DI	0.23	104	1400
DI	0.24	12	450
DI	0.3	112	-

Each laser dye has a specific tuning range. For a Lambda Physik FL3002 dye laser, tuning ranges of all the available dyes overlap and cover the whole visible wavelength region up to near ultraviolet and down to near infrared. In [41], a plot of the set of tuning ranges of all the available dyes can be found. For preparation of a dye solution, 1200 ml of pure solvent had been mixed using a magnetic stirrer. 400 ml of that mixture was then filled into another 800 ml of the solvent. The outcome was 800 ml of preamplifier dye solution and 1200 ml main-amplifier solution having one third of the original concentration. A certain dye may be solved in different solvents. The solvent and also

the concentration have an impact on the dyes spectral emission profile.

Achieved pulse energies ranged up to 5 mJ. Pulse repetition rate and duration time are given by the pump laser. Short-time intensities are much higher than with cw-lasers available in the labs. In subsection 4.3.1, the short time power while using DMQ dye was determined to be 5.0×10^4 W. The CLI and CLII laser having the highest continuous power is an 18 W diode-pumped Pr-doped yttrium-vanadate laser.

The dye laser has a GPIB link. Thus it is possible to remote control the resonator grating using MATLAB from the CLI PC. The PC itself is remote controlled by TeamViewer from the CLII PC. Within MATLAB, there is a routine for setting the laser to desired wavelengths and to perform wavelength scans. MATLAB on the CLI PC is synchronized to LabView on the CLII PC by means of CPU time, as it will be described in [19]. Thus it is possible to create plots of QMS ion counts versus exciting laser wavelength. These are PI spectra as shown in chapter 4.

3.4.3 Pump Laser

The pump laser is a 308 nm XeCl excimer type. The beam has a rectangular profile of about 1×3.5 cm. Pulse energy can be varied by an internal ignition electrode high voltage and ranges up to 100 mJ. The repetition rate can be set to integer values up to 100 Hz. Pulse duration is about 30 ns. After six million repetitions, the lasing gas mixture needs to be refreshed. The left part of Fig. 3.15 shows the closed beam outlet of the pump laser. The right part shows the mirror setup to guide the beam into the dye laser.

Figure 3.15: Pump Laser

3.4.4 Attenuators

For PI measurements, the laser intensity needs to be high enough to create a satisfying ion yield. On the other hand if it is too high, transitions may be saturated. Thus information about transition probabilities at different wavenumbers is lost. The ion yield remains constant while changing the laser intensity. A test procedure of inserting and removing neutral density attenuators and focussing lenses into the laser beam preceded most of the recordings outlined in chapter 4.

3.4.5 Minimizing ASE

Using the monochromator described below in section 3.6, it became obvious that the dye laser light consists of a narrow-banded line and ASE, as shown in subsection 4.1.1. Since stimulated emission is playing a role, ASE is also laser light. But it origins from dye fluorescence and is thus broad-banded. Broad laser spectrum means broad PI spectra. Thus a way of minimizing ASE had to be figured out, as described in the following. The monochromator played an important role for achieving this aim.

Fig. 3.16 shows two spectral laser profiles recorded with the monochromator. If one covers the resonator grating of the dye laser with some piece of paper, the oscillator output becomes much lower and a considerable side-peak appears. This shows the impact of suboptimal resonance on the spectral quality. The constant background is due to dark counts.

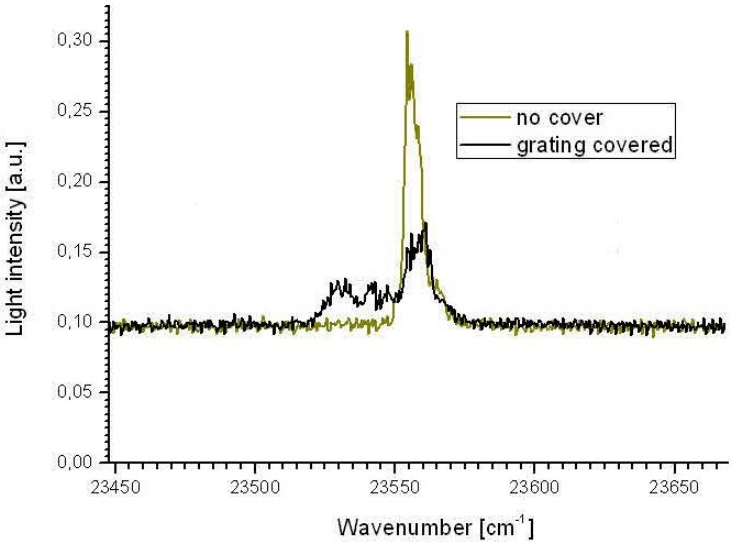

Figure 3.16: Covered and uncovered Oscillator Grating Laser Spectral Profiles

Laser dye: Stilbene 3, 1.0 mJ max., 424.5 nm, 23557 cm^{-1}, 700 V PM voltage, 1 nm/s monochromator scan rate, date: 14.11.2011, files: LaserSpec0088.txt, LaserSpec0079.txt.

It was important to make the resonance process within the oscillator as efficient as possible, accepting lower total pulse energy. Maximizing the resonator output energy means to make it more likely for excited dye molecules to contribute to real laser light rather than ASE. For optimization, a pulse energy powerhead was moved from the laser outlet to the outlet of the oscillator.

But even with perfect adjustment, it is not possible to completely eliminate ASE. For example, if the oscillator grating is set to a wavelength next to the limits of the tuning range of the dye. In this case, the output of the oscillator becomes lower. This it is again more likely for the dye molecules to produce ASE. This is shown in fig. 3.17. The grating was set to several sampling wavelengths. As they approach the tuning range limits, very broad ASE appears around the wavelength of maximum pulse energy of the dye.

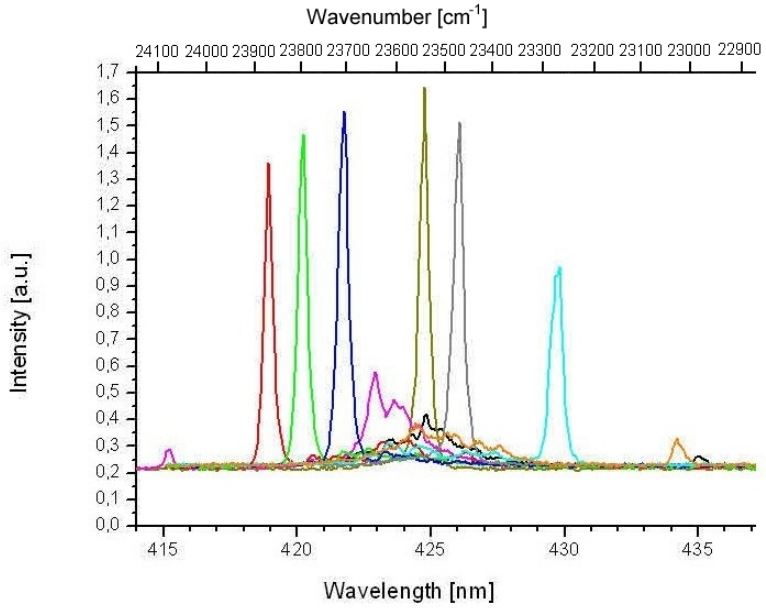

Figure 3.17: Dye Laser Spectral Profile for Stilbene 3

4.0 mJ max., XeCl laser: 10 Hz, 80 mJ, 800 V voltage, 10 nm/s monochromator scan rate, date: 25.01.2012, files: LaserSpec0191.txt to LaserSpec0202.txt.

However, this new kind of adjustment improved the spectral quality. Sharp peaks in the center have a broadening comparable to the monochromator resolution of 0.1 nm. Thus the real broadening might be lower than the resolution.

Especially with Stilbene 3 laser dye, photochemical exhaustion of the active molecules was critical. Given a pump laser pulse energy of 100 mJ, 50 Hz repetition rate and a total effective operation time of 3 hours during one measurement day, the total light energy acted on the dye solution is $0.1\,\mathrm{J} \times 50\,\mathrm{Hz} \times (60 \times 60 \times 3)\,\mathrm{s} = 54000\,\mathrm{J} = 15\,\mathrm{Wh}$. For Stilbene 3, [41] gives a photochemical lifetime of 14 Wh. It is imaginable that this dye solution is exhausted after one single measurement day.

During measurement, the problem was also that while the dye became more and more exhausted, the ratio between small-banded laser light and ASE became lower and lower. It is recommended to prepare some extra dye solution to refill the circulators after exhaustion became too bad.

During Cr PI, two other laser dyes had been used. These are DMQ and PTP. They have between 100 and 1000 times higher lifetimes. There was no need to worry about exhaustion during the measurement. The DMQ pulse energy distribution is displayed in fig. 3.18. Pulse energy was always measured by means of a thermal detector head. The recording shows that with this dye it was also essential but less critical to have a good

oscillator performance.

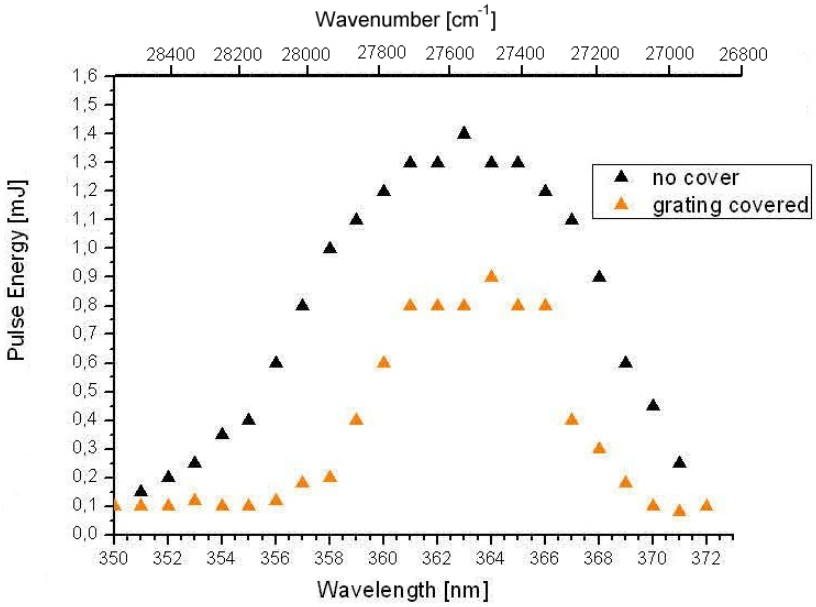

Figure 3.18: Spectral Distribution of DMQ Pulse Energy

XeCl laser: 10 Hz, 60 mJ, laser optimized for low ASE at 356 nm, date: 22.11.2011.

ASE of DMQ also increases if the laser is set next to the limits of the tuning range, as fig. 3.19 shows. Although, compared to real laser peak height, ASE effects are less critical with this dye.

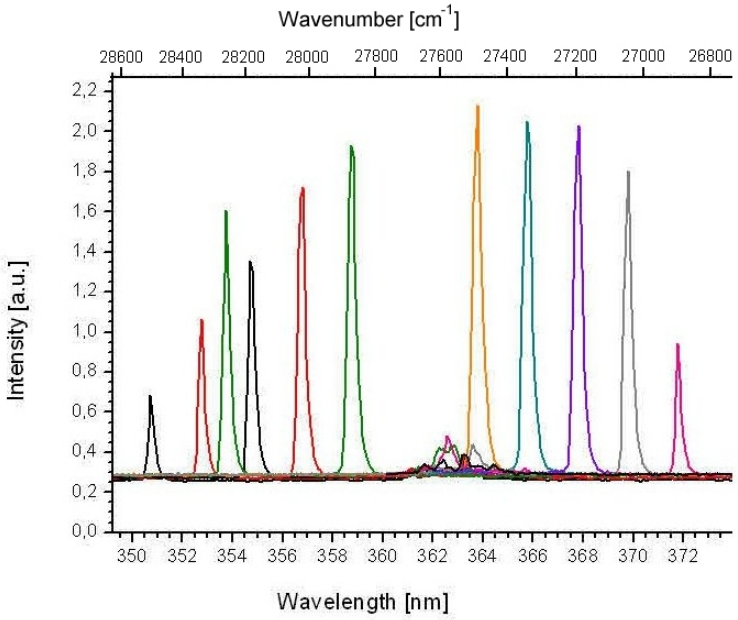

Figure 3.19: Dye Laser Spectral Profile for DMQ

1.0 mJ max., XeCl laser: 10 Hz, 60 mJ, 700 V PM voltage, 10 nm/s monochromator scan rate, monochromator slits widths: 0.06 mm front, 0.035 mm back, date: 5.12.2011, files: LaserSpec0160.txt to LaserSpec0175.txt.

Like with Stilbene 3 in fig. 3.17, well performed peaks in this spectrum are suspected to have a real broadening below the monochromator resolution.

ASE within the amplifier is low at high oscillator pulse energy output and vice-versa. One can thus conclude that ASE yield depends on the laser intensity coming out of the oscillator. At each position within the amplifier, the cross-section profile of the real laser light is non-uniformly distributed. At areas of low intensity, ASE is higher. The spectral quality of the laser may be high in the centre of the beam and decreases outwards. Thus it is useful to screen off the outer parts of the profile using an iris aperture. Or it might occur that the laser spot has some linear extension of high ASE fraction. Therefore a linear aperture is helpful. That aperture should have sharp edges to avoid reflections. A suitable exemplar was designed and constructed. It is shown in fig. 3.20.

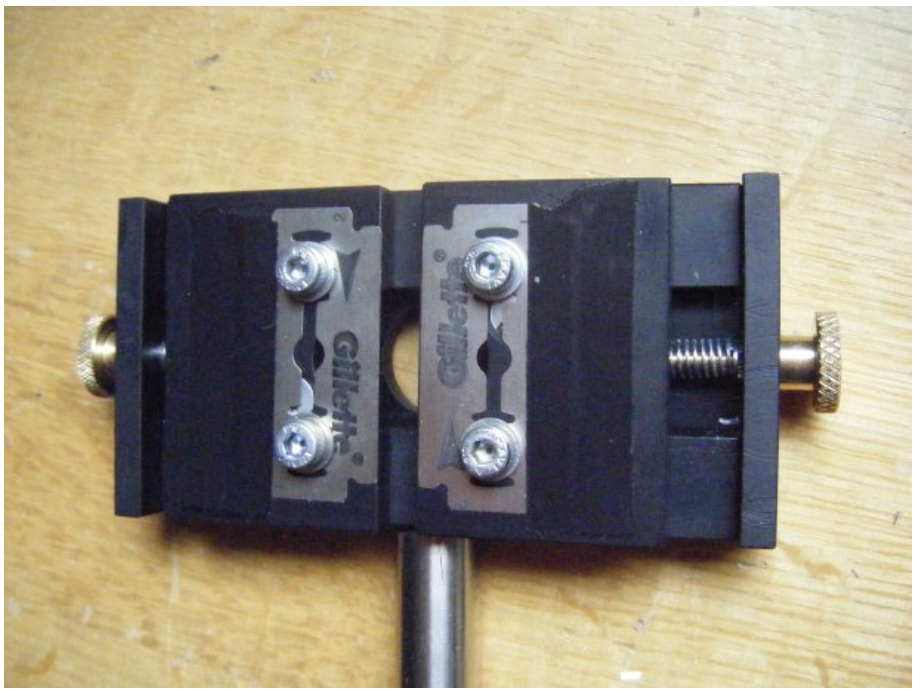

Figure 3.20: Self-developed Aperture

Engineering drawings are found within the appendix. Sharp edges are provided by razor plates.

These efforts could improve the laser spectral quality a lot, as the bare Rb PI spectrum in subsection 4.1.2 shows.

3.5 ADC Card

For controlling and accessing some of the devices of the setup by means of a Meilhaus ME-4660 ADC card, some LabView VIs had been useful. These are modifications of templates from Meilhaus Electronic GmbH. In the appendix chapter 7, these VIs are outlined and described. Fig. 3.21 shows a board of coax connectors for accessing in- and output channels of the card.

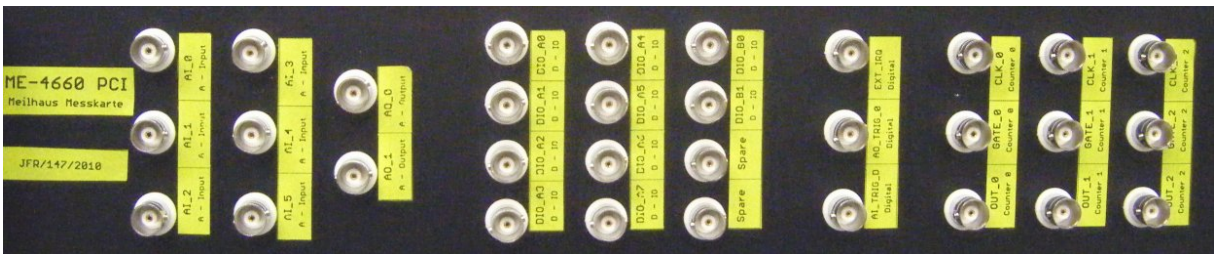

Figure 3.21: Meilhaus ADC Card Connector Board

[40] is giving further information.

3.6 Monochromator

To record precise spectra, it is essential for the laser to be monochromatic. To get information about the laser lights spectral distribution, the ARC SpectraPro-275 grating monochromator was established.

The monochromator wavelength depends on the angle the beam hits the grating, the order of reflection and the grating constant. The grating angle is changed by a stepper motor. That motor is connected to a control unit. At the controller, the transmission wavelength can be selected. Also a wavelength scan under a certain scan rate can be specified.

The monochromator has entrance and exit slits. Both slit widths are adjustable by micrometer screws. Low slit width means high resolution, but low intensity. At the exit slit, there is a PM attached to the monochromator. Since the PM is very sensitive, the laser must not shine directly onto the entrance slit. To make the laser light diffuse by not distorting its spectral distribution, the entrance slit was covered by a small Teflon plate.

The dye laser spectrum was measured using the monochromator. Monochromator scans are thus a key for optimizing the spectral quality of the laser. In course of this master thesis, the 1200 g/mm grating was used. For this grating and entrance and exit slit widths of 10 μm, the wavelength resolution is 0.1 nm at 436 nm. This was determined by using data from pages 5 and 6 of [39]. That was considered to be the achieved resolution for actual scans.

The monochromator control unit is connected to the CLII PC via RS232 and linked to LabView. This makes it possible to use LabView for recording PM intensity versus wavelength light spectra. Fig. 3.22 shows monochromator and equipment.

Figure 3.22: Monochromator, wrapped PM, Control Unit and Power Supply

The PM tube type Hamamatsu R372 was connected to an ORTEC 456H high voltage power supply. This bialkali-type PM tube has a spectral response from 185 to 730 nm, maximum spectral response at 340 nm, 22 ns electron transit time, 1250 V maximum supply voltage and a quantum efficiency of 23% at 320 nm. Further specifications are found in [42]. For most of the measurements, the supply voltage was set to 700 V. The PM was wrapped with aluminium foil to reduce disturbing light. Like with the SEM, dark counts due to thermal influences and also cosmic radiation are playing a role. That noise brought some constant background signal into every recorded spectrum. Just like the SEM, the PM creates electric pulses of different height and time lag. The pulse rate is proportional to the light intensity, as long as the PM is operated within its linear regime. The pulses are transmitted to a picoamperemeter.

The Monochromator-PM-Setup was important for eliminating ASE of the dye laser, as describe above in subsection 3.4.5.

3.7 Picoamperemeter and Analog Processor

Figure 3.23: Picoamperemeter and SR235 Analog Processor

By averaging the pulse signal, one would get a DC signal of respectable voltage, but very low current. The current would be proportional to the count rate and thus to the light intensity. The Keithley 485 auto-ranging picoamperemeter is able to average and measure the pulse current. Its value was proportional to the light intensity. It could thus be used for adjusting the monochromator and recording laser intensity spectra. The left side of fig. 3.23 is a front view of the picoamperemeter. On the right there is the SR235 analog processor.

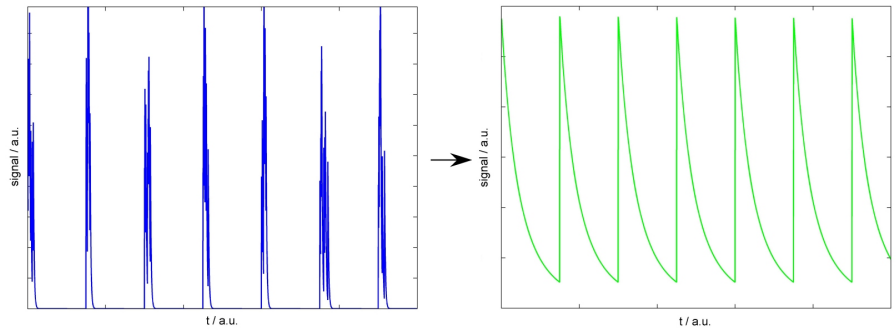

Figure 3.24: PM Signal before and after Picoamperemeter

The picoamperemeter has also an analog output. That output signal reproduces the original pulsed PM signal. Although the fall of the pulse is massively delayed from a few

10 ns to a few 10 ms. The peak repetition rate is now equal to the laser pulse repetition rate. The area underneath the peaks is proportional to the light intensity at the PM. Fig. 3.24 is schematically showing that effect. The signal is then guided to the Stanford Research Systems SR 235 analog processor. This device is shown at the right side of fig. 3.23. The processor function was set to `proportional´ while the internal smoothing capacitors time constant was 30 ms. Thus the analog processor converts the signal into a DC voltage. Also this DC amplitude is proportional to the light intensity. The voltage was measured using an analog input port of the Meilhaus ADC card linked to LabView.

3.8 Wavemeter

The wavelength of the pulsed laser was measured using the Coherent WaveMaster wavelength meter. This device has a special head to couple light into a glass fibre. This head was positioned in a way that the small amount of laser light reflected at the QMS chamber window is coupled into the fibre. The left side of Fig. 3.25 is a front view of the pulse wavemeter. The right side shows wavemeter entrance hat and glass fibre connection to the device.

Figure 3.25: Pulse Wavemeter and Entrance Hat

The wavemeter has an accuracy of 0.005 nm and a wavelength range of 380 to 1095 nm. At 400 nm, ± 0.005 nm corresponds to $\pm 0.3\,\mathrm{cm}^{-1}$. The limited accuracy becomes obvious when comparing measured and tabulated Rb transition lines, as shown in subsection 4.1.3. As described above, dye laser wavelength scans had been synchronized to the LabView signal recorder. In principle the wavemeter was not needed for recording PI spectra. However it gives the wavelength more precisely than the dye laser control. It was also very useful to determine the constant deviation between wavelength the laser controller returns and the real laser wavelength.

Unfortunately the pulsed wavemeter did not work in the wavelength region of DMQ, PTP and RDC360Neu laser dyes, as listed in table (Tab. 3.2) in subsection 3.4.2. Other techniques had to be found to determine the wavelength during a laser scan. Since the monochromator is fully programmable, it was obvious to use it for wavelength determination.

This was done during the first few measurements using UV emitting laser dyes. After starting a laser scan, the LabView VI for recording PI signals was activated. Within this VI, a routine was developed to set the monochromator a few nm above the starting wavelength. Then it waits until the laser line has passed. It records the passing spectral profile. After that the monochromator is set to the next intermediate wavelength. Once again it waits and records the passing profile. This routine continues until the scan is over. For each PI spectrum, the VI provides a series of wavelength marker peaks to interpolate the wavelength.

This method was substituted during Cr measurements. It turned out that the dye laser can be remote controlled using the CLII PC and a GPIB bus. The PC used for recording PI spectra and the laser controlling PC had been synchronized by means of CPU time.

3.9 Laser Beam Profilometer

Several companies offer laser profilometers. Such devices consist of a moveable CCD chip behind some attenuators. The rate of photo-charge-carrier accumulation in each pixel of the chip is proportional to the local light intensity. Thus read-out of the array can give the intensity cross-section profile. The equipment of CLI and CLII does not include such a device. In general, profilometers are very expensive. Yet the laser cross section profile is a very interesting quantity. The aim was to find some low-cost alternative to commercial device. This was part of this master thesis and the main task of the bachelor thesis [17] of Christian Goesweiner.

A Logitech C310 webcam was ordered. This cam has a $3.6 \times 2.7\,\mathrm{mm}^2$ CCD array having a resolution of 1280×1024 pixels. The size of a single pixel and thus the resolution is about $3\,\mu$m. The CCD can be read out by the CLII PC via USB. The laser needed to be attenuated before exposed onto the CCD. For this purpose, a series of neutral density filters was ordered. These had been reflecting filters of optical densities 2 and 3; and also absorbing filters of density 0.3, 1, 2 and 3. The cam, the filters, a laser pointer and a box to shade the setup from daylight had been used for testing. The aim was to find a combination of filters to have a sufficiently high attenuation to record non-saturated but low-noise images. Test profiles are found in subsection 3.9.2.

Based on these results, a low-cost beam profilometer could be developed. It consists of the circuit board of the cam with the CCD, micrometer screw-driven linear slides for moving the CCD, slots for inserting neutral density filters and a robust plastic housing. From left above to right below, Fig. 3.26 shows the Logitech C310 webcam, OD3 absorbing neutral density filters, the profilometer housing and the screw-driven slide fixation of the CCD circuit board.

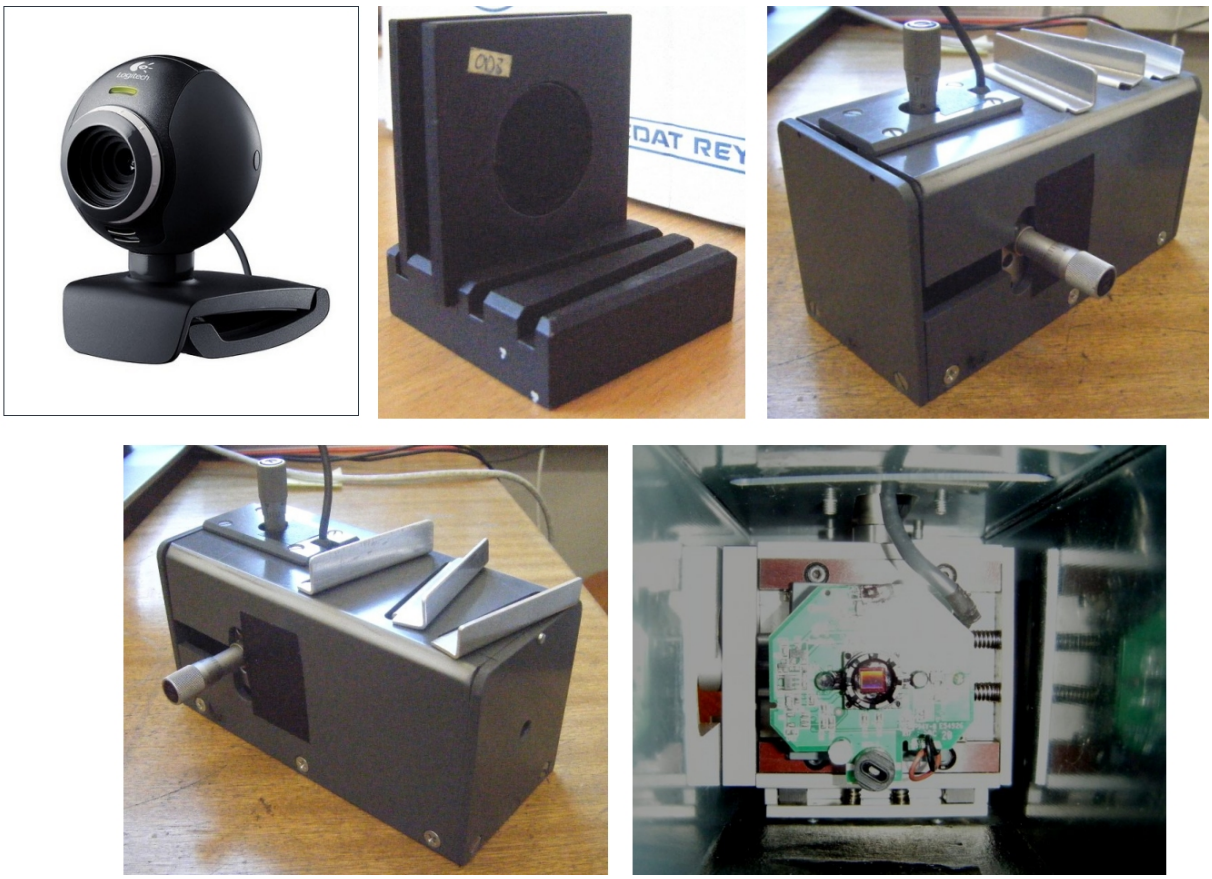

Figure 3.26: Beam Profilometer Equipment

3.9.1 A Method of recording Intensity Profiles

Fortunately, MATLAB provides fairly useful programs for image acquisition from USB camera devices. It was very simple to develop a MATLAB scripts to acquire and process images. Scripts including comments are found in the appendix.

Fig. 3.27 shows three images of attenuated laser beams in real colours. The left image corresponds to the profile fig. 4.5 in subsection 4.1.2 It shows a 425 nm and 1.0 mJ pulse energy laser beam using Stilbene3 laser dye. The middle image shows the spot of a 532 nm diode laser pointer having a laser power of 5 mW. For the right one, the laser settings had been the same as for the left image, though the beam was focussed by a lens.

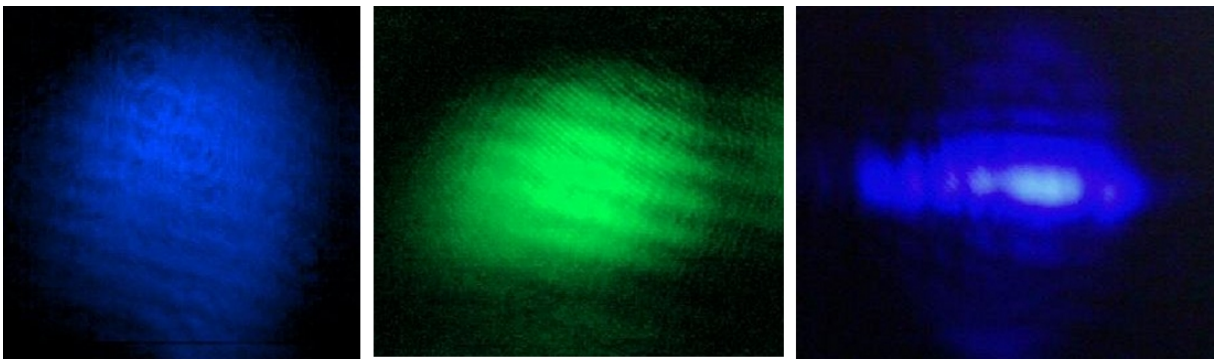

Figure 3.27: Real Color Images of attenuated Laser Beams recorded with the CCD

The left image in fig. 3.27 is without saturation. The middle one is slightly saturated, the center of the image looks monochromatic. The right one shows strong saturation in the center. Thus pixels belonging to the red and green colour channels are also activated and the spot looks white. One can see circular interference patterns due to diffraction at dust particles on the attenuators. Interference lines are considered to be due to Fabry-Perot effects during transmission through the attenuator setup. Note that the horizontal and vertical image sizes comply with $3.6 \times 2.7\,\mathrm{mm}^2$, except for the left image. It was rotated by $90\,^\circ$.

3.9.2 Test Profiles

Since the webcam was designed for entertainment rather than scientific purpose, there was a handicap to overcome. If the CCD is situated in some weakly illuminated room, the webcam controller increases its sensitivity in order to record a fairly bright image. For laser profiles, this behaviour is critical. In most cases a profile consists of dark areas and one small very bright spot. Thus the controller tries to adapt the sensitivity to the dark background rather than the bright spot. The area within the spot is overexposed. Most of the corresponding pixels give the maximum read-out value. The intensity profile is saturated. It looks like a plateau and is far away from proportionality. Fig. 3.28 shows such a plateau. X and Y coordinates are pixel numbers, the Z coordinate is the CCD read-out value in arbitrary units. It represents the light intensity.

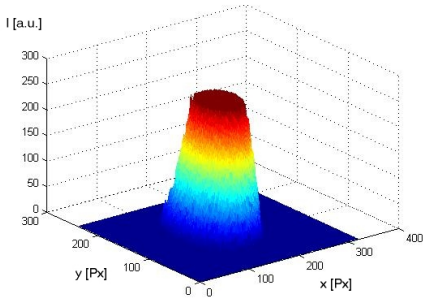

Figure 3.28: Surface Plot of a Beam Profile showing massive Saturation

Attempts to deactivate the sensitivity adaption failed. It turned out the only way to overcome this problem is to attenuate the laser until the intensity is below the adaption threshold. The resisting laser intensity is then comparable to residual room light, which has to be screened. A guideline for avoiding saturation is to attenuate pulse energy down to about 1 μJ. Cw-power has to be scaled to approximately 0.1 mW.

At low laser intensity, noise is playing a role. The left image in fig. 3.29 shows a non-saturated but noisy profile. The noise and also interferences can be eliminated by means of 2D FFT. The profile is transformed into frequency space. High-frequency coefficients are cut off. It is necessary to adapt the cut-off threshold to avoid distortion of the profile. Subsequently, the profile is transformed back to real space. The noise is gone, the profile looks smooth. The right image in fig. 3.29 shows a FFT-smoothed correspondence of the noisy profile. Both noisy and smoothed profile are related to a Stilbene 3 dye laser beam at 425 nm, a pulse energy of 1 mJ and an attenuator setup having a total optical density of 6. Again, X and Y coordinates are pixel numbers, the Z coordinate is the CCD read-out value assumed to be proportional to the light intensity.

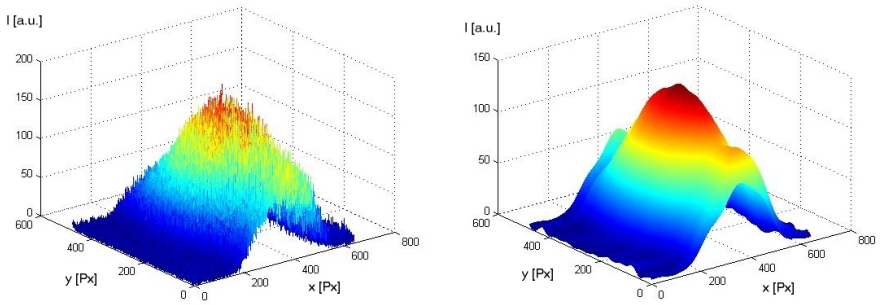

Figure 3.29: Surface Plots of a noisy Profile and the same Profile after Smoothing

It is more insightful to show this data in a 2D pseudocolor plot and adapt the X and Y pixel numbers to the size of the CCD chip. Fig. 3.30 shows pseudocolor plots corresponding to fig. 3.29.

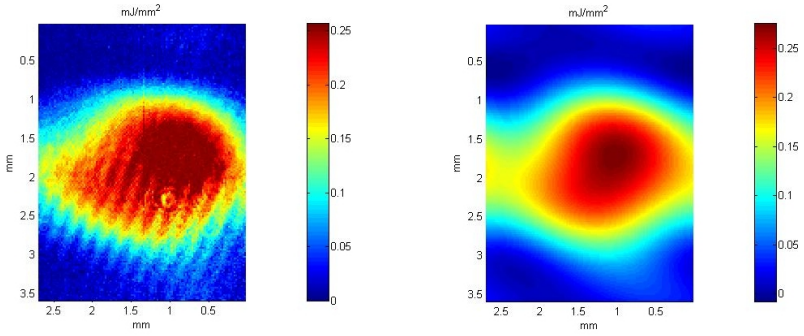

Figure 3.30: Pseudocolor Plots of a noisy Profile and same Profile after Smoothing

We assume a linear relation between CCD read-out value and light intensity. Thus the read-out values can be converted into pulse energy density ρ_E in terms of $\frac{\mathrm{mJ}}{\mathrm{mm}^2}$ using the following relation formula (3.1). By knowing laser wavelength and pulse duration, one can also derive photon density $\rho_{h\nu}$ in terms of $\frac{1}{\mathrm{mm}^2}$ and photon flux $\rho_{h\nu,\,\mathrm{temp.}}$ in terms of $\frac{1}{\mathrm{s\,mm}^2}$ using formulas (3.2) and (3.3).

Formulas are

$$\rho_E = \frac{S}{S_{\mathrm{int}}} \frac{E}{\Delta x\, \Delta y} = \frac{S}{S_{\mathrm{int}}} E \frac{n_x\, n_y}{3.6 \times 2.7 \mathrm{mm}^2}, \tag{3.1}$$

$$\rho_{h\nu} = \frac{\rho_E \lambda}{h\, c\, 1000}, \tag{3.2}$$

$$\rho_{h\nu,\,\mathrm{temp.}} = \frac{\rho_{h\nu}}{T}, \tag{3.3}$$

wherein S is the CCD read-out value, S_{int} the integrated read-out value, which means the sum of all the pixel values of the CCD, E the pulse energy, Δx and Δy the size of one single pixel, n_x and n_y the number of pixel on the CCD, h Plancks constant, ν the laser frequency, λ the laser wavelength, c the speed of light, T the pulse duration.

The size of the whole CCD area is $3.6 \times 2.7\,\mathrm{mm}^2$.

For the laser profiles in the next chapter 4, profilometer and formulas had been applied. Data acquisition, smoothing, imaging, plotting and evaluation had entirely been done in MATLAB. The photon density is needed to calculate excitation and PI yield by means of excitation and PI cross-sections or to determine unknown cross-sections. Thus laser profiles are valuable as an input for a calculation in order to support the experimental results.

4 Experimental Results

This chapter describes the realization of in-droplet PI. It starts with test measurements and goes on towards significant spectroscopic recordings. These are the first Rb PI spectroscopy on the CLII apparatus and the very first in-droplet Cr PI spectroscopy ever done.

Especially for Cr, it was far not obvious how to choose the experimental conditions in order to achieve good results. Therefore a trial and error strategy was necessary. It is outlined in the sections of this chapter.

4.1 Bare Rb Atom PI Spectra using Stilbene 3 Laser Dye

Fig. 4.1 is showing parts of the bare Rb energy level diagram. A two-photon-one-colour process via intermediate levels could be used for PI. While scanning the laser, ions are much more efficiently produced if the energy of the laser photons fits exactly to some transition from the ground state to an intermediate level. The intermediate level energy needs to be higher than half the first ionization energy. Thus should be possible to ionize the excited atom by absorption of another photon.

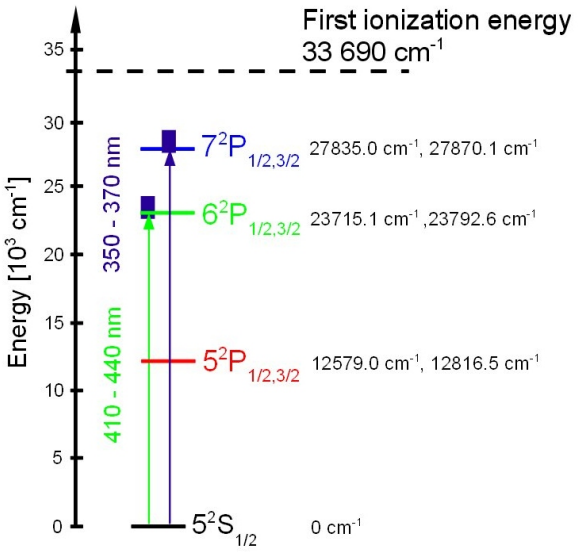

Figure 4.1: Bare Rb Atom Energy Level and Transition Scheme

4.1.1 First PI Measurements

The simplest attempt to start with is investigating atomic Rb. The Rb source was heated while the droplet beam stayed off. Thus an effusive atomic Rb beam was produced. Dye laser cuvettes had been filled with Stilbene 3 solved in methanol. For actual conditions, the tuning range of the dye was 415 to 432 nm or 23200 to 24100 cm^{-1}. The maximum pulse energy is reached at 424 nm or 23600 cm^{-1}.

Within this wavelength region, there are well known transitions from ground state $5^2S_{1/2}$ to $6^2P_{1/2}$ levels at 23715 cm^{-1} and to $6^2P_{3/2}$ levels at 23792 cm^{-1}. They are marked in fig. 4.1. Since the first ionization energy is 33690 cm^{-1}, it is indeed possible to ionize via two-photon resonant absorption.

Thus sharp ion yield peaks at the two respective wavenumbers were expected. Fig. 4.2 shows the related spectrum. Indeed a signal appeared around these two levels. Yet the signal was not sharp.

Using a scan rate of 0.02 nm/s, a peak at 23715 cm^{-1} was resolved. The second peak at 23792 cm^{-1} could only be resolved by lowering the scan rate to 0.004 nm/s. The PI counting time was 1 s, so the resolution is 0.02 or 0.004 nm. At actual wavenumbers, this is equal to 1.1 or 0.2 cm^{-1}. The laser cross-section profile was similar to the one displayed in subsection 4.1.2, although the total pulse energy is lower and thus the energy density. For these spectra, there might be saturation effects. Subsection 3.4.4 describes a strategy of how to avoid saturation. It was applied during subsequent recordings.

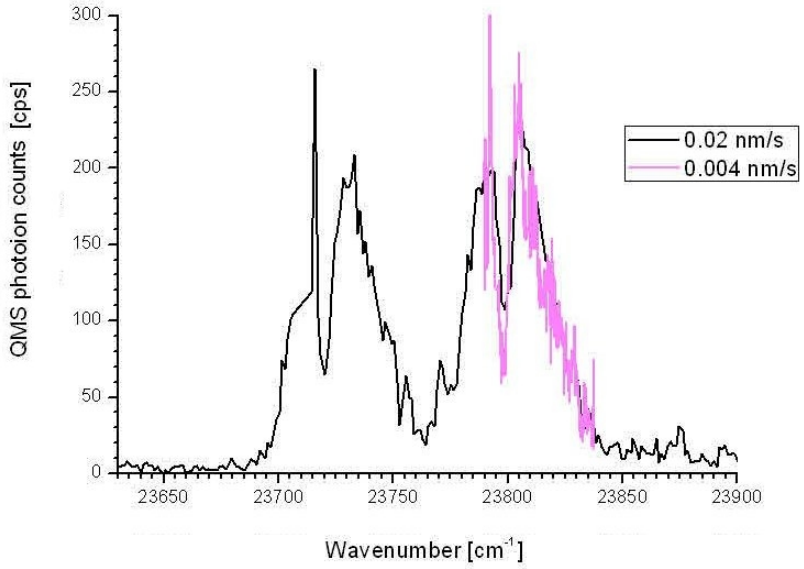

Figure 4.2: Bare Rb Atom PI Spectrum before Laser Optimization

Laser dye: Stilbene 3, 0.3 mJ max., XeCl laser: 100 Hz, 30 mJ, QMS: 2.5 kV SEM voltage, 85 u, SR400: 1 s counting time, Rb source: 90 °C, signal not laser energy normalized, wavenumber measured with pulse wavemeter, cold head off, date: 20.10.2011, files: PI0004.txt, PI0006.txt.

Peaks had been flanked by broad structure. The laser was the first thing to suspect being responsible for that. It looked like the light consisted of a narrow-banded real laser line and ASE. Due to ASE, ions are produced even when the pure laser wavelength did not match to some atomic transition. Broad laser spectrum means broad PI spectra. Thus the aim was to minimize ASE. That procedure is outlined in subsection 3.4.5. At first the idea was to equalize high total pulse energy, good adjustment and low ASE.

Serious efforts had been taken to make the laser pulse energy output as high as possible. It increased from 0.3 to 1.0 mJ at maximum. After this procedure, another spectrum was recorded. It is displayed and compared to the old one in fig. 4.3. Also in this case the laser cross-section profile is similar to the one displayed in subsection 4.1.2. The strategy for avoiding saturation described in subsection 3.4.4 was not applied yet.

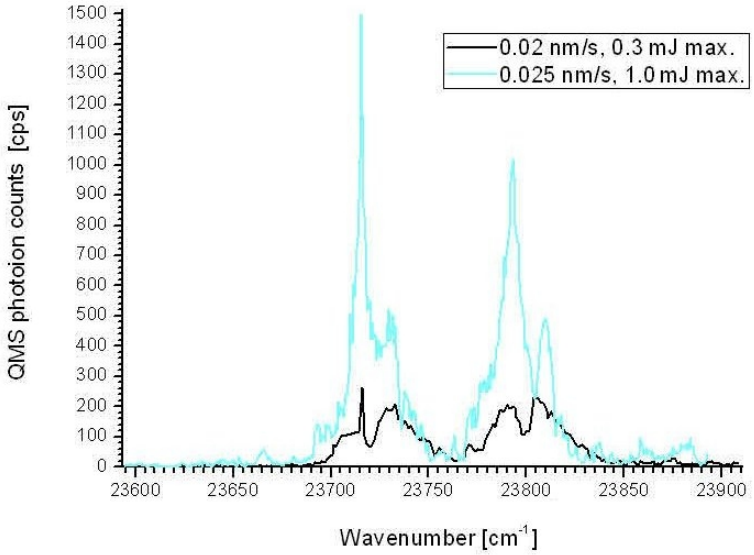

Figure 4.3: Bare Rb Atom PI Spectrum after Laser Pulse Energy Optimization

Laser dye: Stilbene 3, XeCl laser: 100 Hz, 30 mJ, QMS: 2.5 kV SEM voltage, 85 u, SR400: 1 s counting time, Rb source: 90 °C, signal not laser energy normalized, wavenumber measured with pulse wavemeter, cold head off, date: 20.10. and 11.11.2011, files: PI0004.txt, PI0029.txt.

The ratio between single peaks and broad structure became better. But the spectral quality of the laser was still too bad for spectroscopy. Maximizing the laser pulse energy did not increase the spectral quality. Thus it was decided to more precisely investigate how to minimize ASE. That is described in subsection 3.4.5. Furthermore it was tried to optimize the QMS ion yield, as outlined in subsection 3.1.6.

4.1.2 Optimized Bare Rb Atom Spectrum

These efforts indeed improved the performance a lot. As fig. 4.4 shows, the transition peaks from $5^2\mathrm{S}_{1/2}$ to $6^2\mathrm{P}_{1/2}$ and to $6^2P_{3/2}$ could clearly be resolved. The related raw and FFT smoothed dye laser cross-section profile using Stilbene 3 laser dye is plotted in fig. 3.17.

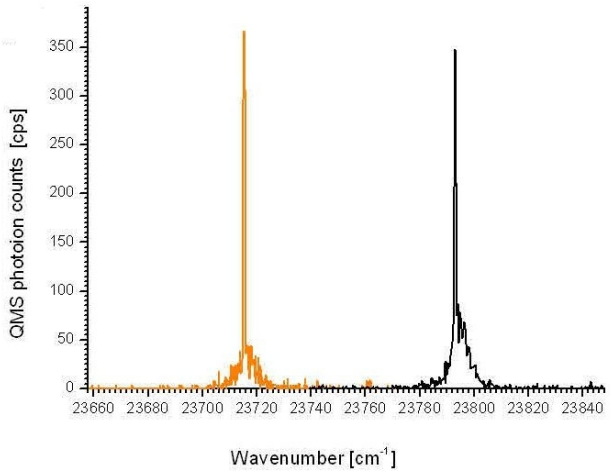

Figure 4.4: Bare Rb Atom PI Spectrum after Low ASE Optimization

Laser dye: Stilbene 3, 1.0 mJ max., XeCl laser: 100 Hz, 30 mJ, QMS: 2.5 kV SEM voltage, 85 u, SR400: 0.5 s counting time, Rb source: 100 °C, signal not laser energy normalized, wavenumber measured with pulse wavemeter, ion yield optimized ion extraction region voltages, cold head off, date: 16.11.2011, files: PI0047.txt, PI0051.txt.

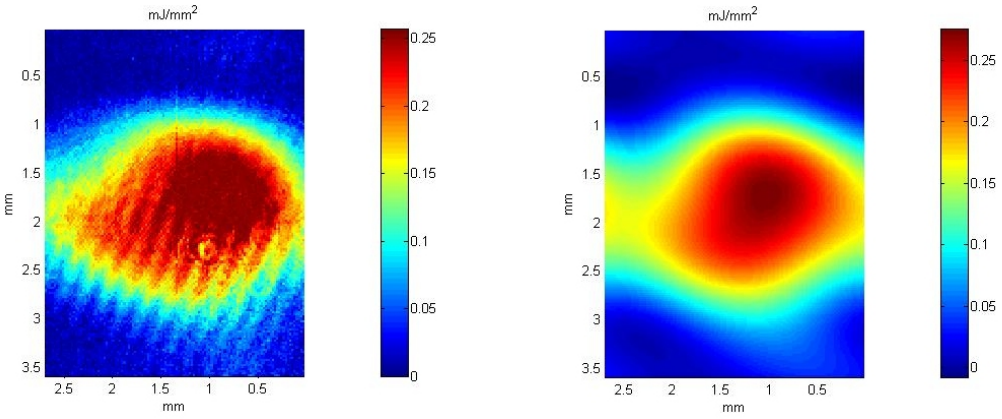

Figure 4.5: Raw and FFT smoothed Laser Profile

1.0 mJ pulse energy, 425 nm, date: 16.11.2011, files: Profile_STB3_20111111.mat.

For this profile, the maximum pulse energy density was about 0.26 $\frac{\text{mJ}}{\text{mm}^2}$. To determine the maximum photon density, relations (3.1) - (3.3) from subsection 3.9.2, a laser wavelength of 425 nm and a pulse duration of 30 ns was used. The result was 5.6×10^{14} $\frac{\text{Photons}}{\text{mm}^2}$

total per pulse and $1.9 \times 10^{21} \frac{\text{Photons}}{\text{s mm}^2}$ during the pulse. The maximum short-time power density was $8.7 \times 10^3 \frac{\text{W}}{\text{mm}^2}$ and the total short time power was 3.3×10^4 W.

4.1.3 Fitting the Spectra

Dealing with bare Rb transitions, there was yet another interesting thing to consider. The spectra in fig. 4.4 can be fitted. They consist of a sharp peak and a minimized but still present background. The sharp peaks are interesting features. The background is due to slight misalignments and can be eliminated by fitting it to a Gaussian, as shown on the left side in fig. 4.6. Only the sharp peak represents the Rb transition.

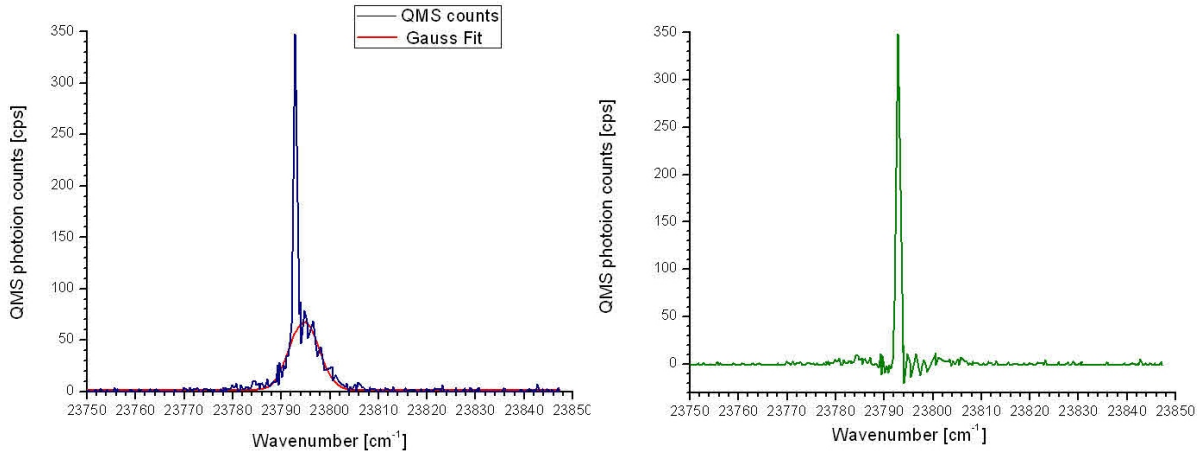

Figure 4.6: Gauss Fit and Residuals of Bare Rb PI Spectrum

Settings like in fig. 4.4, date: 16.11.2011, files: PI0051.txt.

Now the sharp peaks could be fit to a Gaussian and a Lorentzian function. The Formula for a Lorentzian is

$$y = y_0 + \frac{2A}{\pi} \frac{w}{4(x - x_c)^2 + w^2} \tag{4.1}$$

and for a Gaussian

$$y = y_0 + \frac{A}{w\sqrt{\frac{\pi}{2}}} \, \mathrm{e}^{-2\left(\frac{x - x_c}{w}\right)^2}, \tag{4.2}$$

wherein y is the function value, y_0 the offset, A the area under the curve, x_c the center of the peak, w the doubled standard derivation of the Gaussian and the full width of half maximum of the Lorentzian. Fits are shown in fig. 4.7. The Gaussian was considered to better fit to the data than the Lorentzian.

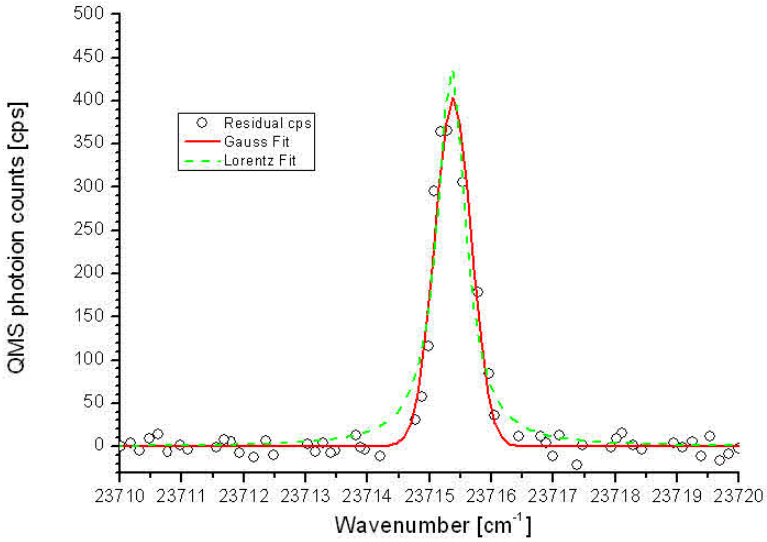

Figure 4.7: Gauss and Lorentz Fits of Residual Rb PI Spectrum

Settings like in fig. 4.4, date: 16.11.2011, files: PI0047.txt.

(Tab. 4.1) is listing the resulting fit parameters for Gaussian fits of the peaks at both wavelengths (G1,G2) and a Lorentzian fit of the peak at 23715 cm^{-1} (L1). The quality is given by the adjusted R-square values.

Table 4.1: Fit Parameters

Variable	G1	ΔG1	G2	ΔG2	L1	ΔL1	Unit
y_0	0.0	0.2	-0.1	0.2	-0.6	0.3	cps
A	295	3	371	5	384	5	cps
w	0.585	0.006	0.83	0.01	0.56	0.01	cm^{-1}
FWHM	0.689	0.007	0.98	0.01	0.66	0.01	cm^{-1}
x_c	23715.375	0.003	23792.91	0.01	23715.353	0.004	cm^{-1}
R-square	0.96415	-	0.966	-	0.94223	-	1

Note that the FWHM of a Gaussian is derived from the doubled standard derivation using the relation

$$\mathrm{FWHM} = \sqrt{2\ln 2}\, w.$$

What is the reason for the broadness of these peaks?

For the transitions from the $5^2\mathrm{S}_{1/2}$ ground state of Rb to $6^2\mathrm{P}_{1/2}$ and $6^2P_{3/2}$, [43] is

listing Einstein coefficients A_{ik} of 1.50×10^6 1/s and 1.77×10^6 1/s. Lifetimes of these excitations are the inverse of the Einstein coefficients. These are 0.67 and 0.56 μs.

Via the energy-time uncertainty principle, lifetimes are related to the transitions natural line widths. For discrete levels, the corresponding profile is Lorentzian. Its FWHM is identified with the Einstein coefficient by relation 5 on page 159 of [34]. From the Einstein coefficients, one can derive the FWHM in terms of cm^{-1} using the relation

$$\Delta\overline{\nu} = \frac{0.01}{c} A_{ik},$$

with c being the speed of light. Results are $5.0 \times 10^{-5}\,cm^{-1}$ and $5.9 \times 10^{-5}\,cm^{-1}$, or 1.50 and 1.77 kHz

Lifetime is related to natural line width. The relation above also holds for two step resonant PI. Peak profiles are probability distributions. At every wavelength, the probability of a two step process is the product of the two steps single probabilities. For the ionization step, the probability is nearly equally distributed in wavelength. Thus the PI profile is proportional to the excitation profile, natural line width are the same.

Results for the natural line widths ranged at $10^{-5}\,cm^{-1}$, which is very small compared to the w-values in (Tab. 4.1). Thus it is obvious that the broadening origins from other effects than energy-time-uncertainty. Two other reasons have to be considered.

1. The laser spectral profile could have been broadened. During PI, this broadening was transferred to the spectrum. In subsection 3.4.5, the laser broadening was suspected to be lower than the resolution of the monochromator.

2. The laser crosses the effusive Rb beam perpendicular. Thus a first order Doppler broadening was out of question. The second order Doppler Effect is due to special relativity. Since Rb is a fairly massive atom, the average thermal velocity at 100 °C is diminishingly small compared to the speed of light. Thus the second order Doppler effect could also be neglected.

The conclusion is now that the broadening of the $5^2S_{1/2}$ to $6^2P_{1/2}$ and $6^2P_{3/2}$ Rb lines is due to the laser spectral profile. The half values of the w parameters in (Tab. 4.1) are carefully rounded to $0.4\,cm^{-1}$. This value represents now the spectral broadening of the laser light.

Since the transition lines are narrow now, the procedure was considered to be good enough to stop effusive Rb test measurements and start investigating Rb-doped nanodroplets.

As listed in (Tab. 4.1), the gaussian fit results for the line centers are 23715.375 and $23792.91\,cm^{-1}$. [43] is giving 23715.081 and $23792.591\,cm^{-1}$. The derivations seem to be due to the limited accuracy of the wavemeter. It is $\pm 0.3\,cm^{-1}$ at 400 nm, as shown in section 3.8.

4.1.4 Conclusion

In accordance with the level scheme fig. 4.1, two bare Rb transitions had been observed. ASE had been reduced. The QMS Rb ion yield was increased by optimizing the voltages of the ion extraction region. A procedure to avoid saturation of the transitions was figured out. Improving the procedure made it possible to precisely resolve the transition lines. The agreement of the centers of these lines and tabulated Rb lines is limited by the accuracy of the wavemeter. The standard derivation of the gaussian spectral profile of the laser light is $0.4\,\mathrm{cm}^{-1}$. The procedure was considered to be good enough to go on to two-photon-one-colour PI of Rb in droplets.

4.2 Rb-doped Droplet Spectra using Stilbene 3 Laser Dye

For Rb-doped droplets, two-photon-one-colour PI should be feasible at the same energies bare Rb transitions exist. Thus the Stilbene 3 laser dye can again be used. The spectrum was expected to include the same peaks shown in fig. 4.4, because effusive bare Rb was still present. However, the spectrum should also include broadened in-droplet excitation and PI transition curves. The $RbHe^+$ PI spectrum should be similar, although without bare Rb peaks.

Concerning Rb-doped droplets, there exists some knowledge about how to set parameters to come to good experimental results. It was based on former investigations of Rb-doped nanodroplets and PI experiments on the CLI apparatus, as they are described in [14]. It was also interesting to record a dimer PI spectrum and mass spectra.

4.2.1 First Measurements

Due to already gathered know-how about Rb-doped droplets, it was relatively easy to lead over from bare Rb atom to Cr-doped droplet PI. It was clear how to set the He nozzle temperature, the He pressure and the temperature of the Rb source. Fig. 4.8 shows the first Rb droplet PI signal.

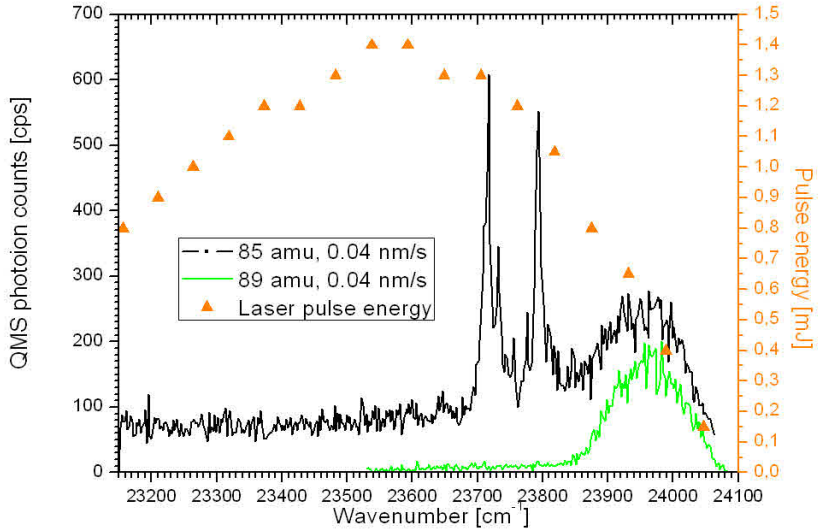

Figure 4.8: First Rb doped Droplet PI Spectrum

Laser dye: Stilbene 3, 1.5 mJ max., XeCl laser: 10 Hz, 60 mJ, QMS: 2.5 kV SEM voltage, 85 u, SR400: 0.5 s counting time, Rb source: 85 °C, signal not laser energy normalized, wavenumber measured with pulse wavemeter, ion yield optimized ion extraction region voltages, cold head on: 17 K, 50 bar, date: 18.11.2011, files: PI0071.txt, PI0072.txt.

Beside the He droplet beam, there was still an effusive beam transporting bare Rb atoms to the QMS. Both beams can contribute to the 85 u PI signal. That is the reason for the two sharp lines at 23715 cm^{-1} and 23792 cm^{-1} to remain in this spectrum. The rest of the signal comes from two step excitation and PI of in-droplet Rb.

Rb PI findings from ClusterLabI helped in explaining this data. The bump in fig. 4.8 seems to consist of the blueshifted and broadened in-droplet correspondence of the two effusive lines from $5^2S_{1/2}$ to $6^2P_{1/2}$ and to $6^2P_{3/2}$.

In the droplet, excited Rb atoms may catch surrounding He atoms to form nonstabile $RbHe_n$ molecules. Such molecules can entirely be ionized. They are detected by the QMS at 85 u and multiples of 4 u. Indeed a $RbHe^+$ signal was observed during this test measurement. It is also plotted in fig. 4.8.

The $RbHe^+$ spectrum looks quiet similar to the bare Rb spectrum. That is not astonishing! Current settings assured that the signal mainly represents the in-droplet excitation spectrum. $RbHe_n^+$ are formed after excitation. Excitation acts the same way for both

species. The advantages of mass-selective PI are shown here. Each spectrum of a different species is a separate source of data. Combining them can give a lot more information.

Also a dimer PI spectrum can include valuable information. Fig. 4.9 shows such spectra. 172 u is the mass of a dimer consisting of a ^{85}Rb and a ^{87}Rb atom, while a pure ^{87}Rb dimer weights 174 u. The dimer ion yield is bad and thus the signal-to-noise ratio is low. No spectral structure could be resolved, but at least it is useful to know that dimers can be produced.

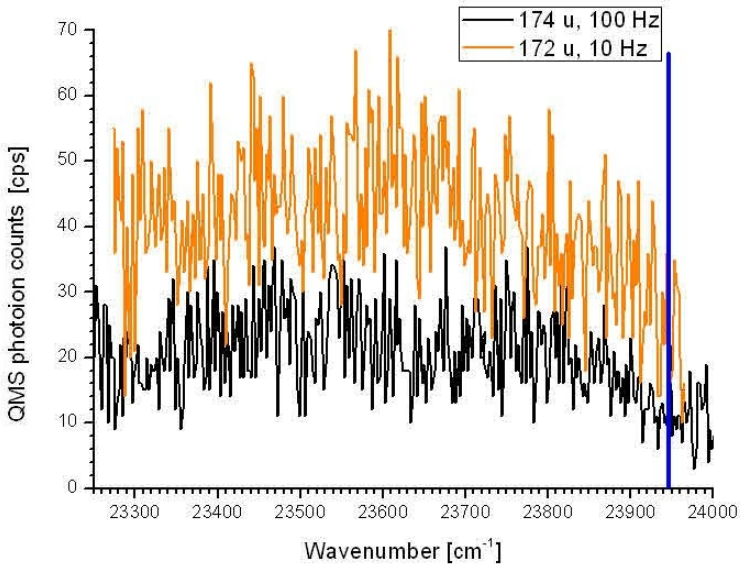

Figure 4.9: First Rb doped Droplet PI Spectrum - Dimers

Laser dye: Stilbene 3, 1.5 mJ max., XeCl laser: 10 Hz / 100 Hz, 60 mJ, QMS: 2.5 kV SEM voltage, 85 u, SR400: 0.5 s counting time, Rb source: 85 °C, signal not laser energy normalized, wavenumber measured with pulse wavemeter, ion yield optimized ion extraction region voltages, cold head on: 17 K, 50 bar, date: 18.11.2011, files: PI0073.txt, PI0074.txt.

The blue bar is marking the wavenumber at which the dimer mass spectrum in fig. 4.12 was recorded.

4.2.2 Laser Energy Normalization

The laser pulse energy was not constant over the scan range, as fig. 4.8 shows. At respective wavenumbers, a very intensive transition might look quiet inconspicuous because of low laser energy. To obtain a better feeling about what are the most intensive parts of the signal, a laser energy normalisation was done for most of the spectra.

Fig. 4.10 shows the normalized version of the signal plotted in fig. 4.8. At every wavenumber, the original signal was divided by the actual laser energy measured by means of the thermal detector head. That normalization is correct as long as one can assume linear dependence between laser intensity and ion yield. Yet for complex multi-step absorption processes, the probability of each step is proportional to the photon density. Consequentially, a two step PI yield scales with the squared laser intensity.

Anyway it is useful to stick to linear normalization.

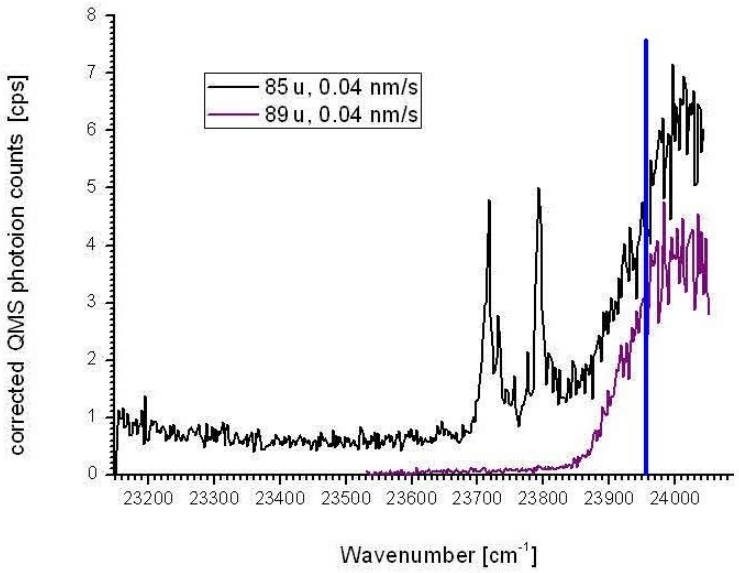

Figure 4.10: First Rb doped Droplet PI Spectrum - Laser Energy Normalisation

Laser dye: Stilbene 3, 1.5 mJ max., XeCl laser: 10 Hz, 60 mJ, QMS: 2.5 kV SEM voltage, 85 u, SR400: 0.5 s counting time, Rb source: 85 °C, signal laser energy normalized, wavenumber measured with pulse wavemeter, ion yield optimized ion extraction region voltages, cold head on: 17 K, 50 bar, date: 18.11.2011, files: PI0071.txt, PI0072.txt.

At maximum signal yield, it is interesting to perform mass scans. Again the blue bar in fig. 4.10 is marking the wavenumber, at which a mass spectrum was recorded. This spectrum is displayed in fig. 4.11 in the next subsection.

Fig. 4.8 and fig. 4.10 show only a small extract of a complete PI spectrum. That is no complete Rb investigation. Therefore, the laser dye needs to be changed in order to continue to neighbouring wavelength regions. But the purpose of these recordings was to find proper settings for subsequent Cr experiments. Fortunately, these two spectra are

showing similarities to an in-droplet Rb LIF spectrum recorded on the CLI apparatus. This LIF spectrum is found in [10]. Thus it was considered the settings are good enough to resolve interesting structures. So except mass scans, no more Rb investigations had been made. The following subsection continues with the mass spectra.

As mentioned in subsection 4.2.1, the broad structure within the spectrum shown in fig. 4.10 seems to consist of the in-droplet correspondence of the two effusive lines at $23715\,\mathrm{cm}^{-1}$ and $23792\,\mathrm{cm}^{-1}$. Within the droplet, these transition lines get blueshifted and broadened. Since the team from CLI already investigated such spectra, no more efforts had been made to explain the data in fig. 4.10 and also the mass spectra shown in fig. 4.11 and fig. 4.12.

4.2.3 Mass Spectrum

Compared to effusive beam investigations, the variety of fragments produced by in-droplet PI is much higher. There may be different isotopes of a certain metal. Each isotope can form an $RbHe_n^+$ with one or more He atoms. Clusters of several metal atoms with arbitrary isotopic mixture can be formed. These clusters can even form nonstabile molecules using He atoms. All these species can entirely be ionized and detected by the QMS. Some of them decay into fragments and increase ion counts of lower mass.

For Rb doped droplets, dimer formation can be detected by PI, as fig. 4.11 and 4.12 show. $RbHe_n^+$ formation can be induced by absorption of a photon and detected by subsequent PI.

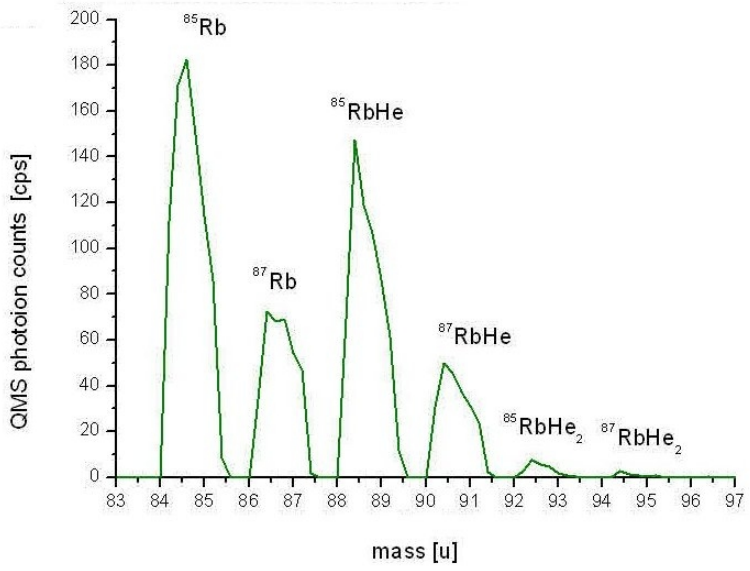

Figure 4.11: First Rb doped Droplet Mass Spectrum

Laser dye: Stilbene 3, 1.5 mJ max., 417.4 nm, XeCl laser: 10 Hz, 60 mJ, QMS: 2.5 kV SEM voltage, $\Delta = 0.2$ u, SR400: 200 ms counting time, Rb source: 90 °C, ion yield optimized ion extraction region voltages, cold head on: 17 K, 50 bar. date: 18.11.2011, files: QMS1343.txt.

The spectrum fig. 4.11 reflects the natural isotopic composition of Rb, namely 72 % ^{85}Rb and 28 % ^{87}Rb. The ion extraction region voltages had been set to the values optimized for the pickup of Rb listed in (Tab. 3.1). The `resolution´ parameter described in subsection 3.1.6 was also increased, the peak shapes are asymmetric. The ratio between monomer abundance and the abundances of the different $RbHe_n^+$ may be different at other exciting laser wavelengths.

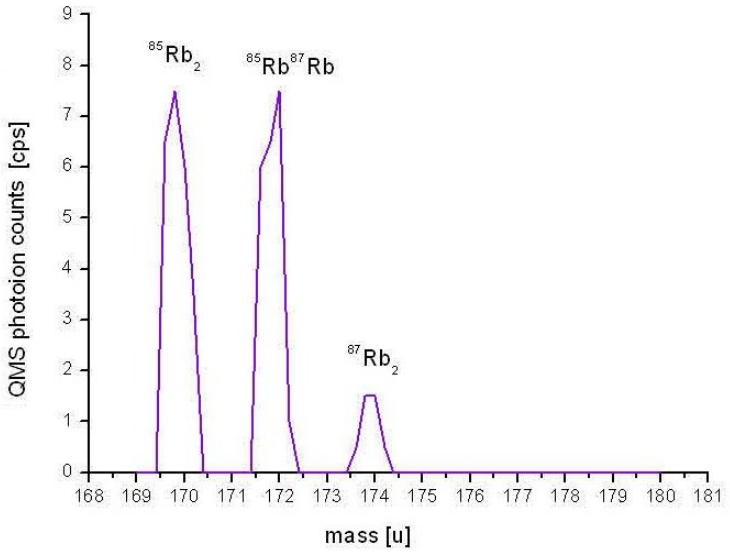

Figure 4.12: First Rb doped Droplet Mass Spectrum - Dimers

Laser dye: Stilbene 3, 1.5 mJ max., 417.4 nm, XeCl laser: 10 Hz, 60 mJ, QMS: 2.5 kV SEM voltage, $\Delta = 0.2$ u, SR400: 200 ms counting time, Rb source: 90 °C, ion yield optimized ion extraction region voltages, cold head on: 17 K, 50 bar. date: 18.11.2011, files: QMS1346.txt, PI0072.txt.

Also the dimer spectrum fig. 4.12 reproduces expectations very well. Peak height ratios fit to the binomial relations $0.72^2 = 0.52$, $2 \times 0.72 \times 0.38 = 0.40$ and $0.38^2 = 0.08$. This means a dimer composition of 52 % $^{85}Rb_2$, 40 % $^{85}Rb\,^{87}Rb$ and 8 % $^{87}Rb_2$.
Mass spectra are valuable for gaining information about which species are formed. Subsequently, after identification, the QMS can be set to respective masses for recording PI spectra of complex species. Thus one can learn a lot about structure and interaction.

4.2.4 Conclusion

Indeed a combination of sharp peaks and broadened in-droplet signal was observed. As expected, the $RbHe^+$ spectrum looked similar. Both signals are plotted in fig. 4.8. Fig. 4.9 shows a dimer PI spectrum having a low signal-to-noise ratio.

The Rb^+ and $RbHe^+$ PI spectrum had been laser energy normalized. The results are plotted in fig. 4.10. Mass scans fig. 4.11 and fig. 4.12 highlight the production of $RbHe_n^+$ up to an order n = 2 and dimer production in the expected isotopic ratio.

Now the final conclusion for Rb spectroscopy was that it works and delivers the ex-

pected results. There is still some potential for optimization, but it is not needed since the main goals are investigations of Cr. The following section continues with that.

4.3 Cr-doped Droplet Spectra using DMQ Laser Dye

As PI of Rb on droplets was successful, prerequisites for Cr doped droplet PI had mostly been done. The lowest ionization energy of Rb is $33690\,\mathrm{cm}^{-1}$. For Cr, it is much higher and ranges at $54570\,\mathrm{cm}^{-1}$. Two-photon-one-colour PI is only possible, if the photon energy of the laser is larger than half this value. We had to change from Stilbene 3 to some ultraviolet laser dye. DMQ solved in 1,4-Dioxane was found to be appropriate. For actual conditions, the tuning range of the dye was 350 to 370 nm or 27000 to $28600\,\mathrm{cm}^{-1}$. The maximum pulse energy is reached at 364 nm or $27500\,\mathrm{cm}^{-1}$. Unlike Stilbene 3, it has a high photochemical stability. There is no need to change the dye solution after one single measurement day.

The optimized PI procedure found during the last section was now used to record proper Cr PI spectra. During recordings in the following sections 4.3 and 4.4, the ion extraction region voltages optimized for Cr detection had been used. These voltages are outlined in (Tab. 3.1).

Fig. 4.13 shows a part of the energy level diagram of Cr. [12] is suggesting several PI schemes. Just like with Rb, two-photon-one-colour processes are possible, for example through the $y^7\mathrm{P}$ atomic levels. For DMQ, the laser energies overlap with the energy necessary to excite from the ground state to these levels.

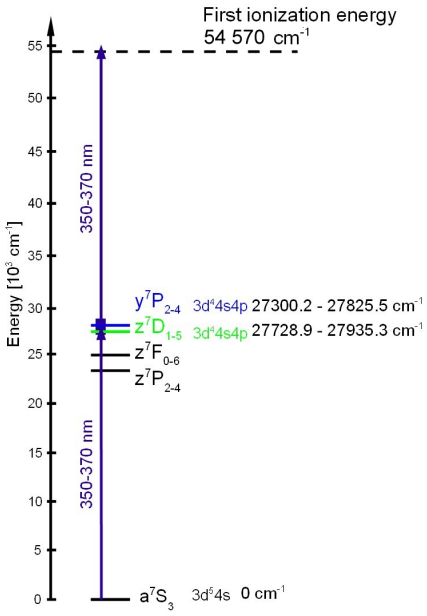

Figure 4.13: Bare Cr Atom Energy Level and Transition Scheme

Since it was the very first attempt of in-droplet PI of Cr, no publications existed yet. Fortunately papers [7] and [9] deal with related topics. [7] is about PI spectroscopy of Ag atoms in He nanodroplets, while [9] investigated Cr and Mo in solid noble gas matrices. Especially the absorption spectrum fig. 3 in [9] was a helpful guideline.

However, it was hard to make any predictions. For interpretation, a detailed table of Cr atomic levels was found to be useful, namely [13].

4.3.1 First Attempts

Pickup optimization described in subsection 3.1.3 was followed by the very first tests of PI of Cr atoms in superfluid He droplets. Indeed a signal appeared. A quick scan showed a continuous broad structure. Two noticeable sharp peaks could be resolved at 28199 cm^{-1} and 28422 cm^{-1}. This scan is plotted in fig. 4.14.

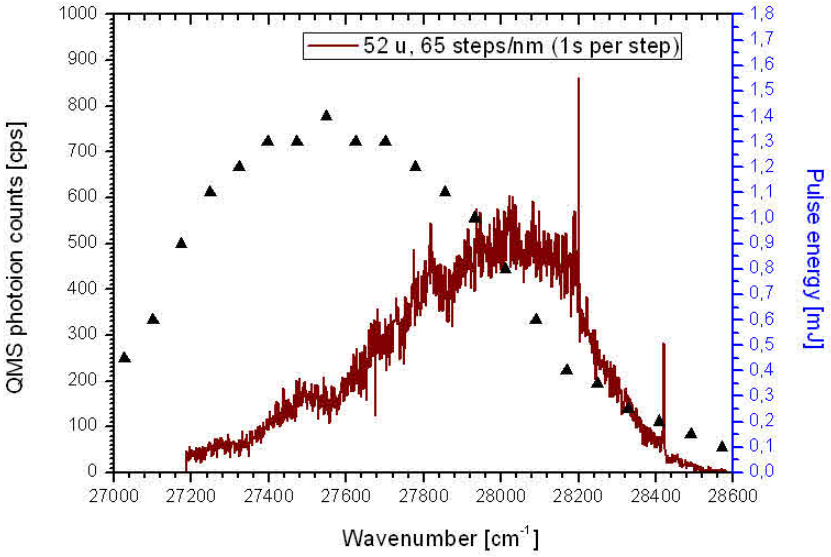

Figure 4.14: First Cr doped Droplet PI Spectrum and Laser Pulse Energy

Laser dye: DMQ, 1.5 mJ max., XeCl laser: 30 Hz, 60 mJ, QMS: 2.5 kV SEM voltage, 52 u, 145 W heating power, SR400: 1 s counting time, signal not laser energy normalized, wavenumber measured with monochromator, ion yield optimized ion extraction region voltages, cold head on: 15 K, 50 bar, date: 30.11.2011, files: PI0106.txt.

Unlike with the Rb in-droplet PI spectrum fig. 4.8, the appearance of sharp peaks is remarkable in this case. The following subsections 4.3.3 to 4.3.6 include interpretation. Subsection 4.3.5 includes interpretation of the broad structure.

The following plot fig. 4.15 gives a more detailed view of the sharp peaks in the spectrum. The related raw and FFT smoothed dye laser cross-section profile using DMQ laser dye is plotted in fig. 4.16.

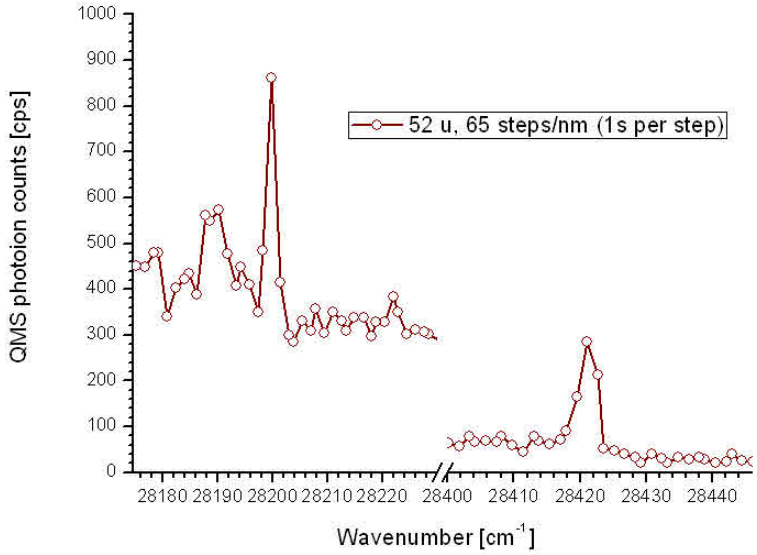

Figure 4.15: Cr-doped Droplet PI Spectrum - Detailed View of the Peaks

Laser dye: DMQ, 1.5 mJ max., XeCl laser: 30 Hz, 60 mJ, QMS: 2.5 kV SEM voltage, 52 u, 145 W heating power, SR400: 1 s counting time, signal not laser energy normalized, wavenumber measured with monochromator, ion yield optimized ion extraction region voltages, cold head on: 15 K, 50 bar, date: 30.11.2011, files: PI0106.txt.

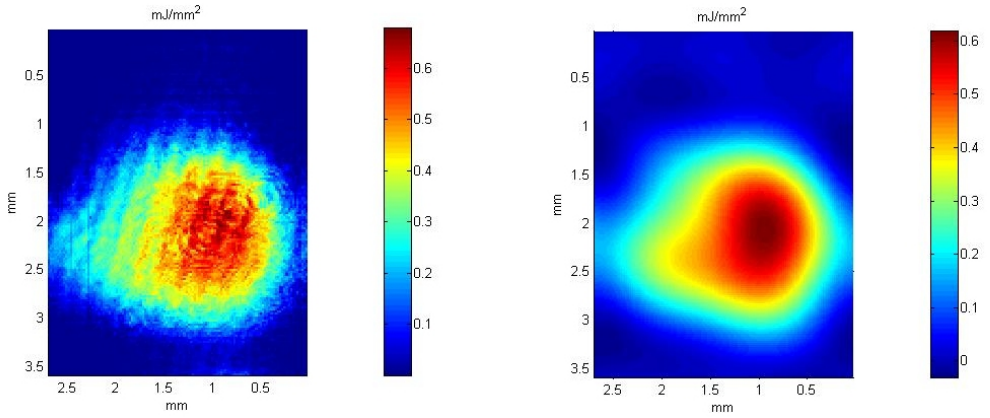

Figure 4.16: Raw and FFT smoothed Laser Profile

1.5 mJ pulse energy, 364 nm, date: 30.11.2011, files: Profile_DMQ_20111130.mat.

For this profile, the maximum pulse energy density was about 0.7 $\frac{\text{mJ}}{\text{mm}^2}$. To determine the maximum photon density, relations (3.1) - (3.3) from subsection 3.9.2, a laser wavelength of 364 nm and a pulse duration of 30 ns was used. The result was 1.3×10^{15} $\frac{\text{Photons}}{\text{mm}^2}$ total per pulse and 4.3×10^{22} $\frac{\text{Photons}}{\text{s mm}^2}$ during the pulse. The maximum short-time power density was 2.3×10^4 $\frac{\text{W}}{\text{mm}^2}$ and the total short time power was 5.0×10^4 W.

4.3.2 Laser Energy Normalization

Laser energy normalisation also seemed to be useful in this case. The normalized spectrum is displayed in fig. 4.17. It shows that the peak at 28422 cm^{-1} is much more prominent than the other one. The signal is relatively high at high energies. The structure may continue up to higher energies outside the wavenumber range of this spectrum. Thus in section 4.4 it was tried to expand the spectrum. This was done by changing to the laser dye having the next higher energy tuning range.

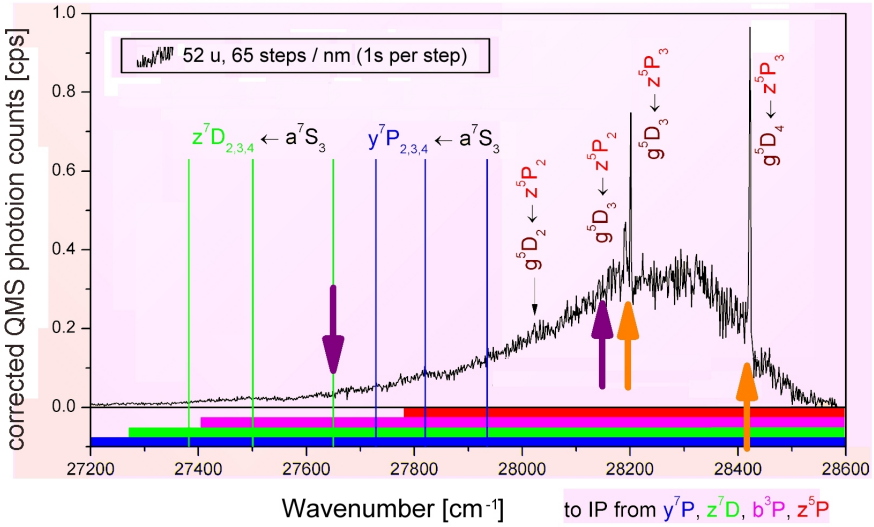

Figure 4.17: First Laser Energy normalized Cr doped Droplet PI Spectrum

Laser dye: DMQ, 1.5 mJ max., XeCl laser: 30 Hz, 60 mJ, QMS: 2.5 kV SEM voltage, 52 u, 145 W heating power, SR400: 1 s counting time, signal laser energy normalized, wavenumber measured with monochromator, ion yield optimized ion extraction region voltages, cold head on: 15 K, 50 bar, date: 30.11.2011, files: PI0106.txt.

Like with Rb in fig. 4.8, this spectrum is also a combination of sharp peaks and broadened structure. But with Cr, there was no effusive beam. Thus the appearance of sharp transition lines is remarkable and will be discussed in the following subsections 4.3.3 to 4.3.4. The mean droplet size was 10000 atoms. The coloured rows below the spectrum indicate energy thresholds. At every threshold, the photon energy becomes high enough for PI from certain levels. Related descriptions are found in subsection

4.3.5. Purple coloured arrows mark the laser wavelengths, at which the two mass scans shown in fig. 4.23 had been recorded. The orange bars correspond to mass scans shown in fig. 4.24. Also the positions of certain bare Cr transitions are marked and signed in this plot.

4.3.3 Bare Cr - Excitation and Ejection

Based on transition rules (2.28) outlined in section 2.5, papers [9], [12] and tables like [13], a level scheme for two-photon-one-colour PI of Cr was created. It is shown in fig. 4.18. In order to interpret experimental data and link it to such a scheme, knowledge about the basic concepts of many electron atoms is necessary. An outline about this topic is found in section 2.3.

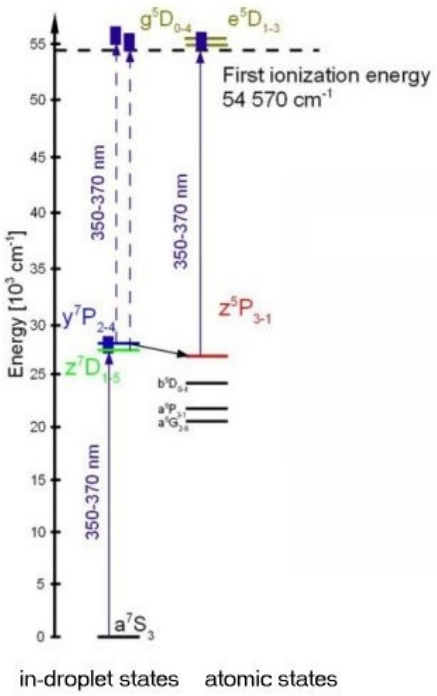

Figure 4.18: Cr - Excitation and Ionization Scheme

As discussed in subsection 4.3.1, the sharp peaks in fig. 4.14 are remarkable. They fit exactly to atomic transitions $z^5P_3 \rightarrow g^5D_3$ at 28199 cm^{-1}, and $z^5P_3 \rightarrow g^5D_4$ at 28422 cm^{-1}.

This proves the presence of bare and excited Cr atoms in the z^5P levels.

Since there is no beam of effusive Cr, it can be concluded that a fraction of Cr atoms leaves the droplet. z^5P levels are located around 27000 cm^{-1} above the a^7S_3 ground state. This shows that ejection out of the droplet happens after excitation. The atoms

change from in-droplet ground state to some in-droplet excited level and subsequently to atomic z^5P. Also other transitions and even relaxation to the ground state during ejection are imaginable. Further information is found in subsection 4.3.6.

In the paper [7], the in-droplet D1 transition of Ag is also followed by ejection from the droplet. It goes into bare Ag $^2P_{1/2}$, $^2P_{3/2}$ and $^2D_{5/2}$ states.

Ejecting the Cr atom from in-droplet y^7P to bare atom z^5P violates change of parity. Change of parity is dictated by the electric dipole transition rules (2.28) outlined in section 2.5. Such a violation is enabled by an interaction with the helium, for example collisions, as described in section 2.7.

It is easy to detect ejection of Cr atoms. Ejection may be followed by two different PI processes. Direct PI, possible at continuous energies, and much more efficient autoionization, only at discrete energies[1]. Both processes are described in the following subsections 4.3.4 and 4.3.5.

4.3.4 Autoionization

From atomic z^5P one can excite to discrete levels above the first ionization energy at $54570\,\mathrm{cm}^{-1}$, for example g^5D. The wavenumbers can tell from which sublevels of z^5P the atoms origin, and into which sublevels of g^5D they are excited. From these levels, autoionization is possible. A description of the theoretical concepts of autoionization is found in subsection 2.6.2 and [4].

Fig. 4.19 shows the electron configuration of the states related to the orbital model autoionization scheme. For g^5D, the 5s orbital is populated by one electron. It is most likely that following autoionization, the emitted electron originates from this orbital.

[1] There is yet another imaginable process. In-droplet Cr might by ionized after excitation without ejection. This process is marked by dashed lines in fig. 4.18. Using the QMS, it is not possible to detect $CrHe_n^+$ if n is greater than 40. Thus an upcoming task will be to install the Cr source at CLI apparatus to make use of a time-of-flight mass spectrometer to handle larger masses.

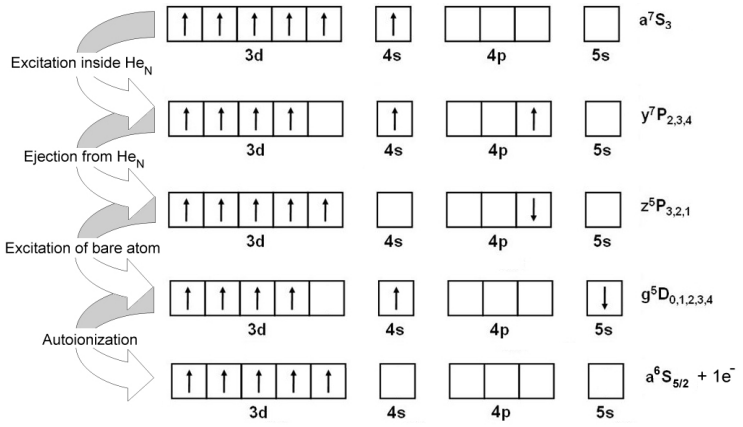

Figure 4.19: Prominent Excitation and Autoionization Scheme of Cr

What can be learned from the laser energy normalized autoionization peaks in fig. 4.17?

At the wavenumber of a peak, the compound process consisting of in-droplet excitation, ejection, atomic excitation to some autoionizing level and subsequent decay into the ionized state occurs. Since the peaks arise conspicuously from the background signal, it shows that autoionization is much more efficient than direct ionization. As long as saturation is avoided, the peak heights are depending on a combination of all the intermediate process probabilities. The peaks can be fitted to Fano profile functions to most accurately determine their height and thus the excitation yield. The excitation is a dipole transition. It is governed by Fermis Golden Rule, as already outlined in section 2.5.

Instead of using the Fermi Rule to calculate transition rates, it is easier to look for tabulated rates. Such can be found in [12]. Yet there are two more things to consider. The laser intensity is affecting the rates. Beside the laser energy, it is important to keep in mind the m_J-degeneracy of all the J-sublevels of z^5P and the autoionizing levels. Thus the transition rates have to be multiplied by factors respecting the diversity. The following table (Tab. 4.2) shows the transition diversity from z^5P to autoionizing states due to that m_J degeneracy.

Table 4.2: Number of allowed m_J Transitions between J Sublevels

		g^5D					e^3D		
	J	0	1	2	3	4	1	2	3
	3			35	49	63		35	49
z^5P	2		15	25	35		15	25	35
	1	3	9	15			9	15	

When comparing calculated transition rates and fitted peak heights, there might be some discrepancy due to non-equal population of the z^5P sublevels. Figuring out the population may give information about transitions to the lowest energy J-sublevel and also about the ejection process. By combining significant data and theoretical calculations, it might be possible to gain a better understanding about what really happens within the droplets. Unfortunately these calculations are complicated.

The PI spectrum fig. 4.18 includes only two peaks. Yet there are other possible transitions from z^5P to autoionizing levels at respective wavenumbers. Thus no conclusions about the z^5P sublevel population could be made. This topics latest results including advanced Cr PI spectra resolving some more lines can be found in section 4.5 and [5].

4.3.5 Continuous Structure

The autoionization mechanism describes the sharp peaks in fig. 4.14. What is now the reason for in-droplet PI spectra to show a continuous signal structure?

At first the in-droplet states are broadened. The mechanism of broadening is described in section 2.7. Secondly, direct PI is possible at continuous wavenumbers above the respective threshold. The total process consisting of in-droplet excitation, ejection and PI of the bare atom requires two photons. Thus the probability of the process is the product of the probabilities of the three steps.

The continuous structure of the spectrum shown in fig. 4.14 arises from in-droplet excitation, subsequent ejection followed by direct PI, as outlined in the scheme of fig. 4.20.

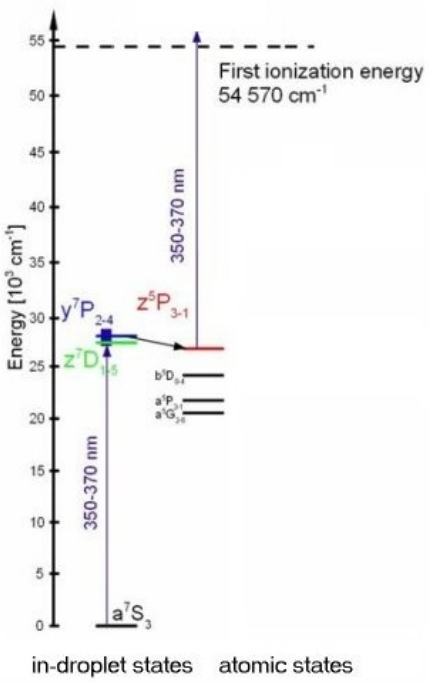

Figure 4.20: Cr - Excitation and Ionization Scheme

At a certain laser wavelength, two requirements have to be fulfilled to enable this process. First of all the laser energy needs to be higher than the difference of level energy and first ionization energy. The coloured rows at the bottom of fig. 4.17 mark the respective thresholds for different intermediate levels. The second thing is that a signal can only appear, if there is some in-droplet state the laser can excite to from the in-droplet ground state.

If the first requirement is fulfilled, the PI signal mainly depends on the in-droplet excitation yield. Thus the significant bump in fig. 4.18 at high laser energy is suspected to represent broadened in-droplet levels such as y^7P. The broadening ranges over $800\,cm^{-1}$. In paper [1], an excitation spectrum of Ag atoms at comparable wavelengths is found. Therein broadened peaks could be assigned to bare Ag states. Their in-droplet broadening is also in the range of 500 to $1000\,cm^{-1}$.

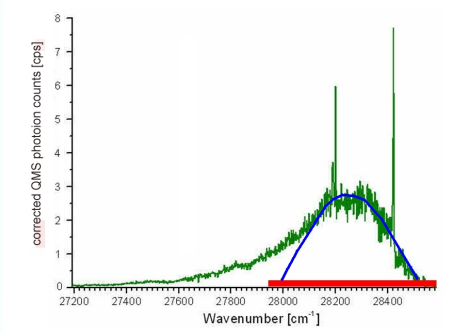

Figure 4.21: First Laser Energy normalized Cr doped Droplet PI Spectrum

Laser dye: DMQ, 1.5 mJ max., XeCl laser: 30 Hz, 60 mJ, QMS: 2.5 kV SEM voltage, 52 u, 145 W heating power, SR400: 1 s counting time, signal laser energy normalized, wavenumber measured with monochromator, ion yield optimized ion extraction region voltages, cold head on: 15 K, 50 bar, date: 30.11.2011, files: PI0106.txt.

In subsection 2.6.1, the Born approximation was introduced to describe direct PI. For the PI spectrum, this model predicts an absorption edge structure. Edges should be located at wavenumbers just high enough to reach the ionization potential from the z^5P sublevels. That threshold is marked by a red bar in fig. 4.21. The blue curve is a showcase of the y^7P in-droplet profile.

Yet this spectrum does not show any absorption edges. The reason might be that at the threshold, the y^7P excitation yield is low. However, the ion yield is relatively high at the threshold and below. That could be due to the high laser pulse energy in this region, as shown in fig. 4.14. A high pulse energy can enable more complicated processes, for example two-photon direct PI from an excited level. Thereby the doubled photon energy is much higher than the difference of ionization threshold and z^5P sublevel energies. Thus it is far away from absorption edges.

This speculation is supported by the finding, that the latest results outlined in section 4.5 had been achieved under a 20 times lower laser pulse energy. In spectrum fig. 4.28, the ion yield is nearly zero at wavelengths on the left hand side of the threshold marked in fig. 4.21.

All in all it is hard to describe this broad signal structure. It could be an overlay of several broadened peaks. Theoretical calculations could help in understanding this broad structure.

4.3.6 Population of Atomic States

The sharp peaks and the continuous structure in fig. 4.17 had been described in the last two subsections. Yet the fact that Cr atoms are ejected gives rise to another question. Is

there some population of other atomic states, as in [9]? From the excited droplet state, there might be ejection to some other state or even transition from z^5P. Also relaxation to the ground state seems possible. The simplest processes are the most likely. Fig. 4.22 is outlining possible transitions.

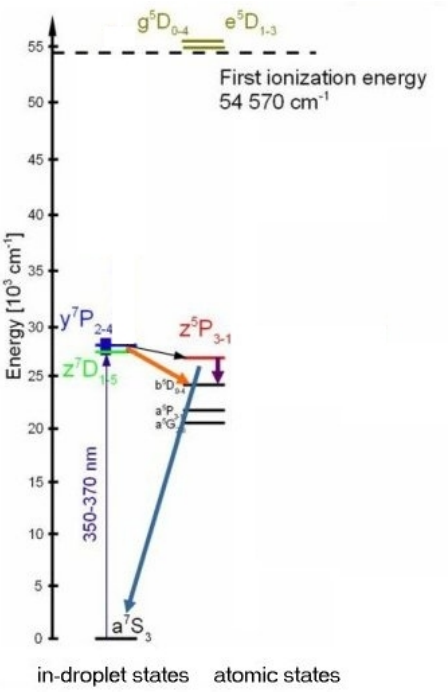

Figure 4.22: Cr - Transition Scheme

Auto- and direct ionization produce ions. Thus the QMS can be used to observe these two effects. Yet for atomic transitions, there needs to be some other detection method. LIF could be a key to that. After laser pulse induced ejection and transition, relaxation to the ground state causes emission of fluorescence light. As described in section 3.1, the CLII apparatus is equipped with facilities to detect fluorescence light. Fluorescence light is emitted for only a few 10 ns after the pulse. Thus it is recommended to use the SR400 gated counting mode for respective PM pulses. The gated counting mode is described in section 3.2.

4.3.7 Mass Scans

Beside PI recordings, it was insightful to make use of the QMS mass scan function. The laser was subsequently set to four different wavelengths to detect ions. The positions of these wavelengths are marked by arrows in the spectrum fig. 4.17. Results are shown in fig. 4.23 and fig. 4.24. These plots are showing the interesting sections of complete mass scans.

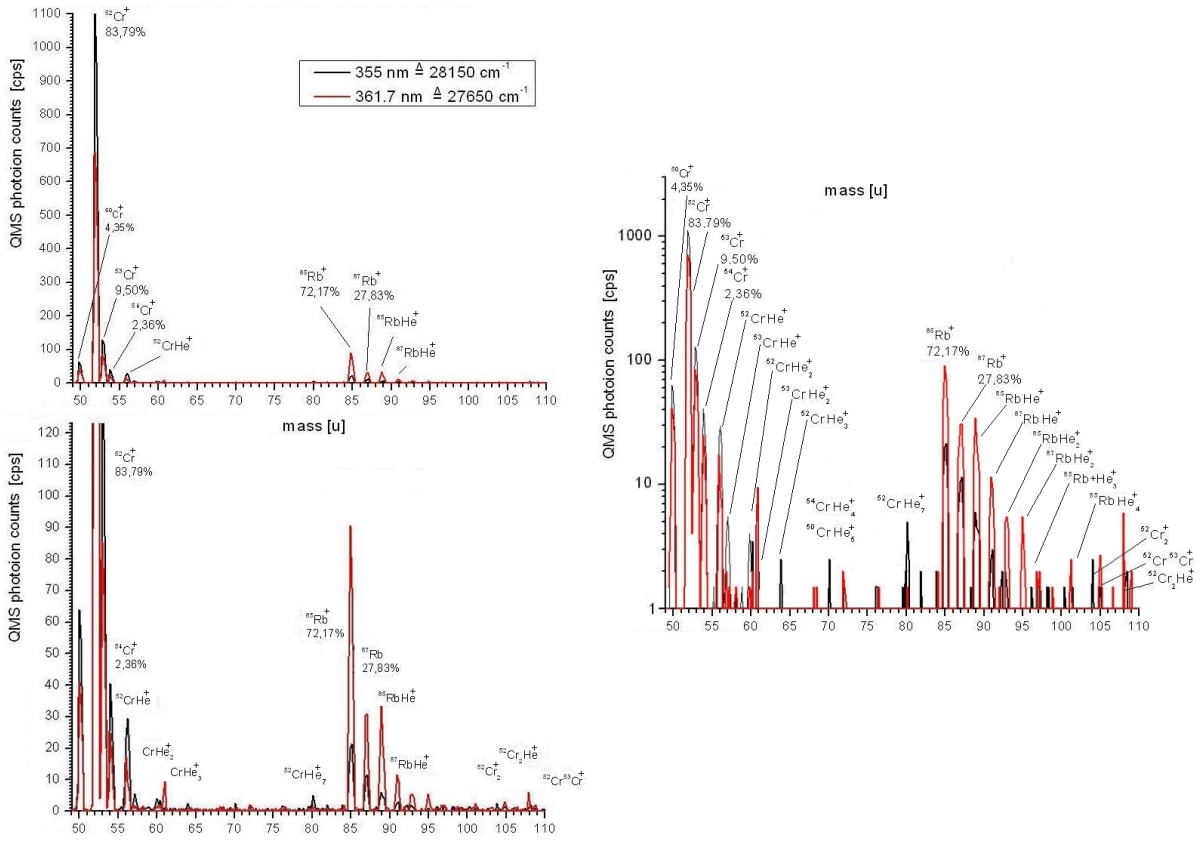

Figure 4.23: First Cr and Rb doped Droplet Mass Spectrum

Laser dye: DMQ, 1.3 mJ max., XeCl laser: 30 Hz, 60 mJ, QMS: 2.5 kV SEM voltage, 145 W heating power, $\Delta = 0.2$ u, SR400: 200 ms counting time, ion yield optimized ion extraction region voltages, cold head on: 15 K, 50 bar. date: 23.11.2011, files: QMS1352.txt to QMS1366.txt.

In fig. 4.23, the four Cr isotopes are present in the expected isotopic ratio outlined in section 2.2. These two mass scans had been recorded at two different laser wavelengths. The wavelengths are located offside the peaks of the continuous structure in fig. 4.17. Formation of $CrHe_n^+$ and dimerisation is observed. For $CrHe_n^+$, the isotopic ratio holds up to n = 2. $CrHe_n^+$ of higher n are sporadic, amounts are too for classification. Relatively high amounts of $CrHe_7^+$ are detected. It looks like seven He atoms is some magic number, so that $CrHe_n^+$ is very stabile at n = 7. The Rb source was still installed, Rb is also present. Although the Rb source had been cooled to minimize Rb pickup. Cooling was done via thermal connection to a vessel filled with liquid nitrogen. Also pure and mixed isotopic dimers and even $Cr_2He_n^+$ are observed sporadically.

$Cr_nHe_m^+$ can be formed in two ways. The first possibility is that an in-droplet Cr atom or cluster gets excited. In the excited state, it can combine with He atoms to form an

excited molecule, a so-called exciplex, that may not be stable in the groundstate. The exciplex might be ejected or stays within the droplet. Via PI, only ejected exciplexes can be detected by the QMS. The reason is outlined in the footnote in subsection 4.3.3.

Otherwise the $Cr_nHe_m^+$ can be formed after ionization of ejected Cr_n. The Cr_n^+ might catch surrounding He atoms. It is not possible to distinguish between these species and exciplexes.

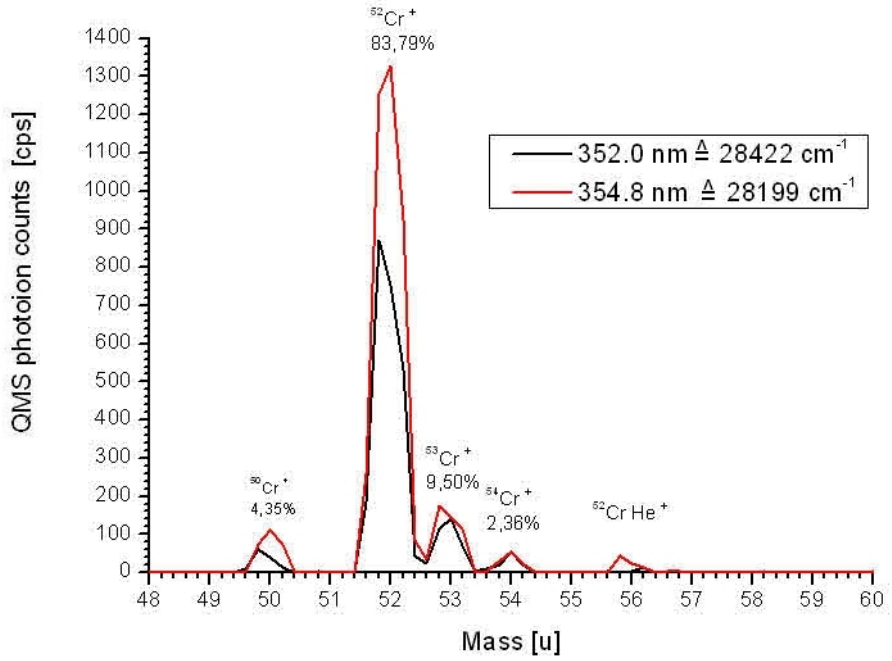

Figure 4.24: First Cr doped Droplet Mass Spectrum at Peak Wavelength

Laser dye: DMQ, 1.0 mJ max., XeCl laser: 30 Hz, 60 mJ, QMS: 2.5 kV SEM voltage, 145 W heating power, $\Delta = 0.2$ u, SR400: 200 ms counting time, ion yield optimized ion extraction region voltages, cold head on: 19 K, 50 bar. date: 30.11.2011, files: QMS1394.txt, QMS1396.txt.

The two scans in fig. 4.24 had been recorded at the wavelengths of the two peaks in fig. 4.17. Formation of Cr_nHe_m seems to be suppressed. The autoionizing mechanism is dominant at the peak wavelengths. It might be that Cr atoms or clusters do not combine with He atoms in the autoionization state.

4.3.8 Conclusion

The pickup conditions had been optimized to favour droplets doped with one single Cr atom each. A PI spectrum was recorded showing two remarkable sharp peaks plotted in fig. 4.14, while fig. 4.15 is giving a more detailed view of the peaks. Using the Cr level diagram [13] and accounting for the dipole transition rules, these lines could clearly be interpreted as transitions from z^5P bare atomic sublevels to g^5D autoionizing sublevels. g^5D levels are situated above the first ionization threshold.

It can thus be concluded that Cr atoms are ejected from the droplets after excitation. Subsequently, they are directly ionized; or excited to the autoionizing levels from which they decay into ions. The related scheme is shown in fig. 4.19. Beside z^5P, other bare atomic states may be populated. The PI spectrum was also laser energy normalized, as shown in fig. 4.17. The normalized heights of the sharp peaks are related to the transition rates between z^5P and the autoionizing levels. Thus the heights are also related to the population of z^5P sublevels times the degeneracy. (Tab. 4.2) is giving the number of allowed transitions with respect to m_J degeneracy.

Since in-droplet states are broadened and direct ionization goes into a continuum of states, there are ionization pathways at continuous wavenumbers. That is the reason for broad structures in the spectra fig. 4.14 and fig. 4.17.

PI mass scans had been performed at four different wavelengths, two of them at the wavelengths of the two peaks. Results are plotted in fig. 4.23 and fig. 4.24. $CrHe_n^+$ are produced up to an order $n = 7$. Pure and mixed isotopic dimers and $Cr_2He_n^+$ are produced.

4.4 Cr-doped Droplet Spectra using PTP Laser Dye

After interpreting results of Cr PI using DMQ laser dye, it was interesting to look for similar effects at next higher laser energy. A dye called PTP solved in 1,4-Dioxane was found to be suitable for this purpose. For actual conditions, the tuning range of the dye was 336 to 347 nm, or 28800 to 29700 cm^{-1}. The maximum pulse energy is reached at 342 nm or 29200 cm^{-1}. The dye solution was filled into the circulators and the laser got readjusted with respect to low ASE. Other settings remained the same.

Fig. 4.13 shows the energy level diagram of Cr. Also within the tuning range of PTP, there are bare atomic transitions $a^7S_3 \rightarrow y^5P_2$ at 29584 cm^{-1}. Thus one could expect similar results and maybe also sharp peaks.

It turned out that the signal is relatively low compared to PI measurements using DMQ. Therefore three scan repetitions were made, one of them at a higher scan rate. Fig. 4.25 shows a plot of the highest scan rate PI signal. No significant spectral structure arose;

in principal the signal represents the pulse energy distribution of the laser.

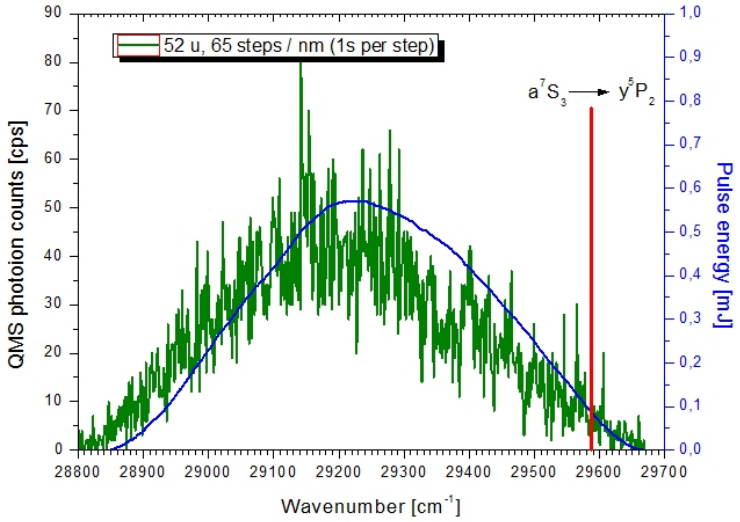

Figure 4.25: Cr doped Droplet PI Spectrum and Laser Pulse Energy

Laser dye: PTP, 0.6 mJ max., XeCl laser: 30 Hz, 60 mJ, QMS: 2.5 kV SEM voltage, 52 u, 150 W heating power, SR400: 1 s counting time, signal not laser energy normalized, wavenumber measured with monochromator, ion yield optimized ion extraction region voltages, cold head on: 19 K, 50 bar, date: 12.12.2011, files: PI0124.txt.

Since the signal to noise ratio was bad, it might be that small spectral structures are hidden by the noise. Hence the signal was smoothed by means of a 29 points Savitzky-Golay algorithm. The smoothed spectrum fig. 4.26 shows peak-like but not very significant structures. It includes the smoothed correspondence of the curve plotted in fig. 4.25 and the two other curves at a scan rate of 30 steps/nm.

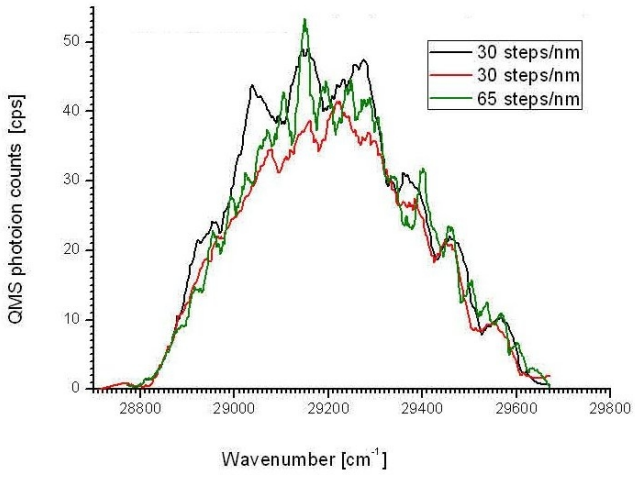

Figure 4.26: Smoothed Cr doped Droplet PI Spectrum

Laser dye: PTP, 0.6 mJ max., XeCl laser: 30 Hz, 60 mJ, QMS: 2.5 kV SEM voltage, 52 u, 150 W heating power, SR400: 1 s counting time, signal not laser energy normalized, wavenumber measured with monochromator, ion yield optimized ion extraction region voltages, cold head on: 19 K, 50 bar, date: 12.12.2011, files: PI0120.txt, PI0121.txt, PI0124.txt.

For Stilbene 3 and DMQ, laser cross section profiles are shown in fig. 4.5 and fig. 4.16 within subsections 4.1.2 and 4.3.1. The spot sizes are nearly the same. For PTP, no laser cross section profile was recorded. But it can be approximated by these two others, although it scales with a lower total pulse energy.

Fig. 4.27 shows the laser energy normalized and smoothed data. The ion yield slightly falls while scanning the laser up to the high energy limit of the tuning range. The peaks at the signal boundaries are due to division by a laser energy value of nearly zero.

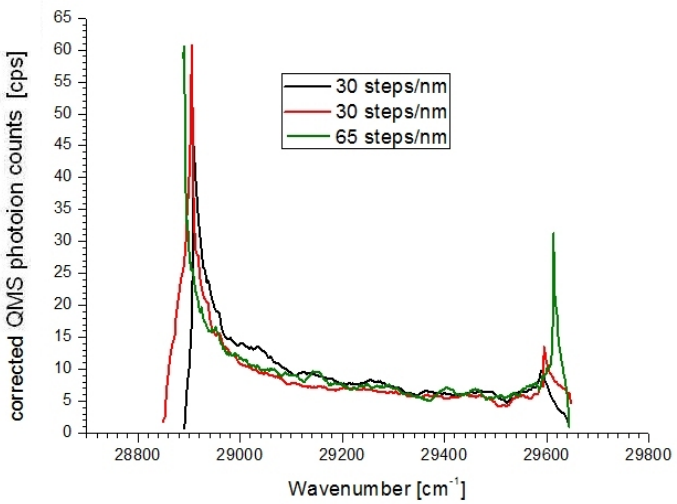

Figure 4.27: Smoothed and Laser Energy normalized Cr doped Droplet PI Spectrum

Laser dye: PTP, 0.6 mJ max., XeCl laser: 30 Hz, 60 mJ, QMS: 2.5 kV SEM voltage, 52 u, 150 W heating power, SR400: 1 s counting time, signal laser energy normalized, wavenumber measured with monochromator, ion yield optimized ion extraction region voltages, cold head on: 19 K, 50 bar, date: 12.12.2011, files: PI0120.txt, PI0121.txt, PI0124.txt.

In both fig. 4.26 and fig. 4.27, no significant spectral structure arises, even at 29584 cm^{-1}. Thus for later investigations, we returned to DMQ and RDC360Neu laser dye. RDC360Neu has about the same tuning range as DMQ. Latest results are outlined in the following section.

4.5 Latest Results

This thesis includes the very first results of PI spectroscopy on Cr-doped droplets. Later results had been more mature due to improved measurement procedures. Fig. 4.28 shows an advanced spectrum. In fig. 4.17, only transitions from z^5P to g^5D autoionizing levels could be resolved. Now transitions to both g^5D and e^3D had been observed. Fig. 4.29 is giving a more detailed view of the peak structured regions within the spectrum.

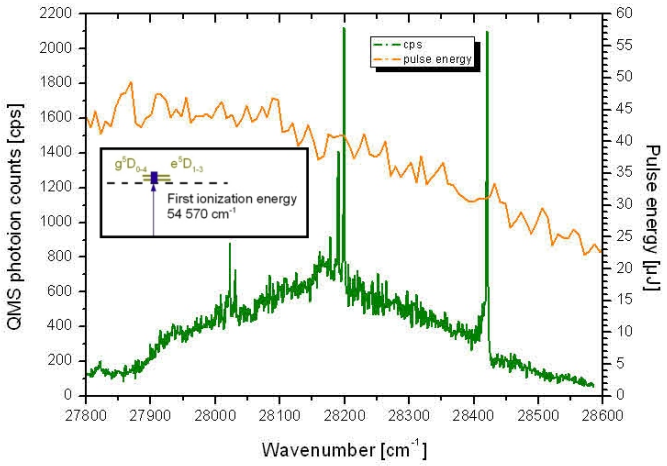

Figure 4.28: Cr doped Droplet PI Spectrum and Laser Pulse Energy

Laser dye: RDC360Neu, 50 μJ max., XeCl laser: 100 Hz, 100 mJ, QMS: 2.5 kV SEM voltage, 52 u, 170 W heating power, SR400: 1 s counting time, signal laser energy normalized, wavelength controlled by PC: 100 steps/nm, ion yield optimized ion extraction region voltages, cold head on: 20 K, 50 bar, date: 25.02.2012, files: PI0238.txt.

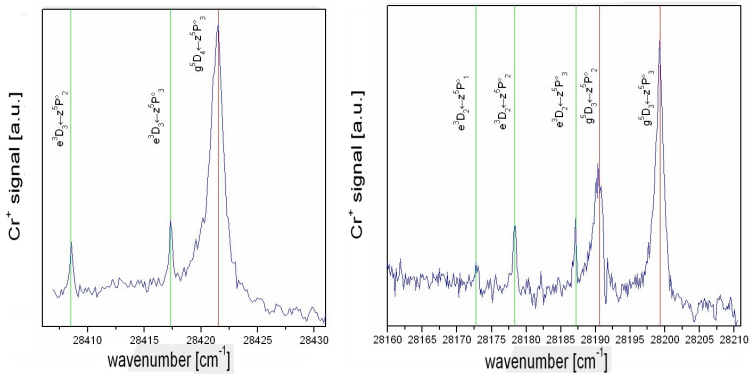

Figure 4.29: Cr doped Droplet PI Spectrum

Laser dye: RDC360Neu, 50 μJ max., XeCl laser: 100 Hz, 100 mJ, QMS: 2.5 kV SEM voltage, 52 u, 170 W heating power, SR400: 1 s counting time, signal laser energy normalized, wavelength controlled by PC: 500 steps/nm, ion yield optimized ion extraction region voltages, cold head on: 20 K, 50 bar, date: 25.02.2012, files: PI0241.txt, PI0242.txt.

Concerning measurement conditions, it is remarkable that the laser pulse energy was about 20 times lower than for measurements in section 4.3. The main amplifier pump pulse was attenuated. The reason for that was to avoid saturation. Saturation may have played a role during former measurements, although there had been efforts to avoid it, as described in subsection 3.4.4. The related raw and FFT smoothed dye laser cross-section profile using RDC360Neu laser dye is plotted in fig. 4.30. It is now scaled in μJ.

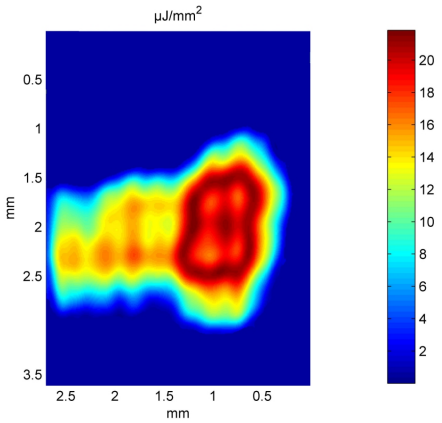

Figure 4.30: Raw and FFT smoothed Laser Profile

50 μJ pulse energy, 355 nm, date: 25.02.2012, files: Profile_RDC360Neu_20120225.mat.

For this profile, the maximum pulse energy density was about 22 $\frac{\text{mJ}}{\text{mm}^2}$. To determine the maximum photon density, relations (3.1) - (3.3) from subsection 3.9.2, a laser wavelength of 355 nm and a pulse duration of 30 ns was used. The result was 3.9×10^{13} $\frac{\text{Photons}}{\text{mm}^2}$ total per pulse and 1.3×10^{21} $\frac{\text{Photons}}{\text{s mm}^2}$ during the pulse. The maximum short-time power density is 730 $\frac{\text{W}}{\text{mm}^2}$ and the total short time power was 1700 W.

More sophisticated results of PI spectroscopy on Cr including interpretation are found in [5] and will be found in [19].

5 Conclusion and Outlook

In course of this master thesis, the very first two-photon-one-colour PI on single Cr atoms in superfluid helium nanodroplets was realized. Following results had been achieved:

- Appropriate experimental conditions had been found. Measurement devices had been configured and combined in a suitable way. Controlling- and evaluation routines had been developed. See the appendix and chapter 3.
- A way of how to adjust the dye laser in the demanded wavelength region was found. With this adjustment, the pulse energy became sufficiently narrow and the spectral profile sufficiently small. Especially elimination of ASE improved the performance. See section 3.4.5.
- The QMS extraction voltages had been optimized to increase the ion yield of interesting species Rb^+ and Cr^+. See section 3.1.6.
- Bare Rb transitions had been investigated using PI. It was found that the broadening of transition lines is due to the lasting spectral broadness of the laser light. This broadening was determined to be gaussian by means of a curve fit. The standard derivation is $0.4\,\mathrm{cm}^{-1}$. The agreement of the line centers and tabulated Rb lines is limited by the accuracy of the wavemeter. See section 4.1 and subsection 4.1.3.
- Rb^+, $RbHe_n^+$ and Rb_2^+ had been produced by PI and detected by means of mass spectrometry up to n = 2. PI spectra of these species had been recorded. Beside the bare Rb transitions at $23715.4\,\mathrm{cm}^{-1}$ and $23792.9\,\mathrm{cm}^{-1}$ mentioned above, the Rb^+ spectrum shows the corresponding in-droplet lines. They are also shown in the $RbHe^+$ spectrum. They are broadened and blue-shifted. See section 4.2.
- Cr^+, $CrHe_n^+$ and $Cr_2He_m^+$ had been produced by PI and detected by means of mass spectrometry up to n = 7 and m = 1. Cr^+ PI spectra had been recorded in the wavelength range of the two laser dyes DMQ and PTP. In the PTP region, signal and signal-to-noise ratio had been low. In the DMQ region, a continuous structure combined with two sharp peaks at $28199\,\mathrm{cm}^{-1}$ and $28422\,\mathrm{cm}^{-1}$ was recorded. See section 4.3.
- These two peaks could be identified as bare Cr transitions from z^5P to g^5D sublevels. Thus it was concluded that Cr atoms are ejected from the droplets into the z^5P state after in-droplet excitation. From z^5P, the Cr atoms are excited to autoionization levels g^5D, from where they undergo transitions into ionized states. See subsections 4.3.3 and 4.3.4.

- It was found that the continuous structure in the PI spectrum comes from the detection of directly-ionized ejected Cr atoms. See subsection 4.3.5.

Latest Cr PI spectra are not in course of this master thesis, yet documented in section 4.5 and in the paper [5]. Beside autoionization resonances mentioned above, these spectra show further peaks that can be assigned to transitions from z^5P to e^3D sublevels, which also decay into ions. The continuous structure seems to be due to the broadening and blue-shift of the a^7S to y^7P in-droplet Cr-excitations.

First tests of a two-step-two-colour PI on Cr-doped droplets had been successful. The dye laser was combined with a part of the excimer pump beam. Excitation was performed by the dye laser, while the excimer beam ionized the fragments. An interesting future task will be combining PI of Cr with TOF analysis, for example at CLI. Thereby, ionized fragments of higher masses like entirely ionized droplets can be detected. Furthermore, PI on Cu-doped droplets will be an interesting topic. Yet this will be preceded by other hot-topics like LIF- and Depletion-measurements on Cr-doped droplets. Therefore a new LIF transmission was assembled. The QMS was mounted off-axis. Due to the high magnetic moment, ESR-investigations of Cr will also be an interesting and challenging topic. Information will be found in [19].

6 Bibliography

6.1 Papers

[1] Bartelt, A.; Close, J. D.; Federmann, F.; Quaas, N.; Toennies, J. P.:
Cold Metal Clusters: helium droplets as a Nanoscale Cryostat, Physical Review Letters, American Physical Society, 1996, 77, 3525-3528

[2] Cheng, H., Wang, L.-S..:
Dimer Growth, Structural Transition, and Antiferromagnetic Ordering of Small Chromium Clusters, Phys. Rev. Letters, American Physical Society, 1996, 77, 51-54

[3] Callegari, C.; Ernst, W.:
Helium Droplets as Nanocryostats for Molecular Spectroscopy - from the Vacuum Ultraviolet to the Microwave Regime, Handbook of High-Resolution Spectroscopy. (2011), S. 1551 - 1594

[4] Fano, U.:
Effects of Configuration Interaction on Intensities and Phase Shifts, Phys. Rev., American Physical Society, 1961, 124, 1866-1878

[5] Kautsch, A.; Hasewend, M.; Koch, M.; Ernst, W.E.:
Fano resonances in chromium photoionization spectra after photoinduced ejection from a superfluid helium nanodroplets, submitted 2012

[6] Koch, M.; Lanzersdorfer, J.; Callegari, C.; Muenter, J.S.; Ernst, W.E.;
Molecular Beam Magnetic Resonance in Doped Helium Nanodroplets. A Setup for Optically Detected ESR/NMR in the Presence of Unresolved Zeeman Splittings, Journal of Physical Chemistry A, Amer Chemical Soc, 2009, 113, 1334713356

[7] Loginov, E.; Drabbels, M.:
Excited state dynamics of Ag atoms in helium Nanodroplets, Journal of Physical Chemistry A, Amer Chemical Soc, 2007, 111, 7504-7515

[8] Moroshkin, P.; Hofer, A., Weis, A.:
Atomic and molecular defects in solid ^{4}He, Physics Reports - Review Section Of Physics Letters, Elsevier Science Bv, 2008, 469, 1-57

[9] Pellin, M. J.; Gruen, D. M.; Fisher, T., Foosnaes, T.:
Emission, optical-optical double resonance, and excited state absorption spectroscopy of matrix isolated chromium and molybdenum atoms, The Journal of Chemical Physics, AIP, 1983, 79, 5871-5886

[10] Pifrader, A.; Allard, O.; Aubock, G.; Callegari, C.; Ernst, W. E.; Huber, R., Ancilotto, F.:
One- and two-photon spectroscopy of highly excited states of alkali-metal atoms on helium nanodroplets, Journal of Chemical Physics, Amer Inst Physics, 2010, 133, 164502

[11] Ratschek, M.; Koch, M.; Ernst, W.:
Doping helium nanodroplets with high temperature metals: Formation of chromium clusters, The Journal of Chemical Physics 136 (2012) , S. 104201-1 - 104201-6

[12] Saloman, E.B.:
A Resonance ionization Spectroscopy / Resonance ionization Mass Spectrometry data service. IIData sheets for Al, Ca, Cs, Cr, Co, Cu, Kr, Mg, Hg and Ni, Spectrochimica Acta Part B: Atomic Spectroscopy, Volume 46, Issue 3, 1991, Pages 319-378, ISSN 0584-8547, 10.1016/0584-8547(91)80035-2

[13] Sugar, J.; Corliss, C.:
Energy levels of chromium, Cr I through Cr XXIV, Journal of Physical and Chemical Reference Data, NIST, 1977, 6, 317-384

[14] Theisen, M.; Lackner, F.; Krois, G.; Ernst, W.:
Ionization Thresholds of Alkali Metal Atoms on Helium Droplets, The Journal of Physical Chemistry Letters (2011) 21, S. 2778 - 2782

[15] Toennies, J. P.; Vilesov, A. F.:
Superfluid helium droplets: a uniquely cold nanomatrix for molecules and molecular complexes, Angewandte Chemie-International Edition, Wiley-V C H Verlag Gmbh, 2004, 43, 2622-2648

6.2 Theses

[16] Auboeck, G:
Spectroscopy of Alkali-Metal Atoms and their High-Spin Oligomers on Helium Nanodroplets in External Magnetic Fields. TU Graz, Doctoral Thesis

[17] Goesweiner, C.:
Konstruktion und Charakterisierung eines Laser-Strahlprofilmessgeraetes. TU Graz, Bachelor Thesis, will be published 2012

[18] Hauser, A.:
Ab initio Berechnungen an Kaliumtrimeren. TU Graz, Master Thesis, 2005

[19] Kautsch, A.:
Title will be defined. TU Graz, Doctoral Thesis, will be published 2013 or 2014

[20] Koch, M.:
Magnetic Resonance Spectroscopy of Single Alkali-Metal Atoms Isolated in Superfluid Helium Nanodroplets. TU Graz, Doctoral Thesis, 2010

[21] Krois, G.:
Heavy Alkali and Alkaline Earth Metals on Cold Helium Droplets: First Comparison of Excitation Spectra. Graz University of Technology, Master Thesis, 2011

[22] Lackner, F.:
Laserspektroskopie und Flugzeitmassenspektrometrie an Rubidium-dotierten Heliumnanotroepfchen. Graz, TU, Master Thesis, 2009

[23] Lanzersdorfer, J.:
Assembly and Test of a Helium Cluster Beam Apparatus for Magnetic Field Studies of Atom and Molecule Doped Helium Nanodroplets. TU Graz, Master Thesis, 2008

[24] Nagl, J.:
Spectroscopic investigations of homo- and heteronuclear molecules of K and Rb on the surface of argon and helium clusters. TU Graz, Doctoral Thesis

[25] Pifrader, A.:
Pulsed laser spectroscopic investigations of rubidium atoms attached to helium nanodroplets, TU Graz, Master Thesis, 2008.

[26] Poms, J.:
Optical detection of ESR on doped helium droplets: the influence of optical pumping in experiment and theory. TU Graz, Master Thesis, will be published 2012

[27] Pototschnig, J.V.:
Title will be defined. TU Graz, Master Thesis, will be published 2012

[28] Ratschek, M.:
Doping Helium Droplets: Development of a High-Temperature Pickup Source. Graz, TU Graz, Master Thesis, 2010

[29] Theisen, M.:
Aggregation of Rb and Cs atoms on helium nanodroplets and laser ionization of cold clusters. TU Graz, Doctoral Thesis

[30] Volk, A.:
Electron Spin Resonance of Single 87Rb Atoms Attached to Superfluid Helium Nanodroplets. TU Graz, Master Thesis, 2011

6.3 Books

[31] Arbeitsunterlagen zur Vorlesung Experimentalphysik 3,
Institut fuer Experimentalphysik, TU Graz, Auflage WS 2007/08

[32] Demtroeder, W.:
Experimentalphysik 3, Springer, 2009

[33] Haken, H., Wolf, H. C.:
Atom- und Quantenphysik, Springer, 2003

[34] Hertel, I.V., Schulz, C.-P.:
Atome, Molekuele und optische Physik 1, Springer, 2010

[35] Letokhov, V.S.:
Laser Control of Atoms and Molecules, Oxford University Press, 2007

[36] Schwabl, F.:
Quantenmechanik fuer Fortgeschrittene, Springer, 2008

[37] Lide, D.R.:
CRC Handbook of Chemistry and Physics. CRC Press, Boca Raton, FL, 77th edition, 1996.

6.4 Manuals

[38] Operating Manual
QMG 422
BG 800 453 BE
Balzers Instruments, FL-9496 Balzers, Liechtenstein

[39] Operating Instructions
SpectraPro © 275
Acton Research Corporation, Acton, MA 01720, USA

[40] Meilhaus Electronic Manual
ME-4600 Series

Revision 2.3E
Meilhaus Electronic GmbH, D-82178 Puchheim, Germany

[41] Brackmann, U:
Lambdachrome © Laser Dyes.
3rd Edition
Lambda Physik AG, D-37079 Goettingen, Germany

[42] R372 Photomultiplier Tube Technical Data Sheet
July 83
Hamamatsu Photonics K.K., Iwata-City, Shizuoka Pref., 438-0825, Japan

6.5 Online-Sources

[43] National Institute of Standards and Technology (NIST). NIST Atomic Spectra Database. May 2011 - June 2012. ⟨http://www.nist.gov/pml/data/asd.cfm⟩

[44] Thorlabs.com. UV Fused Silica High-Precision Windows. July 2012.
⟨http://www.thorlabs.com/newgrouppage9.cfm?objectgroup_id=3983⟩

7 Appendix

The following pages include a description of LabView VIs that had been useful for controlling and accessing several devices named in chapter 3 by means of a Meilhaus ME-4660 ADC card. These are modifications of templates from Meilhaus Electronic GmbH. [40] is giving further information. This appendix also includes CAD drawings of the components of the laser beam aperture presented in subsection 3.4.5. Also scripts for importing data from a Logitech C300 into MATLAB are outlined. They are useful for creating plots of the pulse energy cross-section of a laser beam, as described in section 3.9.

LabView

The CLII PC is equipped with a Meilhaus ME-4660 ADC card. This device has a 500 kHz clock. The cards in- and output devices are accessible by a coax connector board at the electronic device rack of the lab. This board is shown in fig. 7.1. It is indicated, to which devices the coax connectors belong.

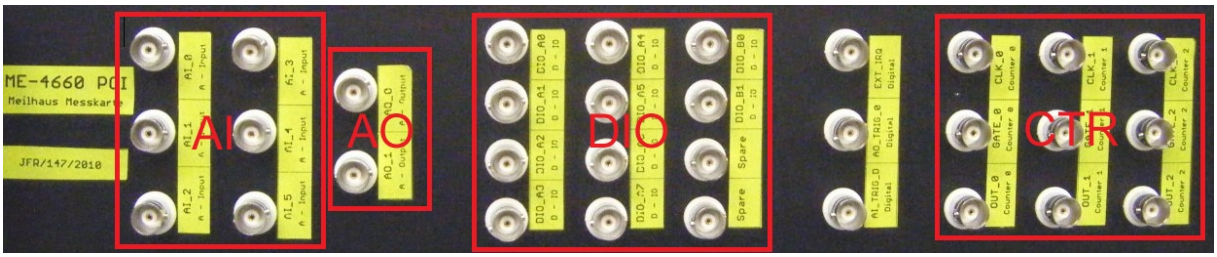

Figure 7.1: Meilhaus ADC Card Connector Board

The control of the devices using NI LabView is described in the following. The aim was to develop LabView virtual instruments (VIs) to handle in- and outputs using templates from Meilhaus Electronic GmbH.

Digital In- and Output

A LabView VI called `singleDIO.vi´ was developed to access the digital in- and output (DIO) channels of the Meilhaus ADC card. There are eight single-bit channels of a first and 2 channels of a second DIO device accessible at the board. These are TTL devices having a high-low level difference of 4.6 V and a maximum output current of 10 mA.

A VI that allows reading from and writing to each DIO bit independently was developed. Therefore, Boolean variables had been defined in the VI. Since there are two DIO devices accessible, two rows of boolean LEDs were created in the VIs front panel shown in Fig. 7.2.

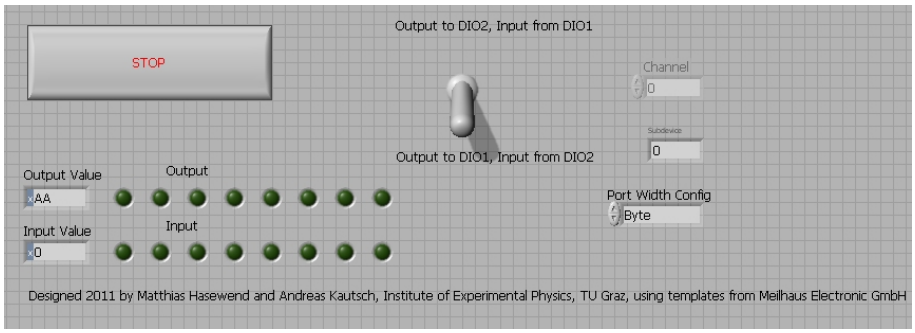

Figure 7.2: Front Panel of singleDIO.vi

Only the output LEDs can be clicked. By clicking onto, they light up or vanish and change their state. States are 0 or 1. The corresponding output voltage rises from low to high or falls.

The eight channels are interpreted as a one byte variable. The byte value can thus be set to values from 0 to 256, or 0 to FF in hexadecimal code. In LabView, the variable is represented as a read-only numerical control and corresponding variable named `Output Value´

The two DIO devices can be operated simultaneously. There is a switch to select if either device 1 is output and device 2 is input or vice versa.

The whole program is included in a loop to enable continuous operation. There is a `Stop´-Button to exit the loop and thus terminate the program. Fig. 7.3 shows the corresponding block diagram.

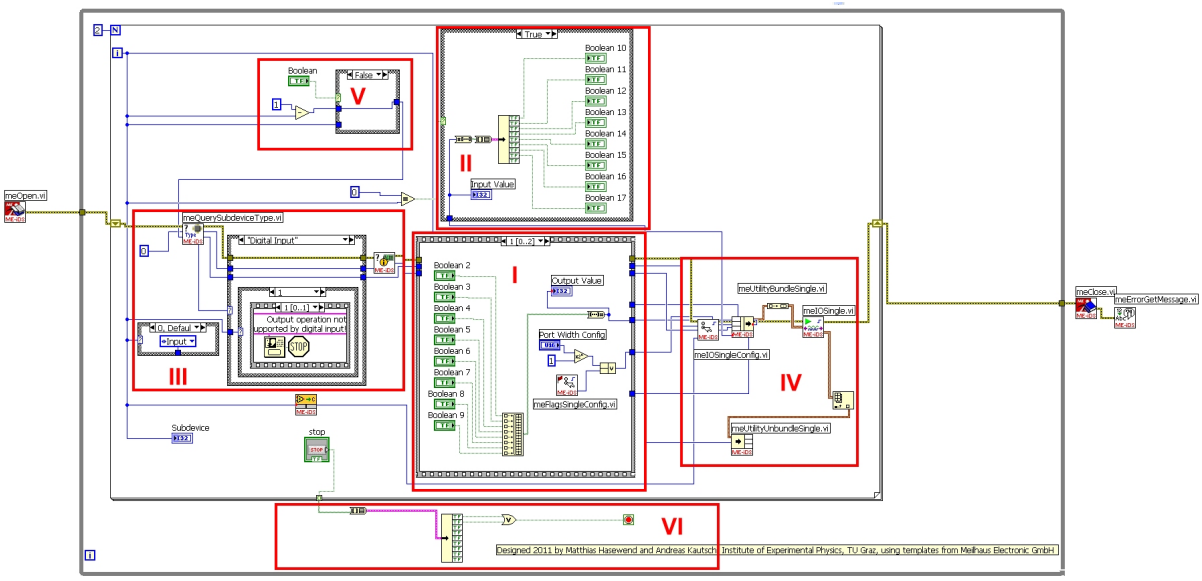

Figure 7.3: Block Diagram of singleDIO.vi

Section I in fig. 7.3 is handling the input channel. Eight output LEDs are gathered to a cluster, converted into an eight-bit integer called `Output Value´ and submitted to devices `meIOSingleConfig.vi´ `me UltilityBundleSingle.vi´ and `meIOSingle.vi´ within section IV. `meUltilityBundleSingle.vi´ bundles the data and delivers it to `meIOSingle.vi´, which accesses the ME-4660 hardware.

Section II handles the input channel. Section IV returns data from the DIO hardware. The result is another eight-bit integer displayed by `Input Value´. It comes from the return-cluster of `meIOSingle.vi´ and is unbundled by `meUltilityUnbundleSingle.vi´.After reconversion to boolean, each bits state is indicated by a LED. Below it is explained why this section is included in a case structure.

All the figures sections are included in a for-loop counting from 0 to 1. During one loop cycle, section III is executed at first. It initializes a DIO device. Subsequently, depending on the actual loop counter value, section I or II is executed performing in- or output. Afterwards section IV terminates the device. Sections III and IV had been included in a template from Meilhaus Electronic GmbH. Sections I, II, V and VI in the figure and the surrounding loops are self-developed.

The VI continues performing output and input. The reason for switching from input to output is that one cannot access more than one device at the same time using these Meilhaus templates.

The switching is realized by connecting the for-loop counter value to a port of `meUltility BundleSingle.vi´ named `Direction´. This Sub-VI is included in section IV. 0 means

input, 1 stands for output. At the same time, one has to submit to a port of `meQuery SubdeviceType.vi´ called `Subdevice´. If both `Direction´ and `Subdevice´ are 0 at the same time, it means input from device 1, both being 1 means output to device 2.

It is useful to enable switching to input from device 2 and output to device 1. It is enabled by assuring `Subdevice´ to be 1, or 0, while `Direction´ is 0 or 1. The switch in the front panel fig. 7.3 is responsible for that. In the block diagram, this switch is represented by another boolean variable in section V.

To make 0 become 1 and 1 become 0, the counter value is subtracted from 1. In case of 1, the case structure transmits the counter value. Otherwise it transmits the subtracted value.

Finally, a temporal series of in- and output tasks is created. Therefore the 0-1-for-loop is surrounded by a while loop. There is a stop button included in the front panel fig. 7.3 to break that loop and terminate the program.

Analog Input

Unlike digital devices, analog output and input devices are separated. Six different analog input channels are connected with the board on the rack shown in fig. 7.1. The input voltage working range limits are $\pm$ 10 V, inputs are protected up to $\pm$ 15 V. Every channel has a high resistance input stage of typically 600 MΩ and an input capacity of 3 pF.

Within the working range of voltage, it is possible to define cut off limits called minimum and maximum physical value. The trigger may be `software´ or `external´.

A VI called `singleAI.vi´ was developed to perform analog input tasks. Fig. 7.4 shows its front panel. It includes controls to specify minimum and maximum physical value. Since the device can also be used for triggering, there are controls to specify `Trigger Type´, `Trigger Edge´ and `Time Out´. The VI displays the analog input value in a form named `Physical Value´ and a waveform chart. By pressing `Stop´, the program terminates.

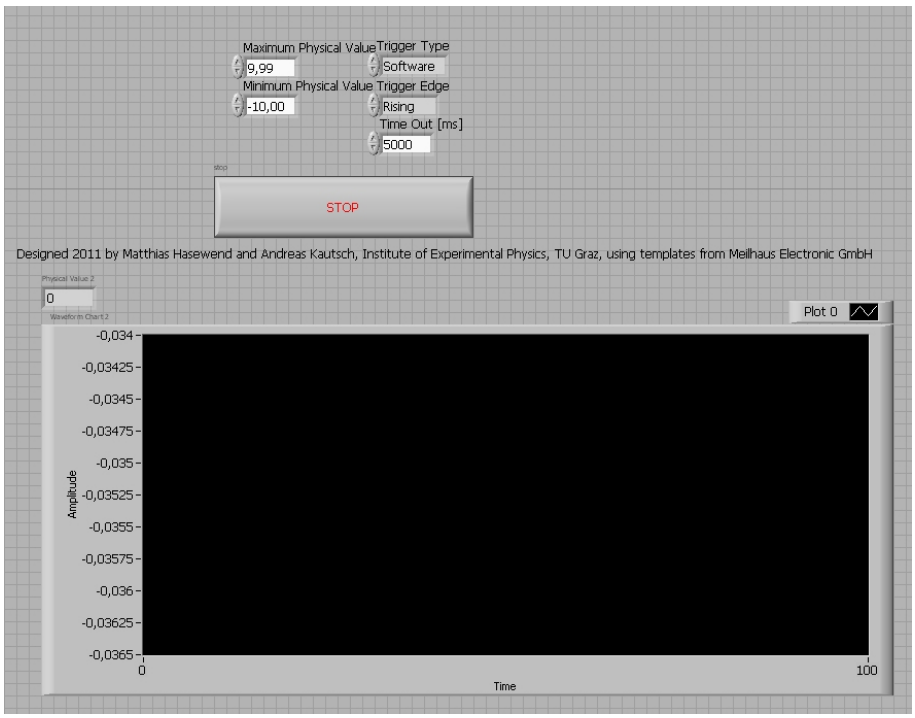

Figure 7.4: Front Panel of singleAI.vi

Fig. 7.5 shows the corresponding block diagram. Unlike with DIO, only small modifications of the original Meilhaus template had been necessary. There are blocks for opening and initialisation of the device, for reading the input value and for closing the communication. The read-out blocks had been surrounded by a while-loop.

In the loop, `meIOSingle.vi´ accesses the device and returns a cluster. That clusters units are representing the different input channels. The channel is selected by variable No. I in fig. 7.5. Each channel is represented as a cluster on its own. These sub-clusters are unbundled by `meUltilityUnbundleSingle.vi´ and converted by `meUltilityDigitalTo Physical.vi´. Outcomes are different values related to the actual channel. Variable No. II specifies which value should be handed over. The first value in the cluster is the input. Once more it gets converted and subsequently plotted in a waveform chart.

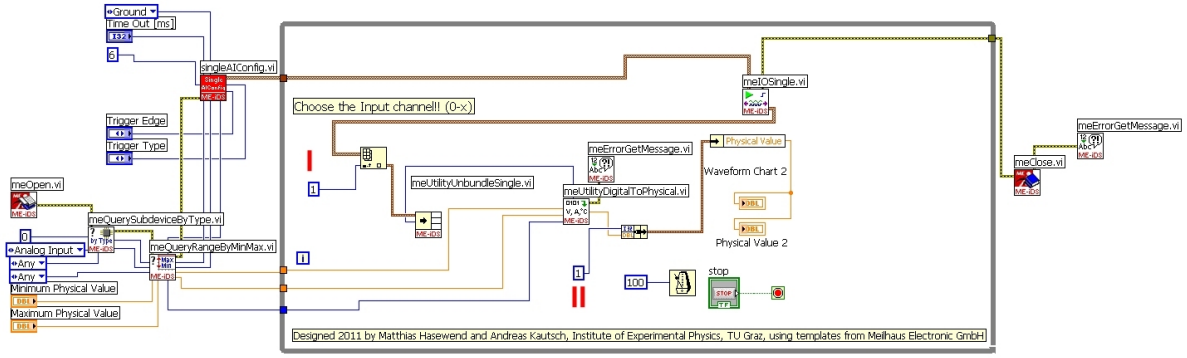

Figure 7.5: Block Diagram of singleAI.vi

In this VI, the treatment of the output of `meUltilityDigitalToPhysical.vi´ and the surrounding while-loop having a delay of 100 ms per loop cycle are the only self-developed parts.

Analog Output

The Analog Output VI called `singleAO.vi´ is pretty similar to analog input. One can also specify `Trigger Type´, `Trigger Edge´ and `Time Out´, as fig. 7.6 shows. The most important variable is the output value. In this demonstration VI, it is a sine function in time. A respective block was inserted in the block diagram, as shown below. In the front panel, the sine is plotted in a waveform chart. Output voltage ranges from -10 to +10 V, the output current should not exceed ± 5 mA. The user can select the channel via some extra control. `Stop´ terminates the program.

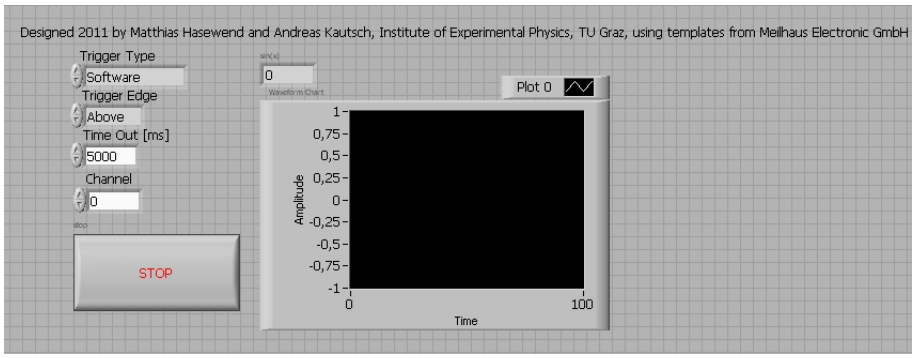

Figure 7.6: Front Panel of singleAO.vi

Fig. 7.7 shows the corresponding block diagram. It is almost identical to the original template. Yet the output components had been surrounded by a while-loop. A sine function and a 10 ms delay per loop cycle had been inserted. The sine value is converted by `meUltilityPhysicalToDigital.vi´. The converted value is bundled with some other

specific values by `meUltilityBundleSingle.vi´ and passed on to `meIOSingle.vi´, which accesses the device.

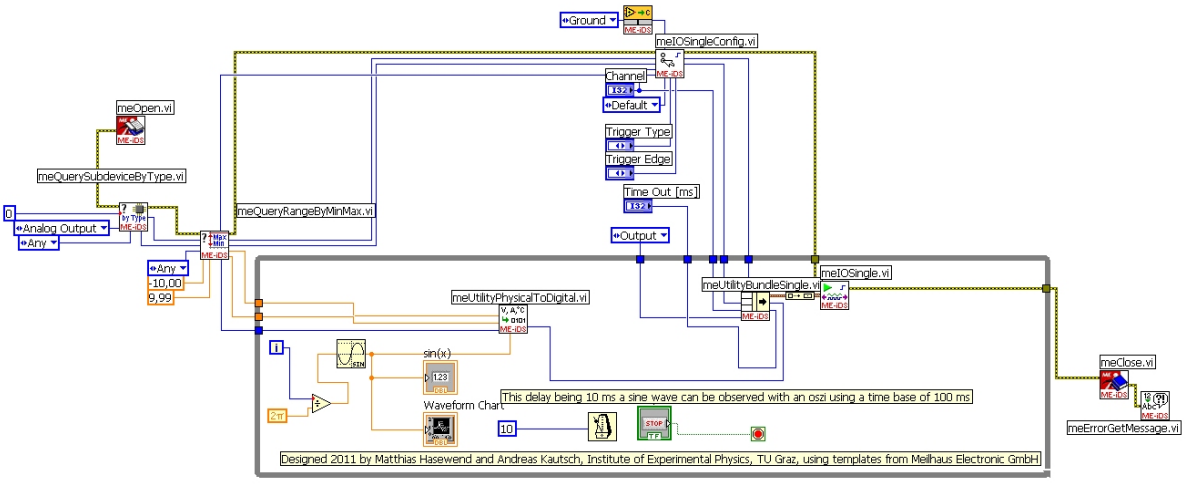

Figure 7.7: Block Diagram of singleAO.vi

The sine function can easily be substituted by an arbitrary output function, as desired. The user could also be enabled to specify the output value in a form of the block diagram.

Counter

The Counter VI is called `singleCTR.vi´. Its front panel is shown in fig. 7.8. There are three counter devices accessible at the connector board shown in fig. 7.1. Each of them is a 82C54 standard counter chip. The counter signal is connected to the GATE. The form named `Device´ allows selecting one of the three counting devices. A `Starting Value´ can also be set. The actual counter reading is displayed by the form `Counter Value´.

`8254 Mode´ is the only entry of `Configuration´. The counter clock `Reference´ can be `Internal´ or `External´. In case of `External´, a clock signal needs to be connected with the CLK input. The `Loop delay´ is described below.

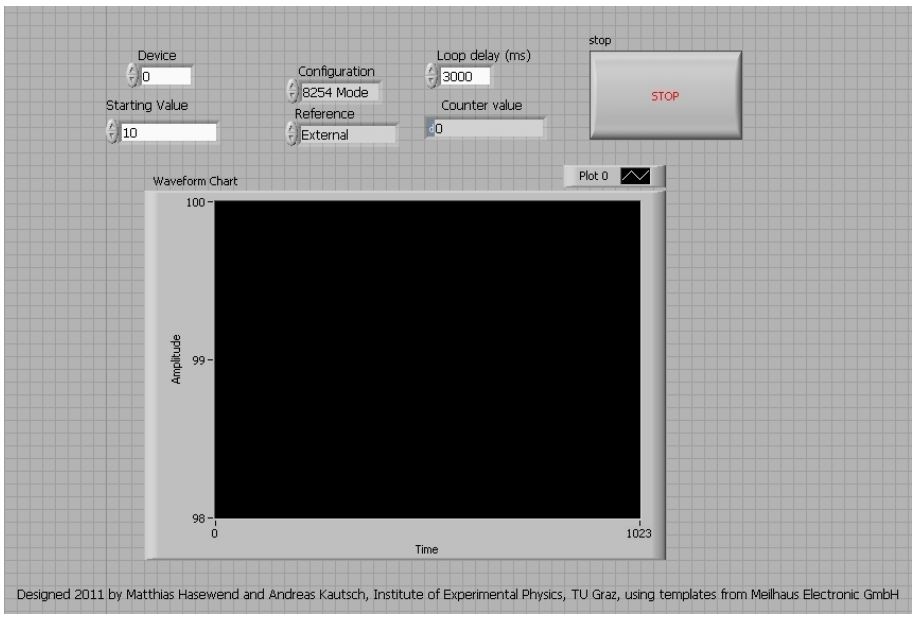

Figure 7.8: Front Panel of singleCTR.vi

Fig. 7.9 shows the corresponding block diagram. As before, only minor modifications of the original template had been necessary. A while-loop including a user-defined delay had been created. During every loop cycle, the counter reading is obtained from `meIOSingle.vi´ and `meUltilityUnBundleSingle.vi´. The reading is displayed in the front panel and plotted in the waveform chart.

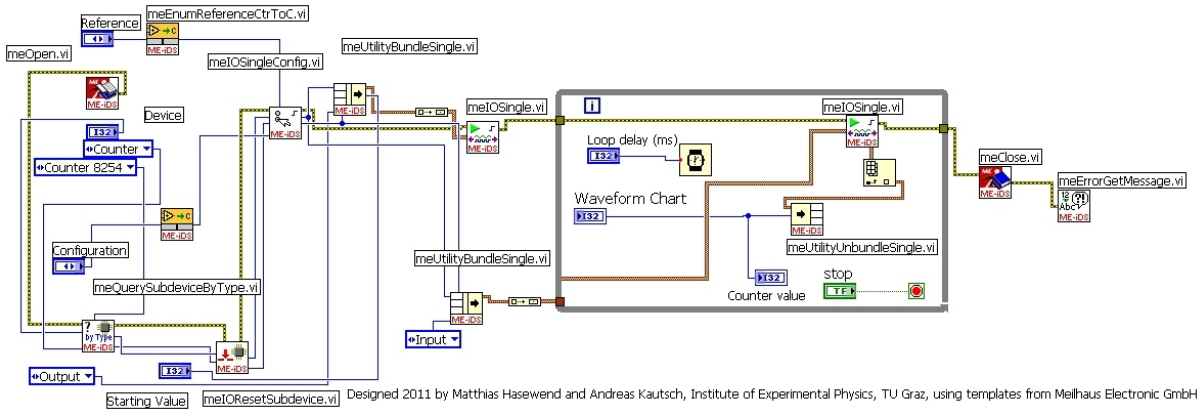

Figure 7.9: Block Diagram of singleCTR.vi

The Meilhaus ADC card manual [40] includes further information about these devices. During the experiments described in chapter 4, the developed VIs had been rather useful. They were included in more complex VIs for recording PI spectra and laser spectral profiles. Therefore the Analog Input device was used to record the output signals of a laser powerhead and the picoamperemeter combined with an analog processor described

in section 3.7.

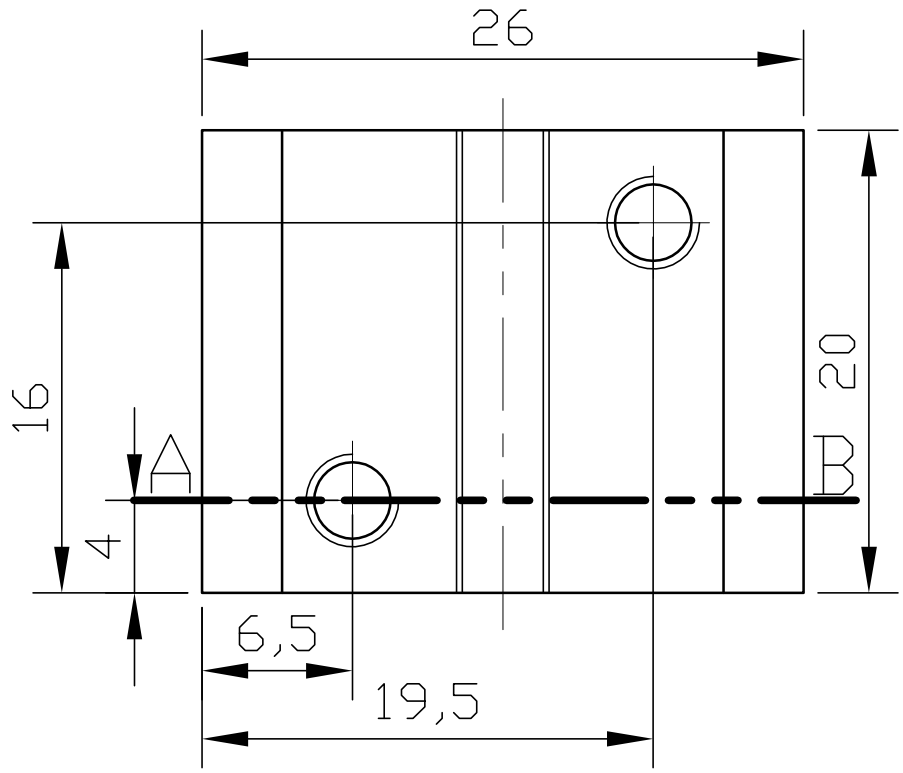

Schnitt A-B

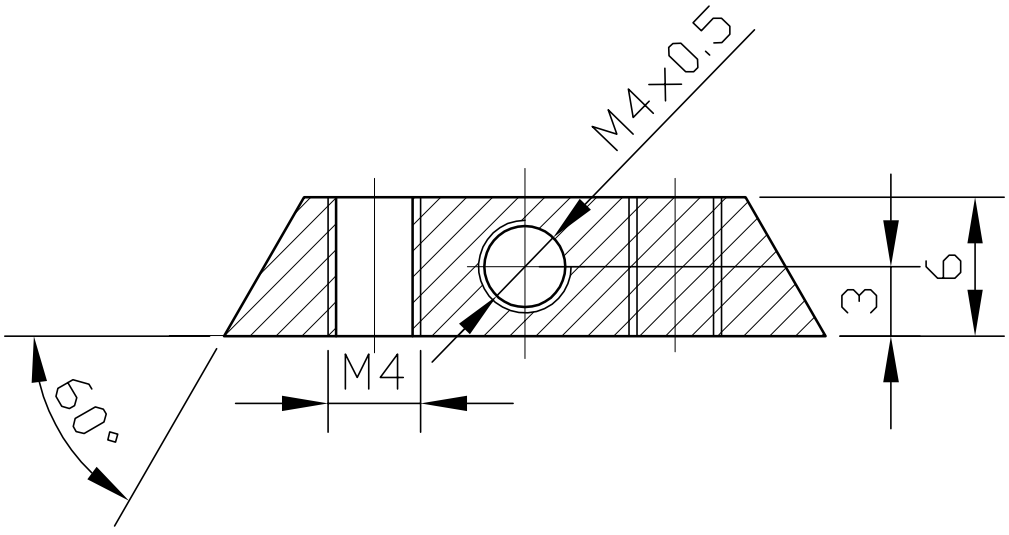

	Tag	Name		
Gez.	28.09.2011	Hasewend	Gleitschuh, 6 Stück, Messing	TU-Graz
Gepr.	-	-		
Norm gepr.	-	-		
Maßstab 3:1	Strahlblende			1
Freimaß-tol.				Ersatz für:
				Ersetzt durch:

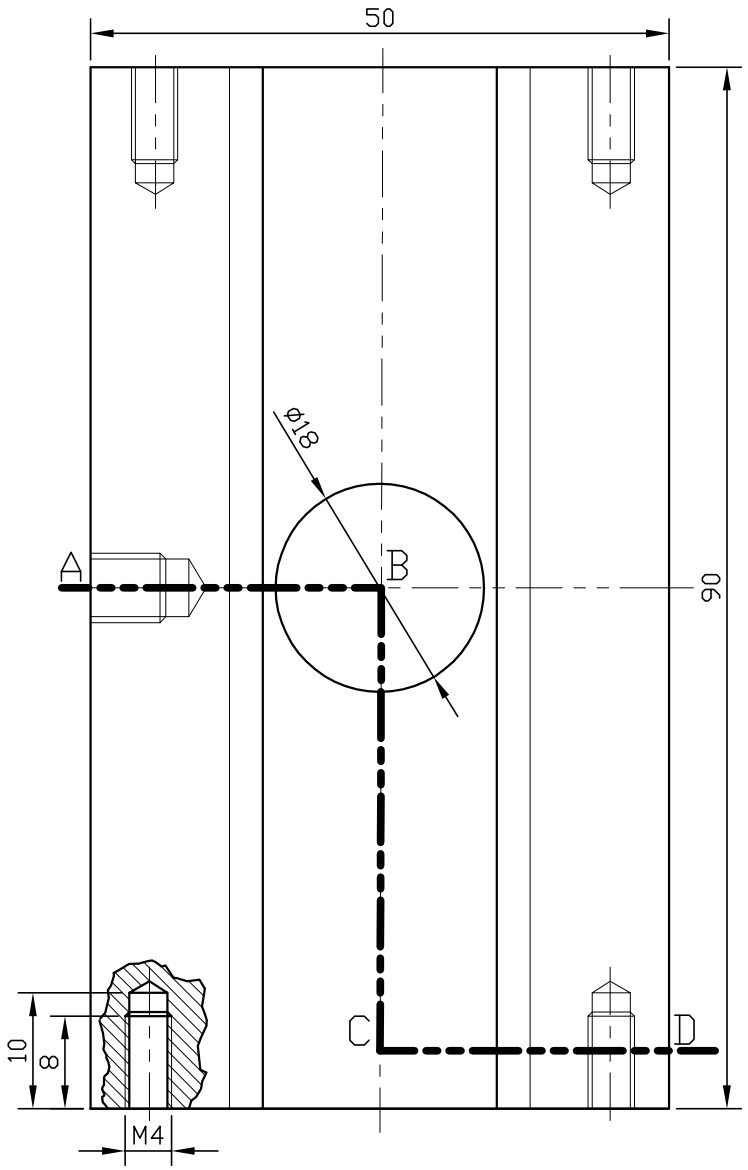

Schnitt A-B-C-D

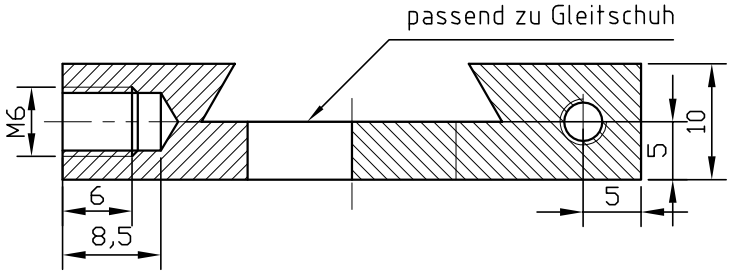

	Tag	Name		
Gez.	28.09.2011	Hasewend	Führung, 3 Stück, Aluminium	TU-Graz
Gepr.	-	-		
Norm gepr.	-	-		
Maßstab 3:2			Strahlblende	2
Freimaß-tol.				Ersatz für:
				Ersetzt durch:

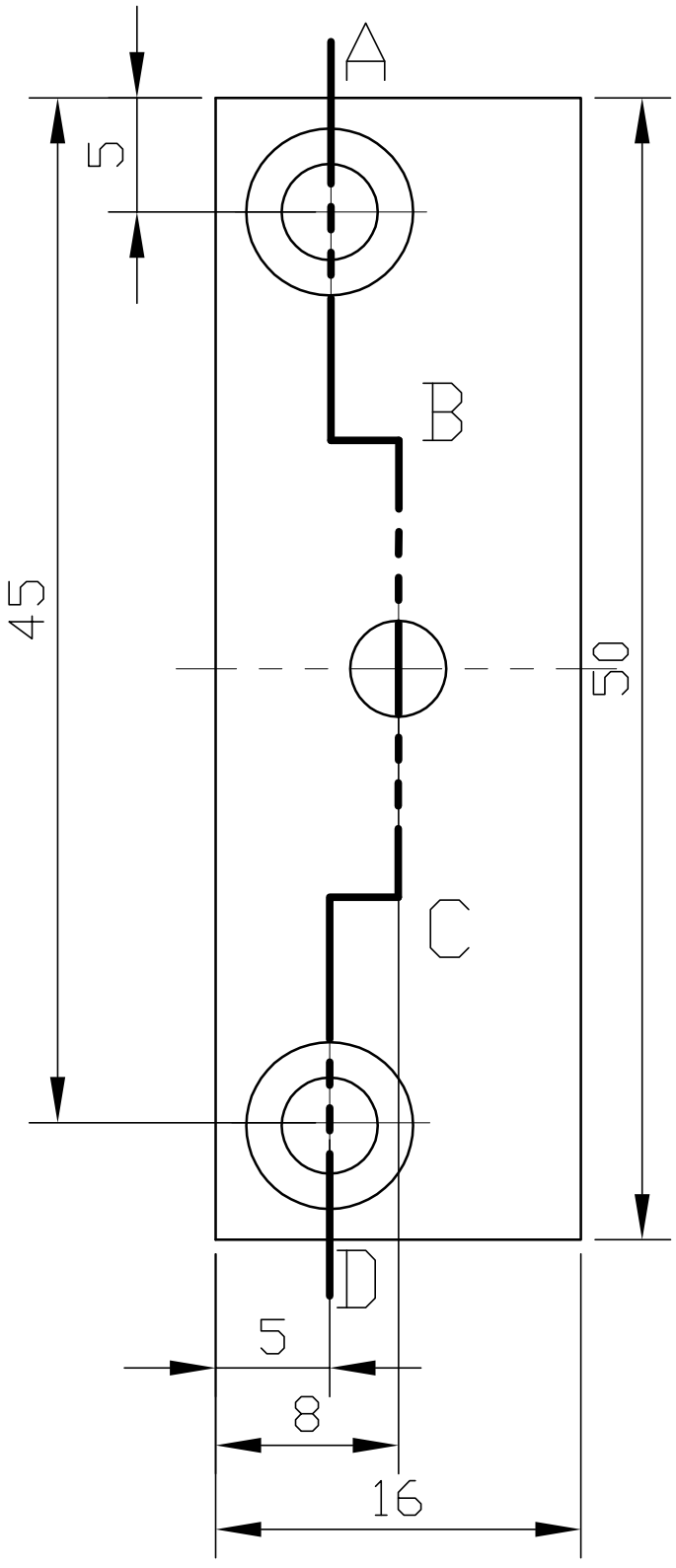

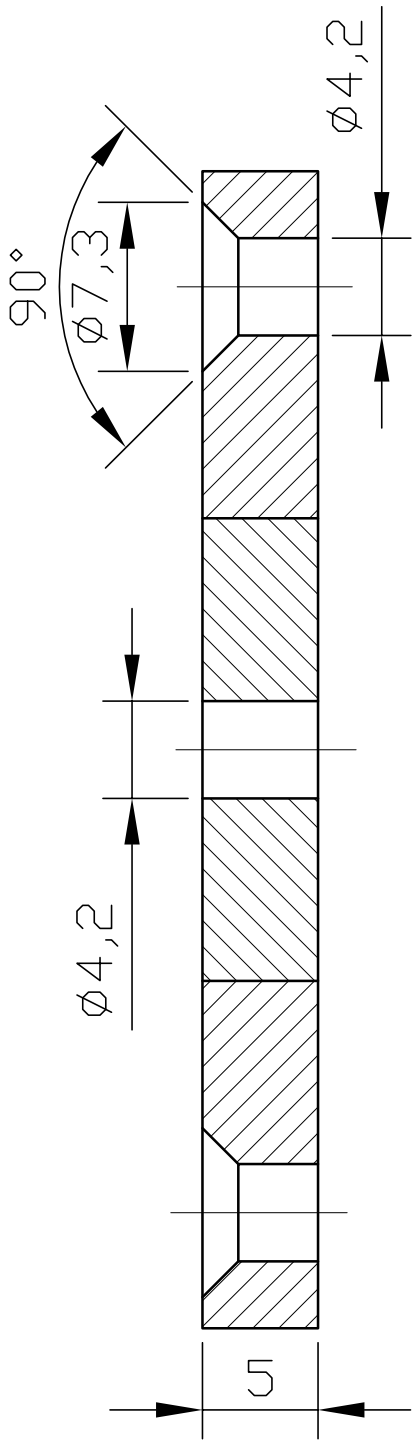

Schnitt
A–B–C–D

	Tag	Name		
Gez.	28.09.2011	Hasewend	Block, 6 Stück, Aluminium	TU-Graz
Gepr.	-	-		
Norm gepr.	-	-		
Maßstab 3:1	Strahlblende			3
Freimaß-tol.				Ersatz für:
				Ersetzt durch:

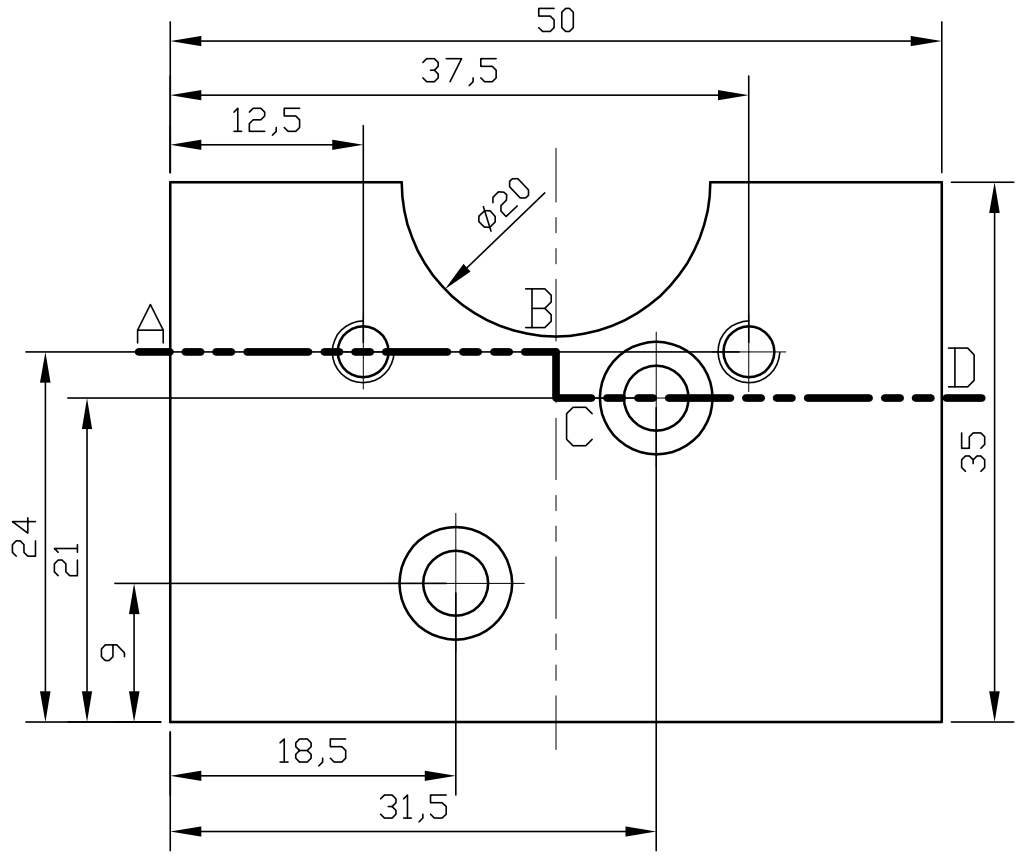

Schnitt A-B-C-D

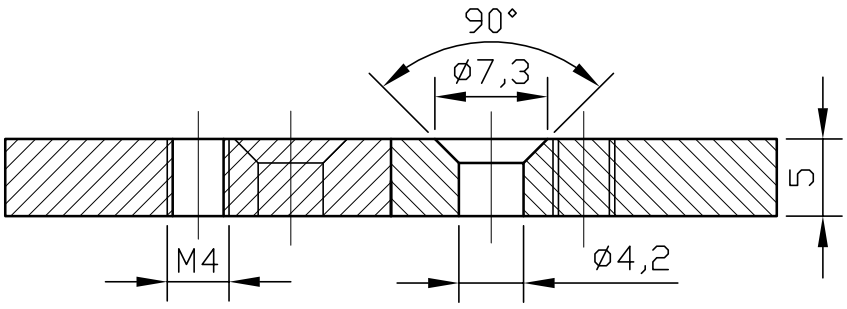

	Tag	Name		
Gez.	28.09.2011	Hasewend	Halteplättchen, 6 Stück, Aluminium	TU-Graz
Gepr.	-	-		
Norm gepr.	-	-		
Maßstab 2:1	Strahlblende			4
Freimaß-tol.				Ersatz für:
				Ersetzt durch:

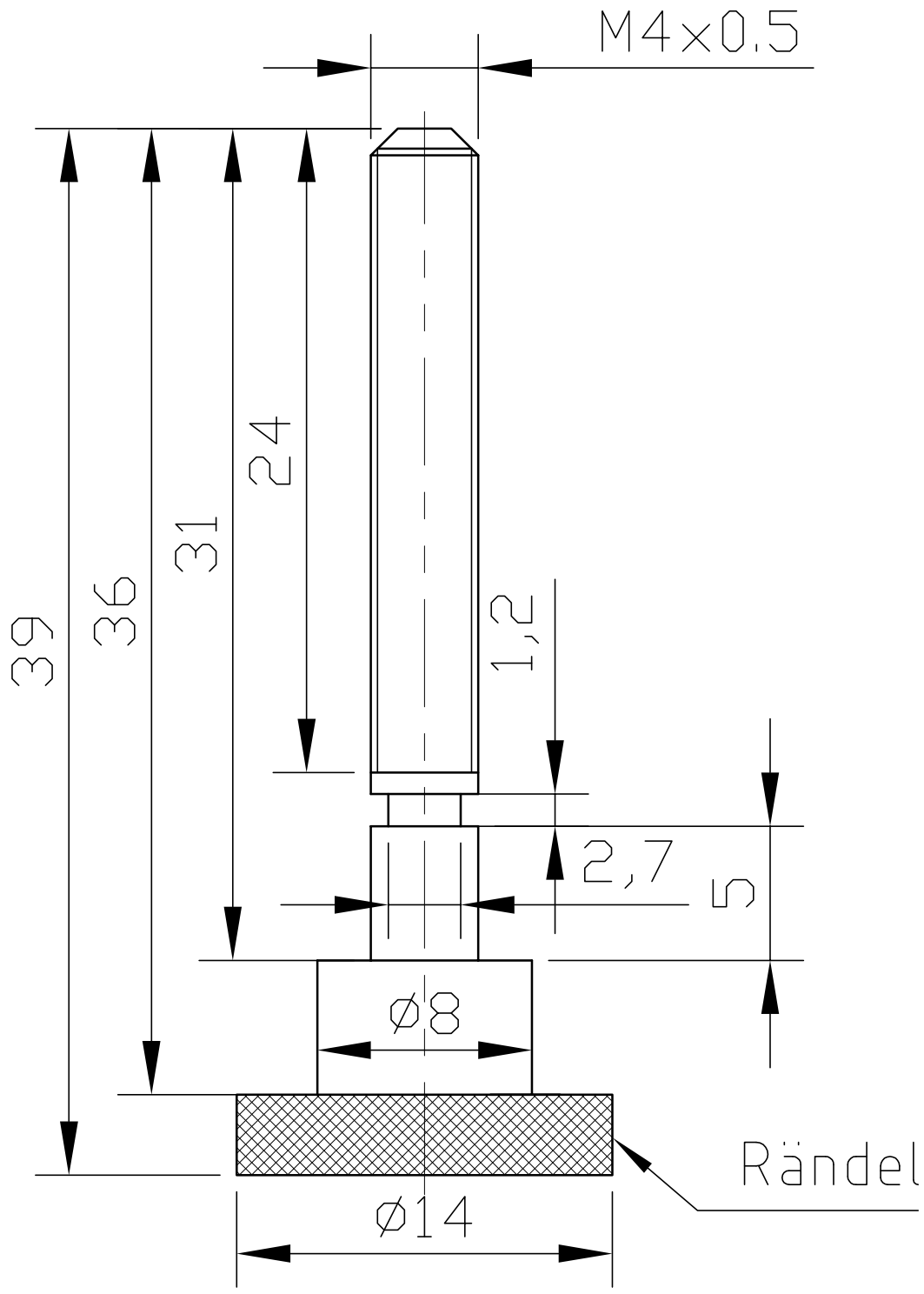

	Tag	Name		
Gez.	28.09.2011	Hasewend	Feinschraube, 6 Stück, Messing	TU-Graz
Gepr.	-	-		
Norm gepr.	-	-		
Maßstab 4:1	Strahlblende		5	
Freimaß-tol.			Ersatz für:	
			Ersetzt durch:	

```
%Hasewend Matthias
%Institute of Experimental Physics
%TU Graz
%2011/12
%
%+++++++++++++++++++++++++++++++++++++++++++++++++++++++++++++++++++++++
%This MATLAB vers.7 program is used to
%
%+ obtain data from an USB Logitech C300 webcam recording the intensity
%profile of an attenuated laser beam.
%
%+ FFT-smooth the laser profil.
%
%+ scale the x- and y-markers of the FFT-smoothed profile so that its size
%fits to CCD chip it was recorded with.
%
%+ scale the intensity so that it represents the laser intensity in terms
%of pulse energy density by means of the total pulse energy.
%+++++++++++++++++++++++++++++++++++++++++++++++++++++++++++++++++++++++

%input
vid = videoinput('winvideo', 1);
data = getsnapshot(vid);

%display image
image(data);

%select the colour channel that fits the best to the laser
%1 = red, 2 = green, 3 = blue
channel = 1;
data = double(data(:,:,1));

%reduce the image size to 1/n
n = 4;
siz = size(data);
ii1 = 1:4:siz(1);
ii2 = 1:4:siz(2);
data = data(ii1,ii2);

%plot the raw profile
figure();
surf(data,'EdatageColor','none','LineStyle','none','FaceLighting','phong');
xlabel('x / px');
ylabel('y / px');
title('Raw laser intensity profile');

%2D-FastFourierTransform of the image
data_fft = fft2(data);

%cut-off parameter: depends on the noise of the profile and the size
%and thus has to be determined manually. For the cam's default image size
%and typical noise, the default par is 150000.
par = 150000;

%cut-off and re-transfrom
data_fft(abs(data_fft) <= 150000) = 0;
```

```
data = real(ifft2(data_fft));

%cut off nonpositive FFT artifacts
data(data <= 0) = 0;

%plot the smoothed profile
figure();
surf(data,'EdatageColor','none','LineStyle','none','FaceLighting','phong');
xlabel('x / px');
ylabel('y / px');
title('Smoothed laser intensity profile');

%height and width of the CCD
hei = 2.7;
wid = 3.6;

%sum normalization
data = data./sum(data(:));

%total pulse energy in mJ
en = 1;

%scale values in order to make the integral of the pulse energy density
%across the CCD area become the total pulse energy
data = data/((hei/siz(2))*(wid/siz(1)))*en;

%create x and y grid
xx = repmat(1:siz(2),siz(1),1);
yy = repmat((1:siz(1))',1,siz(2));

%scale grid to the size of the CCD
xx = xx./siz(2)*hei;
yy = yy./siz(1)*wid;

%plot the profile
figure();
surf(xx,yy,data,'EdgeColor','none','LineStyle','none','FaceLighting','phong');
grid off;
title('Laser beam profile / mJ/mm²');
colorbar;
view([0,90]);
xlabel('x / mm');
ylabel('y / mm');
```